Thesis for the degree of Doctor of Engineering

Micromechanics of oxides

From complex scales to single crystals

ANAND H.S. IYER

Department of Physics

Chalmers University of Technology

Göteborg, Sweden 2019

Micromechanics of oxides
From complex scales to single crystals

Anand H.S. Iyer
ISBN 978-91-7905-230-0

Doktorsavhandlingar vid Chalmers tekniska högskola
Ny serie nr 4697
ISSN 0346-718X

Department of Physics
Chalmers University of Technology
SE-412 96 Göteborg
Sweden
Telephone + 46 (0)31-772 1000

Cover illustration

From complex oxides to single crystals: Top left image shows a microcantilever prepared from Cr_2O_3 scales that has fractured. A closer look at the crack is shown in the bottom left figure. Further examination of fracture mechanism is done by imaging the fracture surface, shown in figure on bottom right. A study on active cleavage planes for Cr_2O_3 was performed using single crystals, and the method of identifying the planes has been shown with an example (top right).

Printed by Chalmers Reproservice
Göteborg, Sweden 2019

Micromechanics of oxides - From complex scales to single crystals
Anand H.S. Iyer
Department of Physics
Chalmers University of Technology

Abstract

Protective oxide scales shield high temperature materials from corrosion, thus ensuring safety and long material life under adverse operating conditions. Cracking and spallation of such scales can lead to fatigue crack initiation and expose the material to further oxidation. It is therefore imperative to measure the fracture properties of oxides so that they can be incorporated in the life estimation models of high temperature materials. Existing models require inputs on oxide properties such as fracture strain and elastic modulus. The established measurement methods are mainly applied for thick (several microns) scales, but for many materials such as superalloys the oxides are thinner ($<$ 1 µm), and the results would be affected by the influence of substrate and residual stresses. Focused ion beam machining (FIB) enables the preparation of micro sized specimens in the size range of these scales.

In this work, a modified microcantilever geometry with partially removed substrate is proposed for testing of oxide scales. Room temperature microcantilever bending of thermally grown superalloy oxide (complex oxide with an upper layer of spinel and lower layer of Cr_2O_3) revealed the presence of plasticity, which is attributed to the deformation of the upper cubic spinel layer and low defect density of the volume being probed. Due to difficulties in isolating Cr_2O_3 from the complex oxide layer, dedicated oxidation exposures are performed on pure chromium to generate Cr_2O_3 which is tested using the same cantilever geometry at room temperature and 600 °C. Results show lower fracture strain at 600 °C in comparison to room temperature and presence of cleavage type of transgranular fracture in both cases, pointing to a need for studying cleavage fracture of Cr_2O_3. This was analysed using microcantilever bending of single crystal Cr_2O_3 to identify the preferential cleavage planes. Finally, fracture toughness was also measured through microcantilever bending and micropillar splitting.

Thus, it is shown that micromechanical testing is an effective tool for measuring fracture properties of oxide scales. The fracture study of Cr_2O_3 scales show that it is a complex process in which the crystallographic texture also plays a role. Surface energy and fracture toughness criterion was unable to explain the fracture behaviour of single crystal Cr_2O_3 observed from experiments. Such a comprehensive analysis can contribute towards the development of reliable models for oxidation assisted failure.

Keywords: oxide scales, fracture, micromechanical testing, Cr_2O_3, electron microscopy

"Nothing worth having comes easy"

-Theodore Roosevelt

Preface

The research work presented in this thesis was carried out at the Division of Materials Microstructure in the Department of Physics, Chalmers University of Technology, during the time period June 2015 - October 2019, under the supervision of Dr. Magnus Hörnqvist Colliander and Prof. Krystyna Stiller.

This work has received funding from High Temperature Corrosion (HTC) centre, Swedish Energy Authority (Grant No: P22581-3), and Swedish Research Council (Grant No: 2015-04719).

List of appended papers

I. *Room temperature plasticity in thermally grown sub-micron oxide scales revealed by micro-cantilever bending*
Anand H.S. Iyer, Krystyna Stiller, Magnus Hörnqvist Colliander
Scripta Materialia 144 (2018) pp 9-12.

II. *Microscale fracture of chromia scales*
Anand H.S. Iyer, Gaurav Mohanty, Krystyna Stiller, Johann Michler, Magnus Hörnqvist Colliander
Materialia 8 (2019) 100465.

III. *Fracture of chromia single crystals on the microscale*
Anand H.S. Iyer, Krystyna Stiller, Magnus Hörnqvist Colliander
In manuscript.

IV. *On the cleavage fracture toughness of Cr_2O_3 single crystals*
Anand H.S. Iyer, Krystyna Stiller, Magnus Hörnqvist Colliander
In manuscript.

My contributions to the appended papers

I. I performed the sample preparation, experiments, results analysis, and was lead author of the paper.

II. I performed the sample preparation, room temperature experiments, results analysis, and was lead author of the paper.

III. I performed the sample preparation, experiments, analysis of experimental results, and was lead author of the paper.

IV. I performed the sample preparation, experiments, analysis of experimental results, and was lead author of the paper.

Publications not included in this thesis

I. *Crack Growth Studies in a Welded Ni-base Superalloy*
Anand H.S: Iyer, Krystyna Stiller, Magnus Hörnqvist Colliander
Solid State Phenomena 258 (2016) pp 237-240.

II. *Influence of dwell time on fatigue crack propagation in Alloy 718 laser welds*
Anand H.S. Iyer, Krystyna Stiller, Gunnar Leijon, Henrik C.M. Andersson-Östling, Magnus Hörnqvist Colliander
Materials Science and Engineering A 704 (2017) pp 440-447.

III. *Prediction of mechanical response for 5000-Series aluminum alloy coupling visco-plastic self- consistent approach with finite element method*
A Ruggiero, M Hörnqvist Colliander, A H S Iyer, N Bonora, D Gentile, G Iannitti and G Testa
Journal of Physics: Conference series 1063 (2018) 012104.

IV. *Effects of gas flow on detailed microstructure inhomogeneities in LPCVD TiAlN nanolamella coatings*
Ren Qiu, Axel Forslund, Olof Bäcke, Anand H.S. Iyer, Mohammad Sattari, Wiebke Janssen, Thorsten Manns, Johannes Kümmel, Andrei Ruban, Dirk Stiens, Hans-Olof Andrén, Mats Halvarsson
Accepted for publication in Materialia (2019).

Acknowledgements

Looking back four years at myself, I see a naïve guy who moved to a foreign land, with a mind full of uninformed optimism on starting a research journey. Over time, I have grown both as a person and a researcher with a new outlook on life. The journey was far from easy. There were twists and turns, ups and downs, light and darkness, but I had the opportunity to learn from each experience. Now it has brought me to this point, where I complete one chapter of my research life. It definitely would not have been possible without the support I received from the people around me, like a leaf that carries the ant along an unruly river.

I would like to begin by expressing my gratitude to my supervisor, Dr. Magnus Hörnqvist Colliander who has been instrumental in the progress that I have achieved. He has been a mentor who guides me in personal growth, a friend who lends an ear to my personal problems, and a teacher from whom I have learned a lot. Most importantly, he is someone I can always count on for support. I admire the way you work and I hope that someday I will be able to achieve that level of focus and discipline. I would like to thank my co-supervisor Prof. Krystyna Stiller for always supporting me and encouraging me to do good work. Thank you to both of you for providing me the opportunity to perform this excellent work, and for trusting me with the project.

My collaborators at the High Temperature Corrosion centre helped in so many ways for performing various experiments, for which I am very grateful. Special thanks to Dr. Gaurav Mohanty for helping me with the high temperature experiments, for sharing his knowledge and for always responding to questions I had. Kleindiek GmbH and Alemnis AG have provided excellent service and have responded promptly to doubts regarding the instruments and have been timely in fixing issues with them for which I am very thankful. I am grateful to CMAL for their constant support in keeping the instruments running and to Ola Löfgren for always having a solution for my computer problems. I am extremely thankful to my colleagues from my division, Eva Olsson's group and CMAL for creating such positive work environment and for all the discussions we had. I have had several teachers over the last years, colleagues and professors who enlightened me with their knowledge that helped me in my research. I am thankful to every one of them.

I will be forever grateful to my parents without whom I would not have achieved anything. Thank you for aiding me in my journey to find myself. I am very thankful to my in-laws, for always treating me like their own son and checking up on my welfare constantly despite the physical distance between us. Finally, I am indebted to my wife, who I call molu, for being there with me in every moment of this journey, constantly supporting and encouraging me, showering me with love and providing confidence even at times I lost faith in myself. You have made me a better human being and no words will suffice to express what you mean to me.

Contents

CHAPTER 1

Introduction

1.1 High temperature materials

The ability of hot gas to move objects has been known for almost 2000 years and people throughout history have attempted to put this force to use in various forms. In 1791, John Barber applied for a patent for a design of a horseless carriage, which is considered as the first, albeit primitive form of gas turbine design [1]. George Brayton later developed the concept of Brayton cycle, meant to be used for piston engines. This thermodynamic formulation led to the realisation that higher efficiency could be obtained through raising the temperature of operation and was implemented in power generation and later in aviation. There rose a need for materials that could work at higher temperatures without compromising on strength. The early 1900s saw the development of austenitic stainless steels. Intense research regarding modification of properties of such steels by changing chemical compositions and adding new elements was occurring due to its requirement in the jet engine technology. This led to the development of a class of alloys that could be used in jet engines and power generation turbines and came to be know as superalloys. Such materials do not lose their mechanical strength even at high homologous temperatures ($> 0.6\ T_m$). They also possess superior oxidation and corrosion resistance [2]. This is achieved through the addition of elements

such as chromium and aluminium, which form a dense and thin layer of oxide scale on top of the material, which protects the material from further oxidation. Oxides formed from such elements have very high melting points (> 2000 °C), have low oxide growth kinetics, and have low density of defects.

1.2 High temperature fatigue and oxidation

High temperature components typically experience rapid changes in mechanical loads and temperatures. For example, jet engines use gas turbines, which experience periods of sustained mechanical loading and large variation in temperatures and loads during the course of a flight. Similarly, gas turbines operated in combustion based power generation plants are subjected to an increasing number of thermal cycles as the power is ramped up or down based on the power generated from the use of an increasing fraction of renewable sources like wind and solar power, which are intermittent sources. This leads to a form of fatigue in the material commonly termed as thermomechanical fatigue (TMF). The nature of fatigue experienced by these materials have a time component to it, unlike other structural components, thus making fatigue analysis a lot more complex in comparison to other materials [3]. The loading is also experienced by the protective oxide scales on the top of the materials. Oxides are generally brittle and therefore damage can occur in the scale in the form of through cracks or spallation [4] and this exposes the underlying material for further corrosion in the form of rapid oxidation. Since the loading and temperature variation is repetitive, spallation and oxidation can take place a number of times, thus depleting the material of the protective oxide forming element and reducing its corrosion resistance. Through cracks in oxides are also a site of stress concentration, which is detrimental to the underlying material. Thus, there is a clear interplay between mechanical loading and oxidation.

Thermomechanical fatigue is a life limiting factor for high temperature materials (e.g. superalloys) [5], which necessitates the understanding of fatigue mechanism at high temperature. Several studies have been performed on the high temperature fatigue of different superalloys [6–8] and it has been seen that periods of sustained load at high temperatures causes a significant increase in crack growth rate [9] (Figure 1.1). This is termed as dwell fatigue. Such a reduction in material life is noticed in the presence of environment and oxygen has been shown to play a role [10, 11].

Several mechanisms have been proposed for the effect of environment and oxygen seems to play a main role in affecting the life. Among the different mechanisms, two are most often discussed; dynamic embrittlement (DE) [11] and stress assisted grain boundary oxidation (SAGBO) [12]. According to DE, the oxygen diffuses to the grain boundaries and causes their decohesion. SAGBO

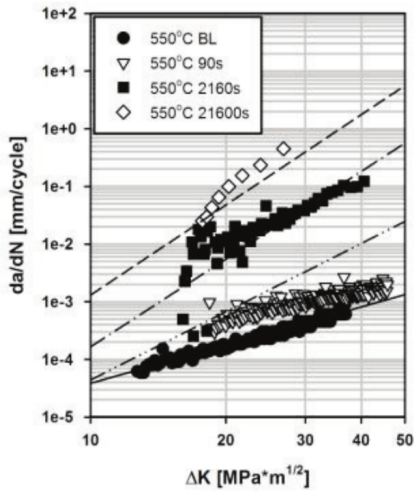

Figure 1.1: Crack growth rate of Alloy 718 at 550 °C with different dwell times [9].

states that the accelerated crack propagation occurs due to the fracture of brittle oxides formed ahead of the crack tip in grain boundaries. Although the relative importance of these two mechanisms are debated, the use of advanced microscopy techniques show the formation of oxides ahead of the crack tip [13, 14] . Figure 1.2 shows one such case where the closed intergranular oxide at the crack tip shows a layered oxide.

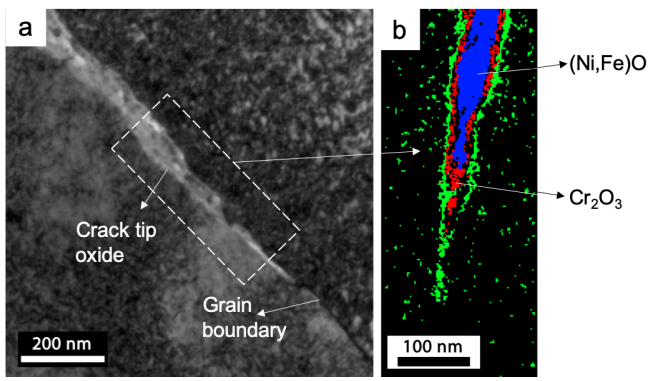

Figure 1.2: (a) TEM bright field image of closed intergranular oxide at crack tip; (b) STEM EDS map of crack tip oxide showing different layers. Blue is Ni and Fe oxide, red is Cr_2O_3, and green region depleted of chromium showing nickel enrichment [14].

Chan *et al.* [15] developed a model for oxidation assisted crack growth where

the threshold stress intensity factor for high temperature fatigue is given by,

$$K_{\mathrm{th}} = E_{\mathrm{ox}}\varepsilon_{\mathrm{cr}}\sqrt{\frac{t_{\mathrm{ox}}}{3\left(1-\nu^2\right)}} + 2\mathrm{sgn}(\varepsilon_{\mathrm{tr}})\left[\frac{E_{\mathrm{ox}}\sigma_{\mathrm{y}}\left|\varepsilon_{\mathrm{tr}}\right| t_{\mathrm{ox}}}{2\left(1-\nu^2\right)}\right]^{1/2} \tag{1.1}$$

E_{ox} and ε_{cr} are the elastic modulus and fracture strain of the crack tip oxide, t_{ox} is the thickness of the oxide, and ν is the Poisson's ratio. ε_{tr} refers to the transformation strain, which accounts for the volume change and its sign depends on the type of oxide formed. These values are required as input to obtain a reliable life assessment based on oxidation models.

Cruchley *et al.* [16] observed in the case of pre-oxidised RR1000 nickel based superalloy that early crack initiation occurred at the surface (Figure 1.3(a)) and internal grain boundary oxides (Figure 1.3(b)) in comparison to as-machined samples, which caused a reduction in fatigue life. Room temperature fatigue testing of the same material under different pre-oxidised conditions revealed that the fatigue life dropped significantly in comparison to the as-received material, and the increase in pre-oxidation time led to further reduction of life (Figure 1.3(c))[17].

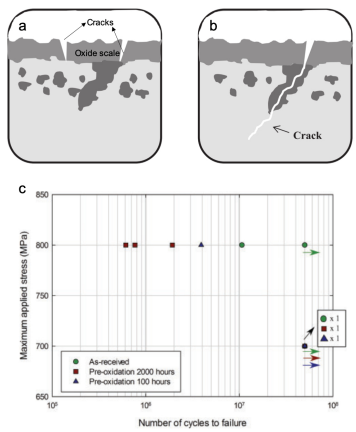

Figure 1.3: (a) Surface oxide cracks as stress concentrations; (b) Cracking of external and intergranular oxide [16]; and (c) Fatigue life of as received and pre-oxidised specimens [17].

Another critical case is for out of phase thermomechanical fatigue (OP-TMF), where the highest tensile strain can coincide with the minimum temperature during the fatigue cycles. Bauer *et al.* [18] studied thermomechanical fatigue in γ-TiAl, and they found that the material life for OP-TMF can be a factor of 30 lower than that for isothermal conditions, when tests are performed in air (Figure 1.4). The effect on life is much less when OP tests are conducted in vacuum. The explanation is that the oxide which forms during the compression

cycle cracks easily during the tensile cycle where temperature is minimum. This clearly implies that oxidation effects are much more important for OP-TMF than tensile mean stress, which is the commonly proposed explanation.

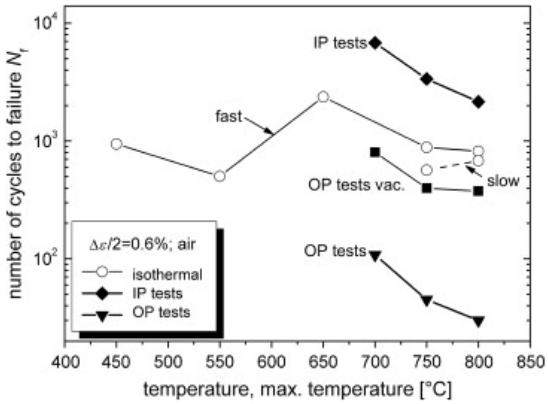

Figure 1.4: Fatigue life of γ-TiAl under different conditions [18].

1.3 Fracture of oxides

The adherence of oxide scales and modes of fracture has been a subject of extensive research over several decades due to their importance in corrosion protection of high temperature materials. Models based on fracture mechanics have been developed in order to explain the failure of oxide scales [19, 20]. However, experimental data regarding fracture strain and elastic modulus are required as inputs to the model, which has been pointed out as one of the critical issues [21]. Conventional methods such as resonance frequency, acoustic emission, four point bending, nanoindentation, etc [22, 23] are typically used for measuring mechanical properties of oxides such as fracture strain and elastic modulus. However, they are applicable to oxide scales which are few tens of microns thick. For thinner oxide scales which are a few microns or less thick, the substrate [23] and residual stresses [24] significantly affect the measured values. This clearly points to the need for development of advanced testing methods, which can measure mechanical properties of protective oxide scales in systems where they are typically thin. Micromechanical testing has shown promise in the measurement of mechanical properties at the micro scale. Focused ion beam (FIB) milling enables the preparation of micro-sized specimens of size in the range of thickness of the oxide layers and they can be tested with the help of micromanipulators or in situ nanoindenters through methods such as microcantilever bending, micropillar compression, micro-tensile testing, etc. Such methods have been successfully employed in the measurement of systems such as coatings [25, 26], oxides [27–29], grain boundaries [30, 31], etc.

1.4 Aim of the study

The aim of this study is to understand the deformation and fracture of oxide scales formed on high temperature materials. The following questions have been addressed in this thesis:

- Can micromechanical testing methods be developed to measure fracture properties of thin oxide scales without influence from substrate and residual stresses?
- In the case of Cr_2O_3, which is the principal protective oxide layer for high temperature materials working below 1000 °C, is it possible to identify the mechanisms of fracture and measure the microscale fracture properties?

It has to be noted that although this work takes Ni-base superalloys as an example, the observations are equally applicable to any high temperature material which relies on the formation of a protective oxide scale for corrosion protection such as stainless steels, intermetallics, titanium alloys, etc. Superalloys were chosen since they represent a class of materials that operate in the harshest conditions and failure prevention is more critical as they are used in components such as jet engines, where unexpected failure leads to huge loss of life. The reasoning behind choosing Cr_2O_3 is that it is much less studied in comparison to Al_2O_3, even though Cr_2O_3 is widely used as a protective oxide scale, in particular for stainless steels.

CHAPTER 2

Literature survey

Fracture of materials is a field that has been studied extensively throughout history. Fracture can be either brittle or ductile. Many metals undergo ductile fracture, which involves significant plastic deformation before failure. Brittle fracture is the mode of failure for materials such as glasses and ceramics. Since the materials in this work are oxides which typically fail in a brittle fashion, this chapter focuses on the theory and state of the art in brittle fracture. Additionally, the measurement techniques for oxide scales and novel methods will also be discussed in this chapter.

2.1 Brittle fracture

The design of structures is always aimed at good performance and to avoid failure. This is not an entirely new concept as evident from the majestic pyramids in Egypt or the Roman bridges and cathedrals which are still standing and functioning as they should. This was possibly achieved through trial and error method since there was no proper understanding on why materials fail and how much is their strength. The earliest attempt at quantification of strength of materials was possibly performed by Leonardo Da Vinci where he related the strength of iron wires to their length by the use of a primitive

setup [32, 33]. It was seen that wires of shorter length supported more weight in comparison to longer ones. The likely explanation is the difference in defect density with the volume of tested material. A quantitative approach to studying fracture was, however, achieved only in the 20^{th} century.

The strength of a material is dependent on the energy required to break the atomic bonds that hold the material together. Fracture results if an energy higher than the cohesive strength of the bonds is supplied. This is the theoretical strength of the material, which is given by the formula,

$$\sigma_{th} = \sqrt{\frac{E\gamma_s}{x_0}} \tag{2.1}$$

E is the elastic modulus of the material, γ_s is the surface energy per unit area, and x_0 is the equilibrium distance between atoms in the material. By inserting typical values for E and γ_s, the theoretical strength of a material is usually approximated to be around $E/10$, but in reality materials typically fail at a much lower stress. This is primarily due to the fact that flaws exist in the material, which leads to its failure. A quantitative approach to estimate the fracture stress was attempted by Griffith [34] in 1920 who proposed a theory relating fracture stress and flaws present in the material based on Inglis's work on stress concentrations around an elliptical crack [35]. Griffith proposed that the propagation of a crack depends on the net energy and it will be in equilibrium if,

$$\frac{dU}{dA} + \frac{dW}{dA} = 0 \tag{2.2}$$

Where U is the internal strain energy and W is the work done for creating new surfaces, and dA is the increment in crack area. For a plate with an elliptical crack of length $2a$ (major axis $\gg$ minor axis), Griffith derived the fracture stress to be,

$$\sigma_c = \sqrt{\frac{2E\gamma_s}{\pi a}} \tag{2.3}$$

when plane stress conditions are considered.

This treatment by Griffith is only applicable to ideal brittle materials such as glass and does not agree with the properties of metals. Irwin, and later Orowan modified equation 2.3 to add a term for plastic work.

Another approach was suggested by Irwin, which is based on *energy release rate* [32].

$$G = -\frac{dU}{dA} \tag{2.4}$$

For a material with a pre-existing flaw of half length a,

$$G = \frac{\pi\sigma^2 a}{E'} \tag{2.5}$$

For plane stress conditions,

$$E' = E \tag{2.6}$$

and for plane strain conditions,

$$E' = \frac{E}{1-\nu^2} \tag{2.7}$$

The critical energy release rate is given by,

$$G_c = \frac{\pi(\sigma_c)^2 a}{E'} = 2\gamma_s \tag{2.8}$$

U is the potential energy, A is the crack area, and σ_c is the applied stress at fracture. One thing to be noted here is that even though it says energy release rate, it is not a time derivative, but based on crack area. G is considered as the crack driving force. It is directly related to *stress intensity factor* (K), which is a proportionality constant used in describing the stress state near crack tip of the material, and it depends on geometry of the specimen, crack size and load. In general, stress intensity factor is represented as,

$$K = f\sigma\sqrt{\pi a} \tag{2.9}$$

f is a function of crack and specimen geometry. G and K are related by the following equation,

$$G = \frac{{K_I}^2}{E'} \tag{2.10}$$

ν is the Poisson's ratio. The critical energy release rate, above which crack propagation occurs, is given by,

$$G_c = \frac{{K_c}^2}{E'} \tag{2.11}$$

K_c is the critical stress intensity factor. Under plane strain conditions, K_c is called *fracture toughness (K_{Ic})*. It is a material property and does not depend on the geometry, and is widely used as a measure for strength of a material.

2.1.1 Microstructural effects

The above description is only valid for homogeneous and elastic isotropic materials. One thing to be aware of is that this kind of analysis does not consider the effect of environment and other external factors that cause crack growth. For example, work of fracture in air can be lower than that in vacuum [36]. Also, crack growth and strength of the material is governed by events happening at atomistic levels, which are not considered in a continuum analysis, and is described later.

The interaction of the crack with certain features can increase the work of fracture and provide damage resistance to materials. In crystalline materials, the cracks tend to follow certain directions as it is more energetically favourable, termed as cleavage. The cleavage through a certain grain can stop at the grain boundary as the neighbouring grain has a different orientation, hence a different direction for the preferred cleavage. Another situation is the presence of inclusions. When the crack tip encounters the inclusion, the crack tip gets blunted and higher stresses are required to further propagate the crack. The presence of secondary phases (in alloys) or fibrous reinforcement (in composites) is another case where the fracture is resisted by the strength of these materials that the cracks encounters, and also their orientation. They can also cause crack deflection which increases the crack area and hence the work of fracture. A situation in which the work of fracture can decrease is at interfaces. Consider an example of a polycrystalline material, the work done for transgranular fracture (through the grain) is,

$$W_{ad} = 2\gamma_s \tag{2.12}$$

But for intergranular fracture (grain boundary fracture), it is,

$$W_{ad} = 2\gamma_s - \gamma_{gb} \tag{2.13}$$

Where γ_s is the surface energy for the lattice, and γ_{gb} is the grain boundary energy. However, transgranular fracture can occur in some situations even though it requires more energy, as in the case of polycrystalline Al_2O_3, where it has been observed that the fraction of transgranular fracture increases with increase in grain size [37, 38].

Cleavage is generally explained in terms of the crystal structure, especially for ionic solids, which have a clearly defined structure. There are several theories as to why cleavage occurs in certain planes. Some concepts refer to the number of bonds and distance between atoms on a certain plane, which favours fracture. Another concept is more commonly accepted which is the surface energy criterion. This states that the cleavage occurs in the crystallographic plane with the minimum surface energy. In practice, this is not followed for many materials such as spinels [39]. Schultz suggests the use of fracture toughness as the criterion for cleavage since it occurs in a rapid and catastrophic fashion and fracture toughness is the crack resistance parameter. There is, however, limited studies dedicated to relate fracture toughness to cleavage of materials.

2.1.2 Atomistic aspects

The origin of forces in materials that holds atoms together is different depending on whether the material is metallic, ionic or covalent [40]. At the surface

of a solid, the ions do not take the same positions as they do in the bulk, they are displaced in order to minimise the surface energy. This affects the properties of the material as well. This rearrangement might lead to attractive or repulsive forces between the newly created surfaces, which increase or decrease the work of fracture, though this also depends on the contribution of the environment. Griffith's criterion is based on continuum approach, but failure of materials occur at the atomic level by breaking of bonds, and therefore the criterion is not applicable when considering fracture at atomic level. The crack is stable for a range of stress above Griffith's stress, and this is attributed to a phenomenon called lattice trapping effect [41].

Brittle fracture, when considered at atomic level, can occur in a continuous or discontinuous manner. Continuous type of bond breaking is not affected by structural relaxations and proceeds continuously, as expected from continuum theory. The discontinuous propagation is related to atomic relaxations and rearrangement of atoms around the crack tip [42]. The load is also shared between bonds at the crack tip and its neighbour. This increases the energy barrier required for fracture, and thereby the critical stress. These are the effects of lattice/ bond trapping. This implies that the atomic structure and crystallographic orientation also play an important role in fracture. Experimentally, crack propagation is shown to be anisotropic in many materials [43]. It was seen through atomistic simulations in silicon that in some directions, the crack growth was in a continuous manner and the loads were smaller in comparison to other directions where lattice trapping effects increased the critical load [42].

If Griffith's criteria is followed, the generated surface should be so that the resulting surface energy is minimum (Equation 2.8). But this is not the case always. In some cases such as NiAl, lattice trapping results in the formation of crack surface which consists of half occupied Al atoms, instead of forming asymmetric Al and Ni surfaces [43]. This is because the energy barrier to reach the former surface condition is smaller than the one required to overcome the lattice trapping effect. This can occur in the case of interfaces as well. Atomistic simulations of oxide grain boundaries and dihedral angle measurements reveal that $\gamma_{gb} \sim \gamma_s$ for oxide ceramics, which implies that the work of fracture is halved for intergranular fracture in comparison to transgranular fracture (see Equation 2.13). Despite this, higher fraction of transgranular cracks is seen in brittle materials such as ceramics at high crack propagation speeds. A possible explanation is the bond trapping effects which increase the energy for the crack to propagate through interfaces. This can be overcome by thermal activation, seen in ceramics in the form of increased fraction of intergranular fracture at higher temperatures. This is true for cleavage fracture as well, where the supplied thermal energy is used to overcome the difficulty in creating certain surfaces. This is the case for Al_2O_3, where basal ($\{0001\}$) fracture can occur at very high temperatures, but not at room temperatures [43]. In the case

of polycrystalline Al_2O_3, the fraction of intergranular fracture has been seen to increase with temperature [37], which cites another example where thermal activation supplies the energy for the crack to propagate through the grain boundaries. Though it is not easy to isolate and quantify the lattice trapping effects, it is useful in explaining the differences in theoretical and experimental values for fracture.

In short, it can be said that brittle fracture is a complex process which is influenced by several macroscopic and atomistic factors and needs a thorough understanding and analysis to produce reasonable explanations for strength of materials.

2.2 Oxide scale properties and their measurement

As mentioned in section 1.3, the fracture of oxides is a critical factor determining the life of high temperature materials. The oxide layers experience not only external stresses due to mechanical loading, but also internal stresses. One source of stress is due to the volume difference between oxide and metal, which is expressed in terms of Pilling-Bedworth ratio (R_{PB}). It is the ratio between the molar volumes of the oxide and metal. An $R_{PB} < 1$ creates tensile stresses in oxide leading to the formation of through cracks. If it is > 1, compressive stresses result, and a ratio > 2 can cause buckling and spallation. A ratio between 1 and 2 ensures a passivating and protective oxide lawyer, which is preferable. Another source of stress is due to the difference in thermal expansion of oxide and metal. Typically, the metal has a higher coefficient resulting in residual compressive stresses in the oxide scale. Depending on the net stress and temperature distribution, the oxide scales can undergo fracture or deformation, even in the absence of external loading.

As a result of external stresses, oxide scales can fail in multiple manners. The application of a tensile stress leads to scale cracking and a compressive stress leads to spallation [44]. Another possibility is deformation of the oxide scale. The stress required to activate plastic deformation is higher than that for initiation of cracks, below a certain temperature [45]. At high temperatures, plasticity in oxides can occur by creep, which has been observed for polycrystalline Al_2O_3 by diffusional creep [46] and in single crystal Al_2O_3 by dislocation creep [47]. There is another possibility where the conditions are such that the oxidation rate is higher than the crack rate, leading to healing of the cracked oxides. This phenomenon is referred to as pseudoplasticity [45]. This was observed in the case of heat resistant steels at 800 °C under tensile strains by Schütze [48]. It was seen that below a critical strain rate, the oxide scale heals itself, thus preventing further oxidation. This effect was more pronounced for adherent scales than detached ones.

The properties of an oxide scale determine the life of the alloy protected by it. Therefore, it is necessary to evaluate the mechanical properties of these scales in order to obtain a reliable model for fatigue life of engineering alloys. The principles of fracture mechanics can be applied to determine the failure conditions of oxide scales. Several studies have attempted to fit fracture mechanics principles for failure of oxide scales [4, 49, 50]. Comprehensive oxide failure models have also been developed for several systems which demonstrates various mechanisms of failure based on the elastic strain and oxide layer thickness [19, 20]. Rudolphi *et al.* [51, 52] proposed a simplified model based on the physical defect size rather than scale thickness.

A critical property for an oxide scale is the elastic modulus. There are some indirect methods for the evaluation of elastic modulus such as the vibration method [53]. This method is based on the fact that the resonance frequency of the specimen changes when oxidised. The difference in resonance frequency is utilised in the evaluation of the elastic modulus of the oxide scale. Nicholls *et al.* [53] used this method to determine the elastic modulus of oxide growing on mild steel at 550 °C as 185 GPa. A direct method of determination of the elastic modulus is by using nanoindentation, which also suffers from certain disadvantages such as influence from substrate. Tortorelli [23] used this technique to evaluate the room temperature elastic properties of Cr_2O_3 scales. For Cr_2O_3 scale on chromium (oxidised at 850 °C), the elastic modulus was obtained to be 272±62 GPa which was compared with that of bulk sintered Cr_2O_3 and a similar value of 273±17 GPa was obtained. It is mentioned that the surface roughness of the oxide scales and influence of substrate limit the accuracy of the measured values.

Assuming that fracture starts from pre-existing flaws in the material, one of the main challenges is the determination of flaw sizes, since the scales are very thin. The point of crack initiation is also difficult to determine. Optical methods can be used to determine the composite defect size in the oxide scale, as in the case of [49, 54]. Composite defect size is an equivalent defect size that depends on the interaction between defects in the oxide scale and their positions. This has been used in calculation of fracture toughness of oxide scale grown on Nimonic 75, which ranges from 2 MPa$\sqrt{\text{m}}$ at 700 °C to 4.5 MPa$\sqrt{\text{m}}$ at 950 °C [49]. The vibration method was used for determining fracture strains grown on mild steel, which ranged from 0.1% at 600 °C to 0.23% at 900 °C [55]. Fracture and spallation of an oxide scale can be detected through the use of acoustic emission [22]. This is based on the principle that these events produce audible signals. The acoustic emission setup was used together with a four-point bending setup in order to determine the fracture strains of oxides in mild steel [56]. The critical strain decreased with increasing thickness, it varied from about 0.5% for 10 µm thick oxide to about 0.2% for 40 µm thick oxide. The aforementioned methods have a basic flaw that they are affected by the influence of the substrate at some levels. Since the

properties of the isolated oxide cannot be measured using these methods, the values are affected by residual stresses in the oxides as well, which is critical in determining factors such a fracture strain. Nagl *et al.* [24] saw in the case of NiO that accounting for residual stresses in the scales brings down the actual fracture strain by a significant amount (Figure 2.1). It also shows the previously mentioned influence of temperature, which allows for higher strains before failure, due to creep. Measurement of intrinsic oxide properties is more beneficial than fracture measurements of oxide scales under different conditions, because intrinsic properties can be used to predict fracture under any conditions.

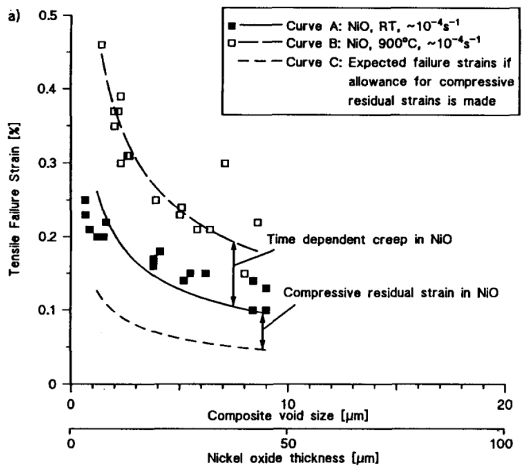

Figure 2.1: Fracture strains in NiO scale. Dotted line shows fracture strain accounting for residual stresses [24].

Information regarding the cleavage of oxides is also important as the fracture path in oxide scales can be transgranular. Many oxide materials show a strong tendency for cleavage in particular planes. Computer simulations on perfect surface for different crystallographic planes in Cr_2O_3 show that the difference in energy during relaxation is minimum for $\{10\bar{1}2\}$ plane (rhombohedral) and therefore was argued to be more likely to be seen during cleavage [57]. In another study on Cr_2O_3 and Al_2O_3 by Sun *et al.* [58], the same is seen for both of the oxides with the rhombohedral plane (r-plane) having the lowest change in surface energies. In both of the above studies, the basal plane (c-plane) has the highest change and is not expected to show any form of cleavage. For understanding the position of different planes, please refer to Figure 2.2. The reasoning has also been based on the atomic positions, where the vacant cationic sites are arranged along the r-plane, which can facilitate cleavage [59, 60].

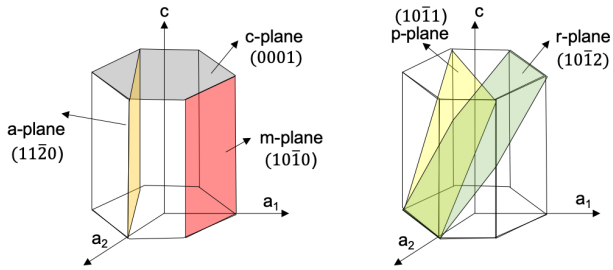

Figure 2.2: Schematic of hcp unit cell showing different crystallographic planes.

Rhombohedral cleavage has been seen experimentally in Cr_2O_3 through AFM, where flat surfaces were obtained on this plane [61]. One of the older studies for Al_2O_3 report cleavage on the *p*-plane (Figure 2.2) and the reasoning is based on the increased bond length between atoms on this plane [62]. Pishchik *et al.* [63] report that though Al_2O_3 does not show any strong cleavage facets, single crystals can be cleaved through the *m*, *a* and *p*-plane. Dedicated single crystal tests through microcantilever bending has been performed by Norton *et al.* [64] on Al_2O_3. It was seen in this study that the fracture surfaces of cantilevers oriented for the *m* and *a*-plane show smooth facets, but the one oriented for *c*-plane does not show a clear cleavage facet. Also, there was no significant difference in fracture toughness for the different planes. Same was reported for cubic zirconia by Henry *et al.* [65] where no significant difference in fracture toughness is seen even though theory suggests that the {110} plane is weaker than {100} plane. Schultz *et al.* [39], suggest in an earlier work that fracture toughness of crystallographic planes could be used as the criterion for predicting cleavage. But it is clear from the aforementioned results that it cannot be applied to all systems. Same is the case for the surface energy criterion where the crystallographic planes with higher surface energy also show cleavage in the case of Al_2O_3. For Cr_2O_3, which has as much importance in engineering applications as Al_2O_3, no experiments have been performed to demonstrate this. Therefore, dedicated experimental tests need to be performed more on these two systems to understand what happens at a single crystal level as well. With the advancement in focused ion beam (FIB) technology, it is possible to prepare samples at the microscale with ease and high precision, and perform experiments using nanoindenters and micromanipulators. Single crystal tests can also be performed on polycrystalline materials, as shown in [65].

2.3 Micromechanical testing

The mechanical properties of materials are directly linked to their microstructure. Therefore, there is a drive towards measurement of mechanical properties

at the microscale. The mechanical testing of materials at the microscale is referred to as micromechanical testing. Testing at the nanoscale with the use of in situ instruments in TEM is also possible, but the focus will be on testing at the microscale in the SEM in this section since it allows the probing of volumes that can be related to the macro properties of the material. In the case of polycrystalline materials such as alloys and ceramics, controlled micromechanical testing enables the targeting of individual grains, grain boundaries, etc, thereby building knowledge on single crystal and grain boundary properties. This is also important for testing of features whose size is in the µm regime, such as thin films, secondary phases, etc. Nanoindentation is one of the most common techniques used for measuring hardness and elastic modulus where bulk samples could be used and at the same time the probing area would be in the micro/ nano scale. Other forms of testing which are often used are microcantilever bending [25, 31, 66, 67], micropillar compression [27, 68, 69], micro-tensile testing [70], etc. One of the main challenges for microscale testing is how to prepare samples at those scales. Techniques such as photolithography and selective etching could be used for many materials such as semiconductors, but is not viable for many other materials. The FIB milling technique plays a very crucial role in sample preparation without which it would not have been possible to apply micromechanical testing to many materials. It allows the preparation of different microscale geometries with high precision. Nanoindenters are typically used in micromechanical testing and they can be either ex situ or in situ, meaning they can be standalone (for ex situ) or as an attachment to SEM or optical microscope (in situ). They typically consist of a high precision displacement sensor attached to the probe that indents/ bends the specimen and a load cell is placed below the sample to measure the load response. In addition to nanoindenters, micromanipulators attached with force sensors have also been used in the field of micromechanical testing. In the following sub sections, descriptions of different micromechanical techniques are given.

2.3.1 Nanoindentation

This is the simplest and the first developed technique for micromechanical testing. It was developed in the early 1970s and has become one of the most commonly used techniques to measure hardness and elastic modulus of materials at the microscale. The earliest hardness measurements such as Brinell (spherical) and Vickers (square pyramidal) depended on the application of a macro load and measurement of the impression created by the tips on the material to calculate hardness. With the advent of nanoindentation, also known as instrumented or depth sensing indentation, the load and the displacement are continuously measured and the hardness value can be obtained without the requirement of imaging the impression. It consists of a displacement sensor

with a sub nm resolution and force sensor with resolution in the micronewton range. Due to the load and displacement ranges measured, this instrument requires shielding from vibrations and the environment to lower noise and reduce thermal drift issues.

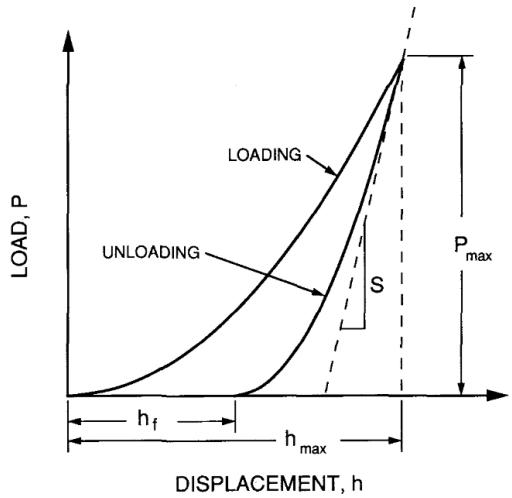

Figure 2.3: A schematic of load-displacement curve generated by nanoindentation [71].

Figure 4.8 shows a schematic of the load-displacement curve generated from a nanoindentation experiment. The required values for calculation of hardness and elastic modulus have been highlighted in the figure as well. The maximum load P_{max}, the maximum depth h_{max}, stiffness during elastic unloading, $S{=}dP/dh$, and the final depth h_f are the important parameters required for analysis of the obtained data [72]. Power law fitting can be used to describe the relation between load and displacement,

$$P = \alpha(h - h_f)^m \tag{2.14}$$

where α and m are fitting constants. The hardness can be determined as follows,

$$H = \frac{P_{max}}{A} \tag{2.15}$$

A is the projected area which is obtained as a function of the contact depth,

$$A = F(h_c) \tag{2.16}$$

The total depth (h_{max}) obtained from the experiment is the sum of contact depth (h_c) and sink in depth (h_s). The contact depth is defined at the vertical

distance along which contact is made, and the sink in depth refers to the surface displacement at the contact perimeter [71]. The Young's modulus and stiffness are related by the following equation,

$$S = \beta \frac{2}{\sqrt{\pi}} E_r \sqrt{A} \tag{2.17}$$

β is a dimensionless correction factor to account for the actual indenter shape. E_r is the reduced Young's modulus accounting for the combined deformation of the indenter and the sample, and also for the fact that the diameter of the indenter impression does not recover during unloading, only the depth does [71]. E_r and the Young's modulus of the material, E is related as follows:

$$\frac{1}{E_r} = \frac{1-\nu^2}{E} + \frac{1-(\nu_i)^2}{E_i} \tag{2.18}$$

E and ν are the elastic modulus and Poisson's ratio for the material, and E_i and ν_i are the corresponding values of the indenter material.

This technique opened up the hardness measurement to many systems which were not previously possible through macro and microhardness measurements, mainly thin films, since hardness could be measured with very shallow indentation depths. Over the years, several additions have been made to the technique, such as continuous stiffness measurement [72], high temperature nanoindentation [73], etc, making it more versatile. A large number of studies has been performed using this technique and it will be impossible to summarise all of them. The focus here will be on thin film systems since it is related to this work. Tortorelli *et al.* used nanoindentation to measure modulus and hardness of oxides grown on Fe_3Al [74] and thermally grown Cr_2O_3 [75]. They used taper polishing to check for influence of substrate for measured values in Cr_2O_3 and the validation was also performed using indentations on bulk sintered oxide. Suresh *et al.* [76] performed indentation on polycrystalline copper of thickness 300 to 1000 nm grown on a silicon substrate. Another application was in studying the strength of multilayer Al/ Si_3N_4 coating to relate layer thickness to strength. In situ oxidation monitoring and mechanical properties measurement in Nb based alloys at different temperatures has been made possible by this technique as well [77]. There are several cases where nanoindentaion enabled determination of fracture strain and elastic properties in oxide scales [78, 79]. This simple technique has become a platform for the development of several other techniques as well, which will be described in the following section. One particular application is the determination of fracture toughness through cracks formed during indentation, which will be described here.

Lawn *et al.* described a theory for development for cracks around sharp indenters [80] where fracture toughness (K_c) is related to radial crack length (c)

through the relation,

$$K_c = \alpha \sqrt{\frac{E}{H}} \left(\frac{P}{c^{3/2}} \right) \tag{2.19}$$

α is an empirical constant that depends on indenter geometry, P is the applied load, E is the elastic modulus, and H is the hardness. This method assumes that the crack length c is larger than the indent size and has a half penny-like shape. It is typically applied in the case of microhardness testing using a Vickers or Berkovich tip. Harding *et al.* suggest a modification to the system through the use of a nanoindenter and a cube corner indenter [81], which reduces the load thresholds required for crack formation in brittle materials. Other studies found disparities in the obtained values for different ceramics [82, 83]. Cook *et al.* [84] observed that the cracks developed beneath the indenter can be of many geometries. This is the main challenge with respect to this technique, as the shape of crack beneath the surface cannot be determined easily. Also, effects such as densification beneath cracks (for porous materials) can affect the fracture toughness values and therefore results in uncertainties in the values calculated using the model [85]. Modifications have been suggested for Equation 2.19 from experimental results [82, 83, 86]. Regardless, due to its ease of use, many brittle materials have been studied using this method [87–89]. In some cases, comparison with other techniques have been performed to ascertain the accuracy of obtained values [90, 91]. Advanced studies have been carried out using FEM [92, 93] and 3D FIB [94, 95] to obtain a better understanding of processes occurring beneath the indenter surface.

2.3.2 Microcantilever bending

Apart from nanoindentation, microcantilever bending is one of the most common methods in micromechanical testing. It essentially involves the bending of a micro-sized cantilever and measuring the load response from it. The force-displacement data generated from the experiment is then used to interpret mechanical behaviour of the material.

Consider a cantilever beam of prismatic cross section which has been loaded at the free end by applying a force F (Figure 2.4). The displacement of the beam at a distance x from the fixed end can be calculated using the equation,

$$\delta = \frac{Fx^2}{6EI}(3L - x) \tag{2.20}$$

where E is the elastic modulus, I is the area moment of inertia (e.g. $wh^3/12$ for a rectangular beam of width w and height h), and L is the length of the cantilever. The maximum displacement or the displacement at the free end is

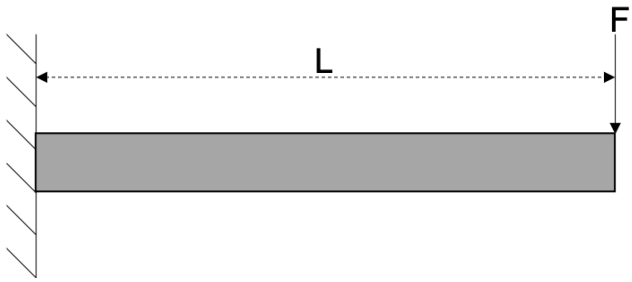

Figure 2.4: A simple cantilever beam with span length L and an applied force F.

given by,

$$\delta_{max} = \frac{FL^3}{3EI} \tag{2.21}$$

the bending stress in the outer fibre is given by the flexural formula,

$$\sigma_b = \frac{M}{I} y \tag{2.22}$$

M is the bending moment ($F \times L$), and y is the perpendicular distance from neutral axis. The corresponding bending strain is given by,

$$\varepsilon_b = \frac{3\delta}{L^2} y \tag{2.23}$$

The strain can be calculated using the relation, $\varepsilon = \sigma/E$, but requires an accurate value of E. Since δ and ε have a geometric relation, that can be used instead. Calculation of E using the beam formula in Equation 2.21 is possible, but it is highly sensitive to the geometry, especially the height of the beam ($I \propto h^3$). Also, in the case of analytical equations shown above, the assumption is of a fixed constraint, which is not valid for several cases. Take an example of hard coatings on soft substrates, a significant compliance of substrate during bending is possible and fixed constraint is not valid.

In practice, microcantilever bending is typically performed with the help of a nanoindenter, which can be ex situ or in situ. Depending on the dimensions, it is often favourable to use an in situ SEM nanoindenter, since the sample and the indenter tip can be visualised, enabling easy alignment of the indenter tip to the cantilever beam (Figure 2.5). This technique has been used for studying of mechanical properties as early as 1988, when Weihs *et al.* used it for evaluating Young's modulus and yield stress of silica by using an ex situ nanoindenter [66]. Ericson *et al.* performed fracture tests on silicon using this technique as well, but using a specially designed in situ SEM nanoindenter [67]. In both of these cases, cantilevers could be prepared using etching techniques applicable for semiconductor materials.

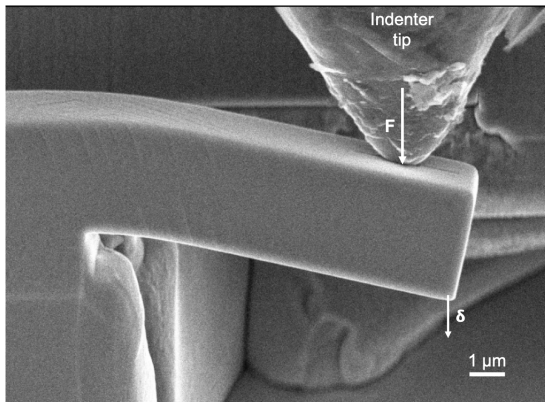

Figure 2.5: SEM image showing microcantilever bending of alloy 718plus FIB milled cantilever.

The real boost in this technique occurred due to the advent of focused ion beam (FIB) machining. Motz *et al.* used FIB machining for preparing microcantilevers in copper and used it to demonstrate the strain gradient plasticity theory [96]. Around the same time, Maio *et al.* devised a method for measuring fracture toughness of thin films through notched microcantilever bending tests [25]. This paved the way for microscale fracture toughness testing in several different materials such as thin films, interfaces, single crystals, etc. Different cantilever geometries were used, depending on the location. Cantilevers made on the surface of the material away from the edges were usually triangular [28, 64, 97] or pentagonal cross section [25, 31, 65], whereas the ones prepared on sample edges could be rectangular or square cross section [96, 98, 99].

In a detailed work by Dugdale *et al.* [31], microcantilever bending was used to determine the nature of crack propagation in an oxidised grain boundary. This study determined that in the case of stress corrosion cracking of Alloy 600, the crack progressed through the oxide metal interface and not through the oxide. The interaction of grain boundary particles with the crack was also studied using this technique. This study was extended in a recent work by Dohr *et al.* [28], which examines the role of surface oxide scales on top of oxidised grain boundaries. With the help of microcantilever bending experiments, it was shown that the surface scale helps in delaying crack initiation at grain boundaries, which is an important result in the field of stress corrosion cracking. The mechanical behaviour of grain boundaries in a ductile aluminium alloy was demonstrated by Kupka *et al.* [100] using blunt notches. Fracture toughness of many single crystals were also measured with ease [65, 98, 101, 102]. Another important application was the fracture toughness of interfaces of coatings [103, 104], which cannot be performed using other conventional techniques. Abad *et al.* [29] used this method to determine frac-

ture toughness of oxide scales and the fracture mode in oxide layers, where the whole cantilever was prepared from thick oxides grown on steels in liquid metal coolant environment. Camposilvan *et al.* used microcantilever bending to measure microscale properties of zirconia [105]. It was seen that the failure stress was about 4 times larger than standard sized specimen. The size effect plays an important role in determining the properties, as small sized specimens would have very less or no intrinsic defects. Size dependence for plasticity [98, 106] and fracture toughness [107] has also been studied in detail. The testing technique itself has been modified over the years. A straight notch on the cantilever leads to an unstable crack growth. Therefore, alternate FIB notching techniques have also been developed which allows stable crack growth, such as chevron notches [97, 108] and bridge notches [109]. The testing has also been extended to cases where crack tip plasticity could be present, using the J-integral method [110–112].

Some aspects need to be considered while performing fracture experiments using cantilever technique. Since the notch is fabricated using FIB, there is a possibility that ion implantation affects the measured value. This has been analysed in several studies [102, 113]. The chevron and bridge notch geometries aid in circumventing this issue. In some cases, comparison has been performed with FIB notched and natural cracks [110]. Comparison with other micromechanical techniques is also one way of assessing the FIB influence [102, 113]. FEM has been used as well to evaluate the influence of notch geometry, radius, etc [114]. Norton *et al.* [64] and Best *et al.* [113] have evaluated the influence of notching currents on the obtained notch radius and hence the influence on fracture toughness values. Best *et al.* state that below 10 pA of milling current, a sharp notch can be obtained and the measure values reach close to the values measured through techniques uninfluenced by FIB. So, if proper preparation and testing techniques are used, microcantilever bending can be a powerful tool for evaluation of fracture in a wide range of materials.

2.3.3 Micropillar compression

Micropillar compression, or microcompression refers to microscale compression testing of a pillar of close to uniform cross section using a flat punch, in a nanoindenter. This technique was developed by Uchic *et al.* [69] to study size dependent plasticity in Ni_3Al (Figure 2.6). Since then, this technique has been used to test deformation behaviour at small scale. The pillars are machined using FIB and can be of circular [69, 115] or square cross section [116]. In the case of circular cross section, lathe milling technique is used to obtain micropillars of high quality with little taper [117]. Annular milling can also be used for circular pillars, but results in a larger taper. But it has been observed that the yield stresses are about 4 times higher for magnesium pillars of the

same orientation milled by lathe milling in comparison to annular milling which is due to FIB damage resulting from longer exposure in the former case [118]. The force displacement curve obtained is interpreted in terms of engineering stress and strain curve by converting the load to stress using the pillar cross section, and displacement to strain using initial pillar height [117]. It has been seen in several studies that the yield stress of the material is significantly higher at microscale than in bulk [69, 115, 119, 120]. Another interesting effect observed through micropillar compression tests is the brittle to ductile transition in silicon at room temperature, where Östlund *et al.* [121] saw that the material transitioned to a ductile regime between 310 to 400 nm of pillar diameter. Room temperature plasticity was observed in otherwise brittle single crystal sapphire was observed by Montagne *et al.* [27], and the slip planes were identified as well (Figure 2.6). Since the experiments were performed on single crystals, the critical resolved shear stresses were also calculated.

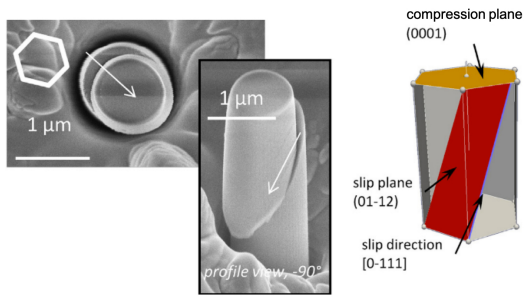

Figure 2.6: SEM image of deformed Al_2O_3 micropillar with the identified slip plane shown [27].

As is the case with any technique, micropillar compression also suffers from some demerits. One is the surface damage of the prepared samples caused by FIB. Comparison of FIB and lithography prepared gold specimens showed significant difference in strength [119]. FIB damage by gallium on surface of specimens has been studied in detail by Kiener *et al.* [120], where it is also stated that annealing at high temperatures can reduce the damage, but it will affect the dislocation structure in the material as well. Another source of error is the misalignment between the flat punch and the pillar, which can lead to underestimation of elastic modulus and also abnormal deformation behaviour [122]. Zhang *et al.* [122] also list out some recommendations such as an aspect ratio (height to diameter ratio) of 2 to 3, and that the taper should be minimised since it can lead to overestimation of elastic modulus. The issue of friction between the indenter tip and the top surface of the pillar cannot be solved. In the case of macro testing, a lubricating layer is used to minimise friction, which cannot be done at the microscale [117]. Friction prevents elastoplastic buckling, which can occur with the onset of plasticity. A theoretical treatment along with the experimental results, and finite element

modelling can lead to highly useful results in this technique. Combined with the reduction in sample preparation time in comparison to micro-tensile and microcantilevers, this is a powerful technique to measuring elastic and plastic properties of materials.

2.3.4 Micropillar splitting

This method was developed by Sebastiani *et al.* [123] in 2014 to measure fracture toughness in ceramic thin films. It is based on sharp indentation testing of FIB milled micropillars, which generates cracks in the pillar and results in its splitting. This method retains the simplicity of indentation fracture toughness testing and provides some advantages over it as well. The measurement of cracks lengths is not necessary post testing. Also, if the height to diameter ratio of the pillar is maintained above 1, residual stress effects are circumvented which provides a huge advantage for testing of thin films. The substrate effects are also removed in such cases since the indentation depth is typically very small before splitting occurs. Since the crack develops from the bulk material under the indenter, FIB influence is minimised as well. The biggest challenge for this method is the generation of a model to describe measurement of fracture toughness based on the fracture load. The fracture toughness can be described by the formula,

$$K_c = \gamma \frac{P_c}{R^{3/2}} \tag{2.24}$$

Where P_c is the fracture load, R is the pillar radius and γ is a dimensionless coefficient which depends on the elastic modulus (E) to hardness (H) ratio of the material. A cohesive zone finite element model was developed which considers the pillar as an isotropic and cylindrical material and a Berkovich indenter which is considered as rigid. The main aim of the model was to generate the relation between fracture toughness, critical load and the pillar radius (Equation 2.24). So, if the E/H ratio is known for a material, γ can be calculated from the data in this study and fracture toughness can be calculated. However, the use of Berkovich tip limits visibility and it is difficult to position the indenter tip on the centre of the pillar due to the tip geometry. A cube corner indenter is much sharper and is easier to use for such experiments, especially in an SEM. A study on the effect of tip geometry was carried out [124], which calculated the γ values for cube corner geometry as well (Figure 2.7).

Figure 2.8 shows a typical micropillar splitting test using a cube corner indenter. The SEM imaging enables the proper placement of the tip on the pillar and to retract the tip after fracture. This technique was used by Lunt *et al.* [125] to profile the fracture toughness at zirconia-porcelain interfaces for dental application. They were able to test 60 pillars along the interface using a

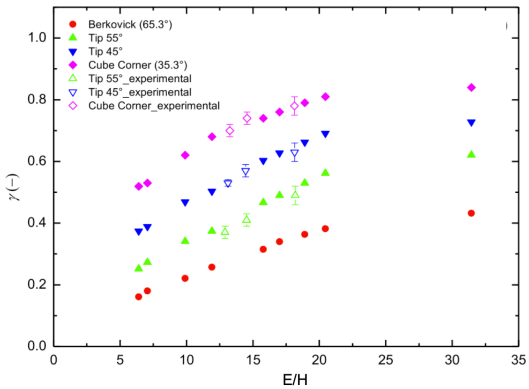

Figure 2.7: Graph showing the variation of γ with E/H ratios for different tip geometry [124].

cube corner indenter. Since the FIB preparation time for a micropillar is much less than that for a notched cantilever, better statistics can be obtained in a shorter time using this technique. Lauener *et al.* used micropillar splitting to perform a thorough study on silicon with regard to various factors influencing the results of this technique [126]. They prepared pillars using lithography and FIB (both gallium and xenon) to compare the effects of ion damage. It was seen that for smaller diameter pillars (< 10 µm) the FIB did influence the obtained results when compared to the ones prepared by lithography. Another factor that affected the results was the positioning on the tip, the further away from the centre, lower was the toughness. Due to the simplicity of this technique, it is gathering importance in the fracture toughness measurements of coating and other brittle materials. One main demerit of this technique is that it can only be used for brittle materials, since the critical radius for crack generation in metals is high.

2.3.5 Stable crack growth techniques

Some micromechanical testing methods have been developed to evaluate fracture toughness in a stable crack growth mode since the cantilever techniques typically lead to unstable fracture. Some of the most used ones will be described in this section.

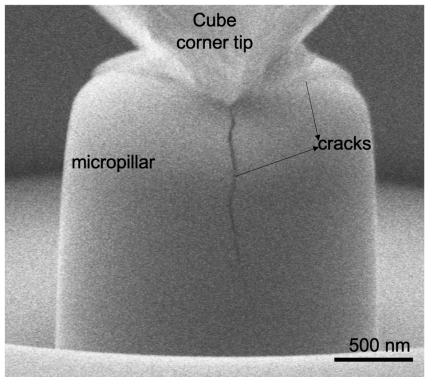

Figure 2.8: Micropillar splitting experiment showing fracture

2.3.5.1 Fixed beam bending

In this geometry, a cantilever milled using FIB fixed on both sides is used (Figure 2.9). In this case, the cantilever shape needs to be milled at the edge of the specimen. This was demonstrated by Jaya *et al.* [127, 128] as a method for fracture toughness evaluation of (Pt,Ni)Al bond coats.

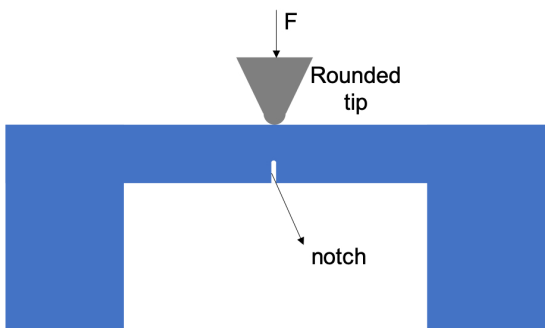

Figure 2.9: Schematic of a single notched double clamped beam.

The fracture toughness is calculated as per notched cantilever equations and validations by comparing with simulations have also been performed. It is a recently developed technique and has also been used for the fracture studies of diffusion aluminide bond coats [129]. A recommendation of length to width ratio between 4 to 8 has been proposed. The notch length to depth ratio should be between 0.3 and 0.5. The alignment of the tip and the notch should be accurate to have mode I loading, and the tip should not create an impression on the beam [102]. The disadvantage of this method is that the notching is done from the side and so the quality of notch is not as good as in the case of

cantilevers. Also, high stresses at the clamped regions can lead to failure at the supports as well [128]. To counter these issues, Cui *et al.* has proposed a modified bowtie geometry which can be prepared on the edges of the sample with a chevron notch [130]. Figure 2.10 shows a milled bowtie geometry with a chevron notch, from which it is clear that the stresses are concentrated near the notched region thus preventing failure at the supports.

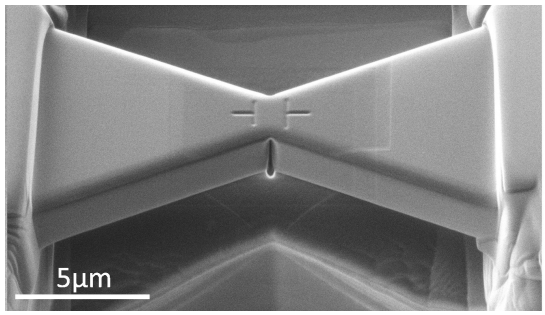

Figure 2.10: SEM image of Bowtie clamped geometry with chevron notch [130].

2.3.5.2 Double cantilever beam (DCB)

Liu *et al.* [131] described a method for measuring fracture toughness of hard coatings through stable crack growth using a notched double cantilever beam geometry (Figure 2.11). A notch is FIB milled to the centre of the geometry and a flat punch is used to compress the shoulders of the milled geometry. This causes a tensile load perpendicular to the direction of load application and the crack starts propagating.

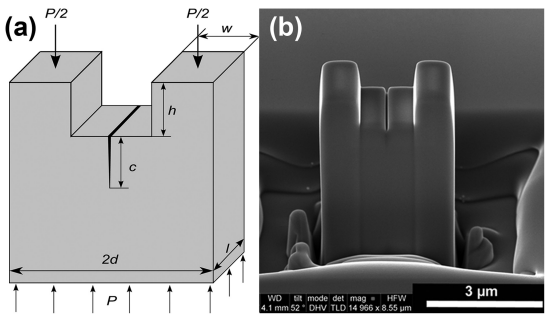

Figure 2.11: (a) Schematic of double cantilever beam geometry; (b) SEM image showing FIB milled DCB [131].

The fracture toughness can be calculated using the formula,

$$K_{Ic} = \sqrt{3}\frac{(e - \mu h)}{bd^{3/2}}P_c \tag{2.25}$$

d is the half width of the specimen, b is the width parallel to the notch, $e = (d-w)/2$ where w is the width of the shoulder, μ is the coefficient of friction between indenter and the sample. Figure 2.11(a) shows different notations used for dimensions of the DCB. Being a recently developed method, it has been used in a few studies in measurement of toughness for different systems [102, 132, 133]. Reliable results depend on the consideration of factors that can affect the results. Beam dimensions need to be such that the two arms are of same width, since symmetry is of importance. Also $w = d/2$ and $(h + a) > 4w$ should be followed as well. To ensure mode I loading, the flat punch should be parallel to the top of the specimen and larger than the $2d$. The validity of the test depends on the straightness of the crack and also whether plastic deformation of the shoulders take place or not [102].

A similar geometry has been proposed by Sernicola *et al.* [134] based on the macro geometry proposed by Lawn (Figure 2.12(a)) [135]. A wedge indenter is used to perform stable crack growth studies (Figure 2.12(b)) from which the fracture energy can be calculated directly. The advantage of this method is that the geometry is relatively simpler and the load values and coefficient of friction are not required for the calculation of fracture energy.

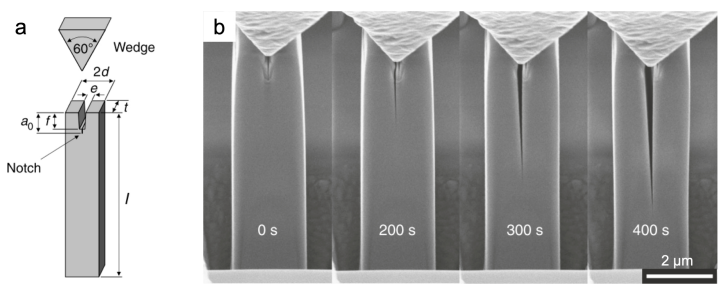

Figure 2.12: (a) Schematic of wedge splitting of double cantilever beam; (b) Stable crack growth during wedge splitting of DCB [134].

2.3.6 Advanced testing

This section will briefly mention the most recent advancements in the field of micromechanical testing aimed at enabling testing in more demanding conditions.

2.3.6.1 Hydrogen embrittlement

Hydrogen embrittlement (HE) is a process where a metal is affected/ embrittled due to exposure to hydrogen. It affects the performance of a variety of metals and alloys. It has been mostly studied macroscopically through mechanical testing such as tensile tests, even though the process is atomistic. Barnoush *et al.* proposed a nanoindentation based technique to evaluate the effect of hydrogen embrittlement [136]. It uses an ex situ nanoindenter attached with a 3 electrode system which could add electrolyte in controlled amounts 2.13. This setup was used to perform nanoindents on single crystal nickel submerged in electrolyte to demonstrate the interaction of hydrogen and has been extended to several other materials [137]. This is further developed to incor-

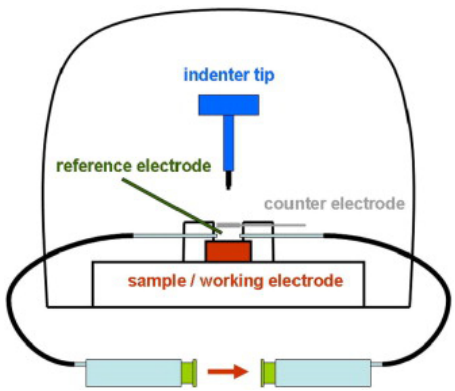

Figure 2.13: In situ hydrogen charging setup for nanoindentation [137]

porate micropillar compression into the testing of FeAl [138], which revealed the effect on hydrogen on dislocation nucleation seen in the form on increased plasticity in the micropillars. The study has been extended to notched microcantilevers tested in electrochemical cell by Hajilou *et al.* [139]. A similar approach aided in the identification of role of hydrogen in phase transformation of a metastable high entropy alloy [140]. In situ SEM testing was also performed where the cracking of notched microcantilevers were compared for high vacuum conditions, and low vacuum condition in an ESEM where water vapour is present and hydrogen can affect the material [141, 142]. The use of hydrogen plasma for in situ micro-tensile testing in SEM was performed by Wan *et al.* [143]. Recently, Kim *et al.* [144] developed an electrochemical cell for in situ charging of hydrogen in an SEM where the effect of hydrogen on different alloys could be monitored using the electron beam and nanoindentation could be performed on the top surface when the hydrogen charging is done through the bottom surface of the specimen.

2.3.6.2 High temperature testing

The simulation of real conditions is necessary for micromechanical testing in order to understand the mechanical behaviour of materials and its mechanisms in service conditions. High temperature micromechanical testing offers such a platform where processes such as deformation can be studied at various temperatures for different materials, providing insight into their behaviour under these conditions. High temperature nanoindentation has existed for over two decades. Lucas *et al.* [145] developed an equipment with nanoindentation capabilities from -100 °C to 75 °C. Smith *et al.* [146] modified a standard nanoindenter to perform indentation experiments up to 500 °C. This led to many modifications of ex situ nanoindenter with separate heating for the indenter tip and the sample stage to allow for temperature matching. For in situ SEM based nanoindenter (Alemnis AG), a modification was proposed by Wheeler *et al.* [147] for experiments up to 500 °C (Figure 2.14). These techniques have been used in various studies which was previously not possible due to experimental limitations. Wheeler *et al.* used microcompression at room temperature and 500 °C tests to assess the performance of hard coatings. Several other studies have used microcompression at elevated temperatures to identify deformation mechanisms, size effects, strain rate sensitivity, etc [148–151]. This has also been used in microcantilever bending tests to evaluate fracture toughness at higher temperatures [113, 128]. Currently, the temperature limit for in situ SEM testing is 1000 °C.

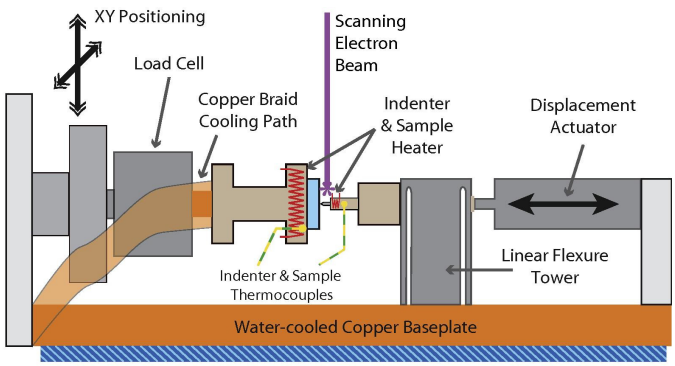

Figure 2.14: Schematic diagram of heating system used in Alemnis in situ SEM nanoindenter [73].

There are several issues related to in situ testing at higher temperatures. One is the need for better materials for indenter tip apart from diamond since it can oxidised above 400 °C in non vaccum environments. Even if used in SEM in a vacuum chamber, reaction with the material being tested is of big concern. Alternatively, materials such as cubic boron nitride (cBN), tungsten

carbide (WC), etc are used for testing at higher temepratures. These materials are subjected to a higher wear rate when compared to room temperature experiments. Temperature matching between the sample and indenter surface is another critical issue if left unchecked can lead to significant thermal drift and wrong temperature measurements. Thermocouples are required near both the sample and the tip so that thermal matching can be achieved with relative ease. The thermal drift in high temperature testing is much more significant because even a small temperature difference can lead to a heat flow, producing spurious results and incorrect conclusions. Some issues are specific to in situ SEM testing. The use of alternating current in heater for such equipment can resulting in a wobbling of images in the SEM. At temperatures higher than 525 °C, radiation from the tip and sample can lead to degradation of image contrast [73].

2.3.6.3 High strain rate tests

In situ micromechanical testing is typically quasi-static, which is due to limitations of the mechanical design and speed of data acquisition. High strain rate tests such as impact tests are of industrial importance as in the case of materials used in the automotive industry. Earlier attempts have been made at impact testing of polymers using a pendulum based actuator [152]. High speed indentations were performed in a study by Hay *et al.* to map the hardness in a solder material, where individual indents took a time of just 3 seconds [153]. Another approach was also in the case of nanoindentation where the strain rate dependence on hardness values of aluminium were measured by Phani *et al.* [154] where strain rate of 1000 s^{-1} were achieved. Recently, a high strain rate testing based on intrinsically displacement controller were developed by Guillonneau *et al.* [155]. The load cell in the typical setup is replaced by a rigid stage and the indenter tip by a piezo actuator which measures the load and displacement signals. This system is able to perform indentations up to a constant strain rate of 1000 s^{-1} and micropillar compressions up to 100 s^{-1}, which has been demonstrated with an example of nanocrystalline nickel [155]. Best *et al.* [156] used this technique for conducting a high number of impact tests at the microscale on CrN coated tool steels at room temperature to 500 °C. Another application was in the compression testing of silica micropillars over a wide range strain rates from 0.0008 to 1335 s^{-1} [157]. This revealed a ductile to brittle to ductile transition in the deformation of the micropillars. Such high strain rate testing capabilities opens doors for high cycle fatigue testing in situ SEM at different temperatures. Also, a wide range of processes can be studied, which was not possible previously.

CHAPTER 3

Materials

This chapter describes the materials that were used in this study. The oxide scales were thermally grown through oxidation exposures at high temperatures. The initial base material chosen was Alloy 718plus, a superalloy which is representative of high temperature materials used in critical applications and also has Cr_2O_3 as its protective oxide scale. Experiments were also carried out on Cr_2O_3 thermally grown on pure chromium to obtain thicker oxide scales. Due to the need for cleavage fracture studies on Cr_2O_3, single crystal wafers were used.

3.1 Oxidation of Alloy 718plus

Alloy 718plus is a nickel based γ' (Ni_3(Al,Ti)) strengthened alloy developed recently (Figure 3.1(a)). The nano sized γ' precipitates (Figure 3.1(b)) provides precipitation strengthening. It is very similar to Alloy 718 in composition, but half of the Fe content is replaced with Co and the Al/Ti ratio is increased. It has a maximum operating temperature of 704 °C.

For the oxidation exposures, coupon sized samples of Alloy 718plus of dimensions $15 \times 15 \times 3$ mm were cut using a low speed saw and the surfaces were

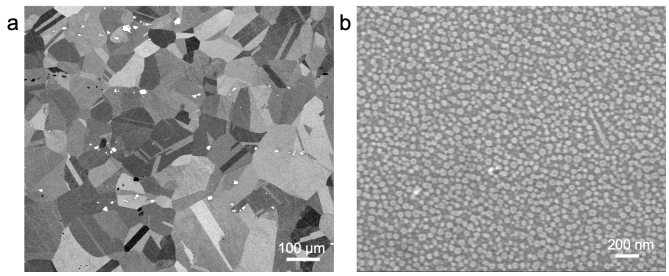

Figure 3.1: (a) SEM backscatter image showing microstructure of alloy 718plus; (b) γ' precipitates in the alloy.

mechanically polished using SiC papers up to 1200 grit size and diamond suspensions of 3 and 1 µm. The exposures were done in an alumina tube furnace at 700 °C in a pure oxygen environment for 100 hours. This yielded an oxide layer which was roughly 200 nm thick, measured from FIB cross sections. TEM lamella was prepared along the cross section of the oxidised alloy to analyse the microstructure of the formed oxide using STEM and EDS. Imaging was performed using a TEM in STEM mode to obtain microstructural and chemical information. The generated oxide consisted of different layers (Figure 3.2(a)), the top layer being a mixed spinel of $(Ni,Co)(Fe,Cr)_2O_4$ followed by a layer of fine grained Cr_2O_3, and internal oxide of Al_2O_3 (Figure 3.2(b)). This is very much in agreement with the oxidation mechanisms for such superalloys [3]. Details regarding preparation and testing of this oxide can be found in **Paper I**.

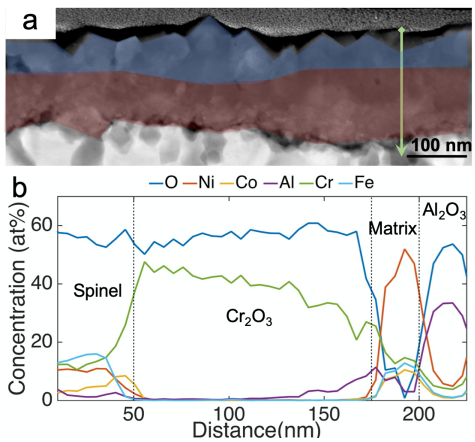

Figure 3.2: (a) Oxide layer thermally grown on alloy 718plus after 100 hours exposure (blue - spinel, red - Cr_2O_3); (b) EDS line scan of oxide scale showing different layers (green line shown in (a)).

3.2 Chromia (Cr_2O_3)

Chromia or chromium(III) oxide is a corundum structured oxide which occurs in nature in the form of a green coloured mineral known as eskolaite. The primitive unit cell is trigonal where the oxygen atoms are arranged in a hexagonal closed packed arrangement and the chromium atoms occupy 2 of the 3 octahedral sites (Figure 3.3). Cr_2O_3 has a very high melting point (2435 °C) and has hardness close to that of α-Al_2O_3. Cr_2O_3 is the only solid form of chromium oxide that is stable at high temperature. It is used in pigments due to its green colour and also as abrasives due to its hardness. However, our focus will be on its application as a protective oxide scale. Chromium is added in the form of an alloying element in many materials so that when they are operating at high temperatures, it leads to the formation of a Cr_2O_3 layer, which is dense, thin, and prevents further oxidation.

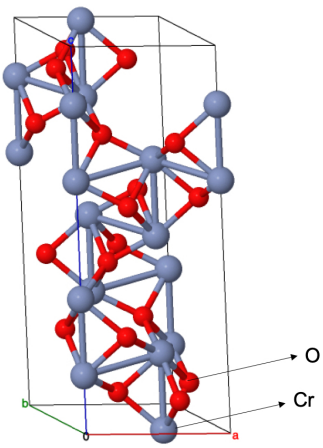

Figure 3.3: Unit cell of Cr_2O_3 showing corundum structure.

3.2.1 Oxidation of chromium

For the oxidation exposures, pure chromium of 99.97 % purity was used to prepare coupon shaped specimen of dimensions $15 \times 15 \times 2$ mm. The coupon surfaces were mechanically prepared using SiC papers and diamond suspensions to generate a scratch free surface. The isothermal exposures were conducted in an alumina tube furnace at 700 °C in an oxygen environment for different times, and it generated oxide scales of thicknesses as shown in Figure 3.4. In all cases, the oxide layer consisted of smaller equiaxed grains covering the surface with some grains growing larger (Figure 3.4). Scale thickness was measured from FIB cross sections. The oxide scale generated from 480

hours exposure that was a couple of microns thick was used for preparation of microcantilevers (Figure 3.5(a)). The oxide microstructure was further examined by preparing a TEM lamella of the oxide layer cross section and imaging was performed in transmission mode in the SEM. The oxide layer reveals a duplex morphology with an inner layer consisting of equiaxed grains and an outer layer of larger grains, which is in agreement with literature [158–161]. The presence of voids is seen both at the oxide-metal interface and within the scale, which has been observed previously as well [158, 162]. TKD performed on the oxide scale reveals a texture close to (0001) for the larger grains (Figure 3.5(b)). The details can be found in the experimental section of **Paper II**.

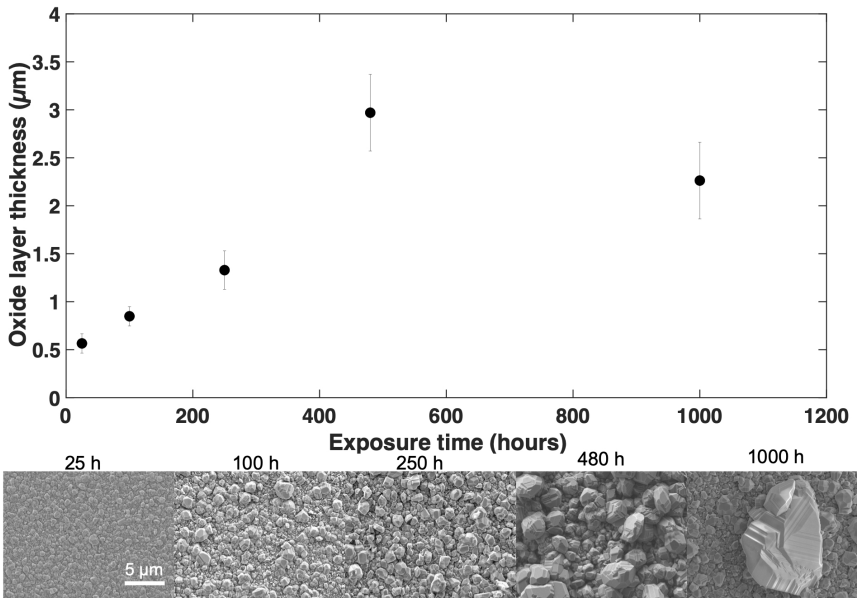

Figure 3.4: Oxide thickness for different oxidation exposure times. The corresponding SEM images of the oxide scale surface is shown as well.

3.2.2 Single crystal Cr_2O_3

The examination of cleavage planes in Cr_2O_3 required single crystals of known orientations. Single crystals of Cr_2O_3 of different orientations grown by Verneuil process were purchased from MaTecK GmbH, Germany. Wafers with (0001) and $(11\bar{2}0)$ planes perpendicular to growth direction were used in the studies for determining the active cleavage planes. The single crystals were obtained in the form of wafers of dimensions $5 \times 5 \times 0.1$ mm. The surface was polished using silica suspension to allow EBSD to be performed to determine the exact

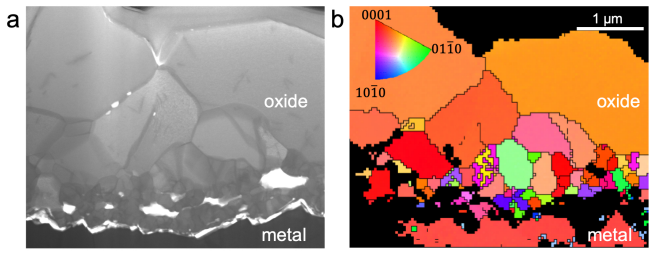

Figure 3.5: (a) Transmission SEM image of Cr_2O_3 grown for 480 hours; (b) inverse pole figure map of the area in (a).

orientation of the crystals. This is needed to orient the crystals during FIB milling of microcantilevers targeting various cleavage planes. Details regarding this can be found in **Paper III** and **Paper IV**.

CHAPTER 4

Experimental techniques

This chapter describes the various experimental techniques that were instrumental in the progress and completion of this work. The methods specifically developed for this work have also been described under the corresponding section headings.

4.1 Scanning electron microscopy (SEM)

SEM is one of the most versatile electron microscopy techniques. It enables the examination of a wide range of materials from the nanometre to the micrometre scale. The analysis of bulk specimens with a high spatial resolution (a few nanometres) [163] is achievable using SEM. It uses a focused electron beam with energies in the range of 1-30 keV for imaging. The beam is scanned over the area of interest which generates a set of signals due to the interaction between the electrons and the specimen. The image in an SEM is generated by the use of these signals. The main signals generated are the secondary electrons (SE) and backscatter electrons used for imaging, and characteristic X-rays used for chemical analysis. Some advanced detectors are also used in SEMs to generate different contrast and to enable imaging under various conditions.

SEM has been instrumental in the completion of this work and has been used extensively for different purposes, which will be summarised in the following sections.

4.1.1 Imaging

The primary use of SEM in this work was for imaging. The microstructures of the materials used were visualised, which provides a lot of information such as grain size, grain morphology, presence of precipitates, surface conditions, etc. The sample surface needs to be metallographically prepared to generate a flat and defect free surface so that the grains and precipitates in the material can be visualised. Taking the example of alloy 718plus which was used in the work shown in **Paper I**, prior to their thermal exposure, the microstructure was studied. A small piece of the alloy (roughly 20 × 20 × 5 mm) was cut using a low speed saw and was mounted on a conductive Bakelite resin using a mounting machine (180 °C for 5 mins). The surface preparation consisted of initial grinding steps using SiC papers up to grit size of 1200 for 2 minutes each. This is followed by polishing using diamond suspensions of 3, 1 and 0.25 µm for 10 to 15 minutes each. As a last step, oxide polishing using silica suspension of 0.05 µm size was carried out for 2-5 minutes so that the damage layer generated due to grinding is removed/ minimised. Ultrasonic cleaning in ethanol is performed for 2 minutes between each of the above steps. This ensures that the impurities from one step is not transferred to the next. After oxide polishing, the surface was wiped using a tissue very carefully in order to remove the silica particles, and the ultrasonic cleaning was done for 10-15 minutes. This recipe was obtained after some trials of varying the time and loads used in each steps, and works for many Ni based superalloys. The sample was then imaged in a SEM, using a backscatter detector, and it was revealed that the material was not heat treated. Since the alloy was not in the desired conditions, heat treatments were performed to generate equiaxed grains and also γ' precipitates to simulate the conditions in which the materials are used. After heat treatment, similar sample preparation steps were performed as described before and the microstructure was was visualised again. The microstructure showed equiaxed grains with some primary carbides along the grain boundaries (see Figure 3.1(a)). To check whether precipitates have formed, electrolytic etching had to be performed using oxalic acid on the prepared specimen. The size of γ' precipitates are a couple of tens of nanometres, which is not easy visualise in the SEM. The interaction volume needs to be minimised which can be done by reducing the voltage. But the secondary and backscatter detectors are not very efficient at these voltages. So, the imaging was performed in a Zeiss Ultra55 FEG SEM using in-lens detectors, which can provide high resolution under low voltage conditions. A 30 µm aperture was used at 1kV voltage to minimise the interaction volume and to bring out the surface fea-

tures clearly. The working distance has to be maintained below 5 mm since the generated electrons from the specimen do not have a high energy and can get scattered over longer working distances. Care needs to be taken at this point that the sample does not crash into the pole piece. The precipitates were visualised clearly using this imaging technique (Figure 3.1(b)) and it was confirmed that the alloy was in the desirable condition.

Similar procedures as mentioned previously were used to analyse the grain size of pure chromium samples used in the work done in **Paper II**. After thermal exposures, the oxide scale was imaged in an SEM in the secondary electron mode, since it provides very good topographical contrast. A voltage of 5 kV was used and the smallest aperture was used to provide better resolution. Figure 3.4 shows the Cr_2O_3 layer generated, in which the features such as the grain facets can be seen. Thus, a rough estimation of the grain sizes in the thermally grown oxide layers could be obtained. Another important use of imaging was in the measurement of dimensions of all prepared microcantilevers. Low voltage conditions were used in all cases to obtain a good resolution. The use of in-lens detectors was preferred since it has better resolution than secondary electron detectors.

The major part of this thesis, which is micromechanical testing would not have been possible without an SEM to visualise the sample during testing. This is especially necessary for testing using the Kleindiek micromanipulator setup (will be described in the following sections), since no displacement sensor is available. Images are recorded at a rate of 1 Hz and image analysis is later used to measure displacement of the microcantilever during testing. The imaging conditions for testing in the Kleindiek setup which was done in FEI Quanta 200 FEG ESEM were 10 kV voltage and a 30 µm aperture, while working distance is in the range of 10-15 mm. The working distance is larger in this case because of the micromechanical test setup, which limits how close to the pole piece the sample can be taken. The tests performed using the Alemnis setup were mostly done using similar imaging conditions, but in a Zeiss microscope. In both of these test setups, SEM allows easy alignment of the indenter with the sample, and also provides a live view of deformation of the samples.

4.1.2 Electron backscatter diffraction (EBSD)

EBSD is a microanalysis technique used in the SEM in order to obtain crystallographic information from crystalline materials. It can be used to deduce the crystal structure, identify phases, reveal texture, etc. When high energy electrons strike a specimen surface, back scattered electrons are generated which undergo Bragg diffraction. The intersection of the diffraction cone and a phosphor screen placed near the specimen produces a pattern of Kikuchi lines called

as electron backscatter patterns (EBSP). This is used as the basis for identification of the orientation of the crystal and the phase. The EBSD detector consists of a phosphor screen that can be moved inside the SEM chamber towards the sample which is place at a steep angle (70°) to the normal plane of the beam (Figure 4.1). Typically, a voltage of 20 kV is used under high current conditions in order to generate a high number of backscatter electrons. The lateral resolution of this technique is limited by the backscatter resolution of the microscope due to the larger interaction volume. Unlike other SEM techniques the horizontal and vertical resolutions are not the same for EBSD due to the high tilt angle.

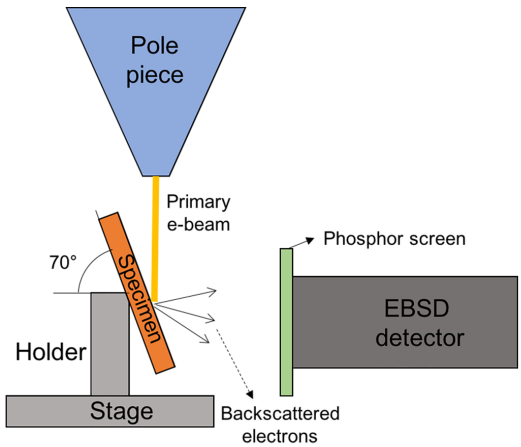

Figure 4.1: Schematic of EBSD setup inside the SEM

EBSD was used for multiple purposes in this work. One was in the case of flat Cr_2O_3 cantilevers, where the orientations the the grains on the surface was measured so that it could be later compared with the images of the fracture surface and deduce the mode of fracture as transgranular or intergranular. Focused ion beam (FIB) milling was used to prepare the surface for EBSD. Low milling currents of 10-100 pA were used to mill away the rough surface of the grains at a gracing incidence angle to minimise ion implantation. For EBSD, a defect free surface is important, otherwise Kikuchi patterns will not be clear. The sample is mounted on an SEM stage using a 70° pre-tilted holder. This can be done using stage tilt as well, but depending on the bulkiness of the sample and location of the detector, it can be difficult. It is recommended to mount the sample on aluminium stub using silver paste or using clamps. The use of carbon tape can lead to mechanical drifts, especially due to the high tilt angle. The sample should be such that the surface where the data is recorded has to face the EBSD detector. The detector is usually retractable and can be brought in close to the sample after aligning the stage so that the sample faces the detector (see Figure 4.1). The maximum insertion distance

is recommended, but it depends on the geometry of the sample. The working distance was maintained close to 10 mm, but depends on the model of the detector and its position in the SEM chamber. The voltage is maintained at 20 kV and a high current condition is used to generate more electrons. The size of the map and the pixel size (step size) is decided based on the feature being analysed. Since the oxide grains were a mixture of sub-micron to few micron sized grains, a fine step size of 20-50 nm was used. Once the area of interest is chosen and the image parameters are adjusted, the stage is not moved again and the sample rests in the chamber for a while to stabilise. This is followed by mapping and the time required for mapping depends on the exposure time for the EBSD camera, step size and the area being mapped. The phase being analysed need to be known since the software does a comparison of the projected Kickuchi patterns to its database to identify the orientation. The results only consist of orientations and pixel positions. The patterns need to be saved for each pixel if a reanalysis needs to be done. The obtained raw data has to be processed to obtain meaningful results.

Processing of EBSD data can be done using software associated with the model of the detector being used. In our case, an Oxford detector was used, so their Channel5 software was used for most analyses. Different forms of maps can be obtained from the raw data. One map that is of very good use is the band contrast map, which is a map showing the Kikuchi band contrasts obtained for each pixel. The advantage of this is that even if orientations in certain pixels are not identified, they still have a band contrast value and the resulting map reveals the microstructure of the sample being analysed, even though the exact orientations are unknown, as in the case of the analysed Cr_2O_3 cantilevers. An inverse pole figure (IPF) map was also used, which shows the sample directions (e.g. growth direction) in terms of crystallographic directions of the material. This gives an idea on the crystallographic texture of the material. In addition to these, Euler maps can also be obtained which gives the absolute orientations of grains with respect to a reference coordinate system.

EBSD was also useful for identification of the exact orientation of single crystal Cr_2O_3 samples used in **Paper III** and **IV**. In this case mechanical preparation of the surface was used. The purchased wafers were already polished. Therefore, only the final polishing step, that the oxide polishing to remove the surface damage layer was done. The procedure of mechanical preparation by grinding and polishing is the same as the one described in the previous section. For the oxide layers, obtained from oxidation exposures, transmission Kikuchi diffraction (TKD) was performed which provides a higher resolution compared to EBSD.

4.1.3 Transmission kikuchi diffraction (TKD)

TKD is a recent technique developed which is very similar to EBSD in operation, but can provide spatial resolutions as high as 2 nm [164]. In this case, an electron transparent sample is placed horizontally or at small angles (0 - 20°) to the stage and at very low working distances. The detector used is the same as that for EBSD. The geometry of a TKD setup is given in Figure 4.2. Due to the diffraction being generated from a smaller volume, the spatial

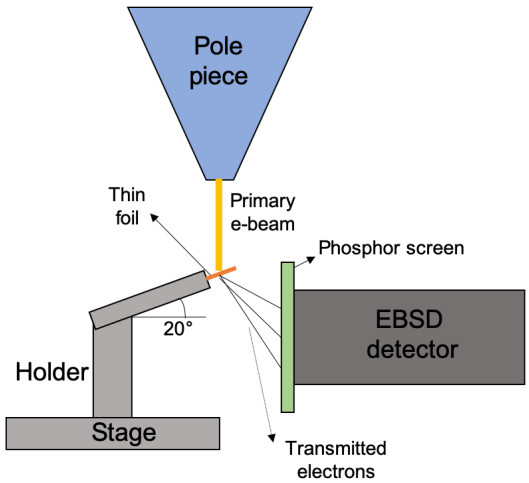

Figure 4.2: Schematic of a TKD setup inside the SEM.

resolution is higher and the diffraction patterns are mostly generated from the bottom side of the specimen [165]. Due to the low tilt angles, the disparity between horizontal and vertical spatial resolution is also reduced. Electron transparent thin foils of oxidised chromium was prepared using FIB. Standard TEM lamella preparation procedures are followed [166]. A special holder in which the TEM grid with the thin foil sample can be inserted is used, which is pre-tilted at 20°. The electron beam energy is maintained at 30 keV to ensure maximum penetration and high current conditions are used as for EBSD. The working distance in kept in the range of 3-5 mm, although it depends on the detector position and sample geometry, The step size used here is typically smaller than the one for EBSD, but it depends on the feature being analysed. For the oxide scales grown on chromium, step sizes 10-25 nm were used. The advantage of this technique was that the grain structure of oxide scale was revealed, which would not have been possible using EBSD due to limitations in spatial resolution. However, the obtained data quality depends on the thin foil sample quality. Typically, there shouldn't be any overlaps of grains along the electron beam path, i.e., the ideal sample would have just one layer of grains

along the thickness. The processing of data obtained from TKD is similar to that for EBSD, described in the previous section.

4.2 Transmission electron microscopy (TEM)

TEM utilises the interaction between sample and the electron beam during transmission. This was the first kind of electron microscope and the concept was proposed by Ernst Ruska. TEM has been commercially available since 1939 and has improved a lot over the years. The sample is in the form of an electron transparent thin foil which is typically < 100 nm thick. The electron beam usually has an energy of 200 or 300 keV, but there are TEMs that can be operated at lower energies. The higher energy is necessary to provide very good spatial resolutions. The best resolution obtained in a TEM is about 0.5 Å. TEMs are widely used for imaging, chemical analysis and also for obtained crystallographic information. The sample preparation can be through mechanical thinning, ion beam milling and also FIB milling. In our work, all thin foil preparation has been performed using a FIB since the samples are target specific and cannot be prepared using mechanical means. The main use of TEM in the current work has been in imaging of oxide layers and their chemical information, and also for the analysis of FIB damage during microcantilever milling.

4.2.1 Scanning TEM (STEM)

STEMs are modified forms of TEMs where a scanning coil setup is added in the electron beam column in addition to the electromagnetic lenses. Modern TEMs have the possibility to be operated in STEM mode as well. Unlike the case of TEM imaging, the electron probe is focused to a fine spot and scanned over the sample in a raster fashion. The images are obtained from different detectors. Bright field detectors are placed in the electron beam path. Annular dark field detectors are like concentric circles and they collect scattered electrons, and provides atomic number contrast. Atomic resolution images can be obtained in this mode, and the contrast can be interpreted directly, unlike the case of TEM. Since the electron beam can be scanned over the sample, it is also possible to obtain high resolution energy dispersive X-Ray spectroscopy (EDS) maps. STEM imaging was mainly used in this work to obtain an overview of the thermally grown oxide microstructure and to obtain chemical information on the oxides. An FEI Titan 80-300 FEG TEM was used for imaging and chemical analysis. The microstructure of thermally grown oxides of 718plus and chromium were both studied in the STEM mode at 300 keV. Standard alignment files available for the instrument was used and

small spot sizes were used to obtained higher resolution images. Figure 4.3(a) shows an example where the oxide microstructure for Cr_2O_3 grown on pure chromium can be seen with the help of bright field images. The dislocation network present in the metal below, possibly due to mechanical preparation can also been visualised clearly using this technique. In another case, high resolution STEM was used to identify the damage layer caused due to FIB damage and redeposition during FIB milling of cantilevers. Figure 4.3(b) is provided as an example to showcase the high resolution capabilities in STEM mode. However, the alignment procedure to obtain good HRSTEM images is complex, especially in the case of oxides, which are fine grained and have several intrinsic defects. Therefore, the redeposition analysis was done using high resolution TEM, since the alignments are comparatively easier.

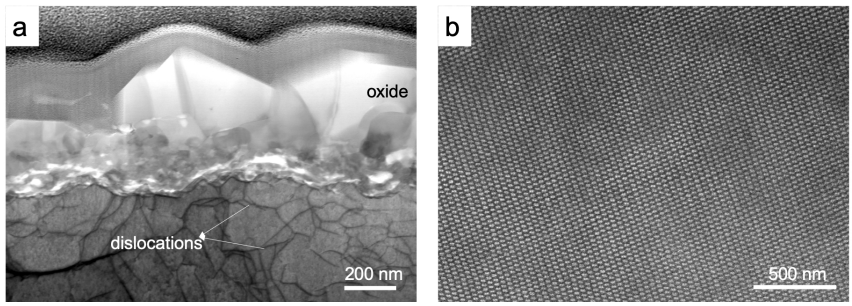

Figure 4.3: (a) Bright field STEM image showing oxide microstructure and dislocations; (b) HRSTEM HAADF image showing atomic columns in Cr_2O_3

4.2.2 High resolution TEM (HRTEM)

HRTEM is an excellent tool for the imaging of lattice and lattice defects in crystalline materials. A technique called phase contrast imaging is used to generate high resolution images of atomic columns. The image is formed by the interference between the direct beam and the diffracted beams that pass through the crystal. To enable this, either a very large objective aperture or no aperture is used so that it allows the passage of the direct beam and a bunch of different diffracted beams. To image atomic columns properly, it is a requirement that the crystal needs to be aligned in a high-symmetry direction, i.e., the zone axis condition needs to be satisfied. A zone axis is that direction to which two or more set of intersecting planes are parallel. However, the phase contrast images obtained using this technique as not easy to interpret. More details are required to isolate atom of one element to the other. However, since the current application was to identify redeposition layers which are typically amorphous, the analysis was relatively simpler. Figure 4.4 shows an example where HRTEM was utilised to identify the presence of redepostion on top of the

oxide layer after FIB milling. Fast Fourier transforms (FFT) are performed on selected areas to obtain patterns similar to electron diffraction patterns, which can reveal whether the area being analysed is crystalline or amorphous. Such an example in shown in Figure 4.4, where the oxide layer is to the left, as revealed by the associated FFT from that area, and the redeposition layer differs in appearance from the image and shows an amorphous nature, as revealed by the FFT.

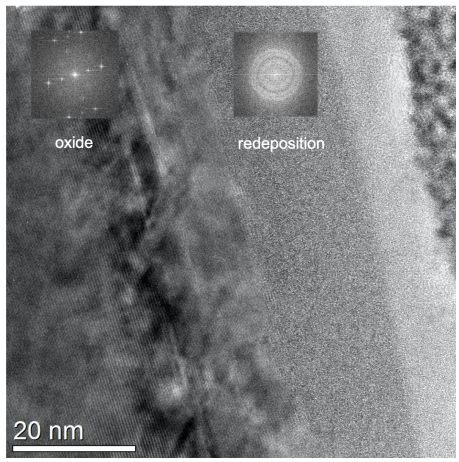

Figure 4.4: HRTEM image showing atomic columns of oxide and redeposition layer.

4.3 Focused ion beam (FIB) microscopy

The FIB is an instrument similar to the SEM in setup, but uses ions instead of electrons as the imaging source. This class of instruments have revolutionised the semiconductor industry with respect to nanomachining, enhanced etching etc. In the 1980s they were used mostly in semiconductor industries for masking and circuit repair [167]. They found their way into research laboratories only in the 1990s. One of the most important contributions of FIB to research is the means for target specific TEM lamella preparation. This instrument allows TEM sample preparation with a greater degree of precision than conventional methods at specific microscopic sites. Today, the most common form of FIB microscopes comes with a dual column; an electron column that is vertical and an ion column inclined at an angle to the electron column (angle depends on the manufacturer). The main application of FIB is for imaging and sputtering.

Unlike broad ion-beams used for TEM lamella preparation or preparing cross sections, FIB uses a highly focused ion beam. It uses a field ionisation source

with a size of about 5 nm in order to generate a very fine beam. The source used is usually a liquid metal ion source (LMIS) which can produce bright and focused beams. The source used in most of the cases is gallium due to its low melting temperature and low volatility. Recently there are some FIBs using xenon plasma as source in order to generate higher currents for sputtering of larger areas, but at the expense of the resolution. Since it is impractical to build huge electromagnetic lenses to focus ions, electrostatic lenses are used instead. Although the resolution depends on the beam shape and intensity, the sputtering resolution is material dependent. The stage for this instrument is designed to have a eucentric point, which aids in maintaining the field of view when the specimen is tilted towards the ion column. Imaging in a FIB can be performed thorough the usual detectors in SEM, SE and BSE detectors. In addition to that, ion-induced secondary electrons (ISE) can also be detected. The advantage of using ISE for imaging is a strong channelling effect created by these electrons, enabling a grain structure view in case of crystalline materials. In addition to the imaging and sputtering capabilities, FIBs are also used for target specific chemical vapour deposition (CVD). Secondary electrons generated by ion beams or electron beams can be used to crack hydrocarbon precursor gases in order to deposit materials such as platinum, tungsten, carbon or SiO_2 films. This can be used as support structures or protective films for materials science applications.

Some of the major applications of FIB in the field of materials science is mentioned below:

- *TEM lamella preparation* – This is one of the most common application of FIB in multiple disciplines of research. TEM lamella can be prepared from specific sites of interest using a widely known lift out method [166].
- *Atom probe tips* – Tips used for Atom Probe Tomography (APT) can be prepared from specific sites using FIB.
- *Micromechanical test specimens* – Specimens for micro-mechanical testing can be milled using FIB with a high degree of accuracy. Preparation of microcantilevers, micropillars, micro-tensile specimens, etc has been made simple through the use of FIB.

As the title of this thesis suggests, micromechanics forms the core of most of the experimental work conducted, which involves intensive sample preparation using FIB. The microcantilevers and micropillars used for mechanical testing are prepared using FIB. The preparation procedures are explained in the later sections where the geometries are described. For microcantilevers prepared on the edges of specimen, a 45° pre-tilted holder was used to mount the sample. This is to allow the milling of two perpendicular surfaces of the sample without the need for remounting them. Since the ion beam is at a tilt angle with respect

to the electron column (52° for FEI microscopes), the use of a pre-tilted holder also reduces the amount of stage tilt required. For TEM sample preparations, standard procedures were followed. An FEI Versa3D FIB was used for all FIB preparations. FEI has a comprehensive guide on TEM sample preparation and those procedures were followed. The only difference was in the case of platinum deposition. More amount of platinum needs to be deposited due to the surface roughness created by the oxide grains.

There are some aspects of FIB milling that one should consider in order to ensure optimal results. The sputtering of material using Ga ions causes ion implantation on the sample surface. This results in a damage layer of certain thickness which is amorphised. It also can lead to creation of point defects and dislocations. This is especially important in the case of TEM foils since and micromechanical test specimens. The preparation needs to be done carefully in order to minimise the damage as much as possible. The standard TEM preparation procedures were fit for producing good quality electron transparent foils for the imaging and analysis of oxide layers. For microcantilever preparation, multiple attempts were made to optimise the preparation parameters. In crystalline materials, the sputtering creates a surface roughness due to several factors such as surface diffusion, channelling effect etc. In order to obtain a cleaner surface, low currents for milling or a rocking stage can be utilised. This is important for TEM lamellae preparation and for FIB cross sections. Another situation is where the sputtered material can get redeposited in the nearby regions which decreases the sputter yield and require sputtering a second time. For micromechanical test specimens, this can alter the mechanical properties of the surface and can affect the measured values. It is therefor very important to be aware and to quantify redeposition in FIB prepared samples. In the case of Cr_2O_3 microcantilevers prepared using FIB, redeposition was observed on surface of cantilevers. The thickness of this layer was measured with the aid of HRTEM (see section 4.2.2). An idea for surface protection using free standing thin films was proposed during the course of our work. This will be pursued at a later stage.

4.4 Raman microscopy

Raman spectroscopy is an excellent optical technique that is used for structure determination of molecules. the principle is based on Raman scattering, which is the inelastic scattering of photons [168]. A monochromatic light source (laser) is used to illuminate the specimen, and it interacts with the specimen to produce elastic and inelastic scattering. The elastic scattering, which is also known as Rayleigh scattering does not provide useful information. The laser also interacts inelastically with the molecules of the specimen, which results in an increase or decrease of the laser energy characteristic to the structure of the

molecule. This principle can be used in generating a Raman spectrum that represents the signature of a particular molecule. The peak positions of the spectrum depend on the mode of vibration of the molecule and the intensity is proportional to the concentration of the component. Both the peak positions and relative intensity can be used to identify a molecule and its structure. One of the challenges is that the inelastic scattering part is only about 0.01% of the incident energy. This means that the detection of the inelastic part is difficult since Rayleigh scattering overpowers the output signal. Special filters are used to filter out or reduce the elastic part so that the Raman spectra can be obtained. Also, all molecules cannot be detected through Raman spectroscopy, the vibrational mode should result in a net change of dipole moment.

Confocal Raman microscopy combines an optical microscope and a Raman spectrometer [169]. However, the optical microscope is a confocal microscope, which is used to spatially filter out the analysis volume to the focus plane. The laser beam can be scanned over the sample by the movement of the sample stage and thus information can be obtained from a large region in the form of maps. Raman maps carry unique information regarding the presence of different phases and their locations as well. A sub-micron spatial resolution can be obtained using this technique. Apart from chemical and structural identification, Raman microscopy can also be used for measurement of residual stresses in materials. The presence of stress in the material causes a shift in the frequency of vibration and this is used to quantify the stresses present in the material [170]. Depending on whether the stresses are compressive or tensile, the peak can shift to the right or left (Figure 4.5(b)). If we take an example of Cr_2O_3, which is the oxide of interest for this thesis, the A_{1g} peak at 551 cm^{-1}, which is the most intense peak (Figure 4.5(a)), shifts linearly with respect to stress in the material. It has been show that the stress can be quantified according to the following equation [171, 172],

$$\sigma = -\Delta\nu \times 0.307 \tag{4.1}$$

where, $\Delta\nu$ is the shift in frequency caused by the stress and 0.307 is the shift stress coefficient calculated from high pressure studies on Cr_2O_3. This method was used in determining the residual stress distribution on thermally grown Cr_2O_3 scales (Figure 4.5).

In the present work, a WITec Alpha 300R Raman microscope with a green laser of wavelength 532 nm was used to perform Raman mapping. The sample was places using a glass slide under the objective lens of the optical microscope and 100x magnification was used to acquire an image. This is followed by adjusting the power of the laser so that a good signal to noise ratio is obtained. The mapping is performed with a step size of 1/3 µm, which is close to the spatial resolution attainable by this technique. The obtained data is processed to generate a map based on peak shift, which in turn shows the distribution of residual stresses. It could be seen that high compressive stresses were present

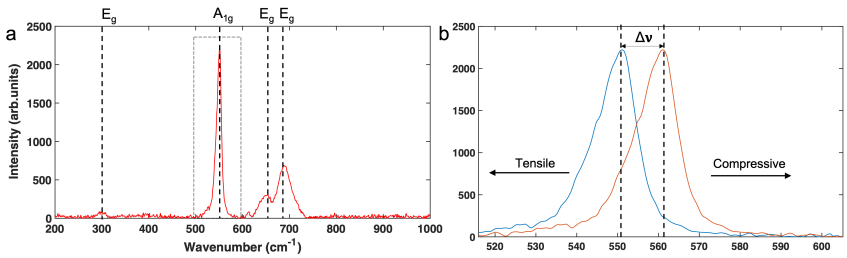

Figure 4.5: (a) A typical Raman spectra for Cr_2O_3; (b) Peak (highlighted in (a)) shifts under stress in Raman spectra.

in the oxide scale and the mapping gave an idea on spatial distribution of the stress.

4.5 Micromechanical test setup

Micromechanical testing requires specialised miniature test equipment, which are typically nanoindenters and in some cases, micromanipulators as well. This section describes the various test setups that were used for different experiments.

4.5.1 Kleindiek micromanipulators

It consists of a micromanipulator capable of precise movement along the 3 axes (two axes of rotation, and linear extentions/retraction) and a force measuring setup. Forces can be measured either through a force measurement sensor (FMS) for small forces or a spring table for larger forces. Figure 4.6 shows the setup placed in an SEM chamber.

It consists of the following components,

- *MM3A micromanipulator* - It is a precision robotic arm that is capable of moving along the three different axes and aid in manipulation of micro sized specimens. Different tips can be attached to the arm depending on the application. It can be controlled using a three-knob system, a joystick or a command based scripting system.
- *Force measurement sensor (FMS)* - It consists of a piezoresistive silicon cantilever which generates a voltage signal during bending. This voltage signal can be converted to a force signal by calibration it against a spring

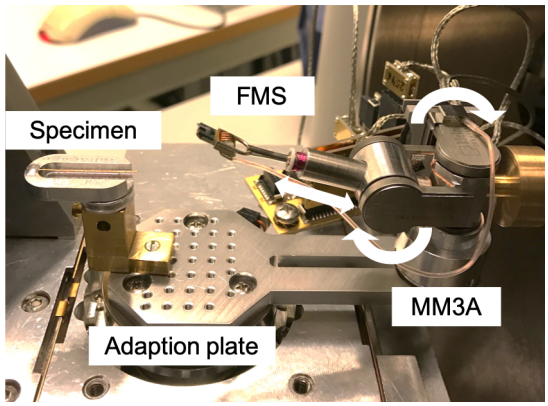

Figure 4.6: Kleindiek micromanipulator setup.

of known force constant. The calibration and recording of force can be performed through a software interface. It can be used to measure forces up to 360 µN and has an excellent force resolution about about 10 nN. Above this value the calibration of the silicon cantilever fails. The displacement is measured from a series of SEM images taken at an interval of 1 Hz. Figure 4.7 shows the image of FMS and the SEM image of the actual silicon cantilever that measures forces.

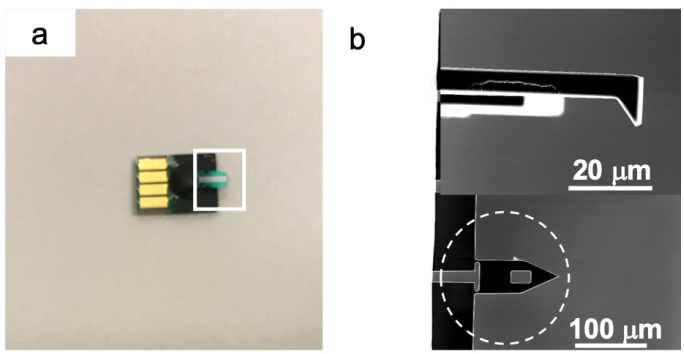

Figure 4.7: (a) Image of FMS sensor; (b) SEM images of the silicon cantilever.

4.5.2 Alemnis in situ nanoindenter

In situ nanoindenters have become a common part of micromechanical testing. Alemnis in situ nanoindenter is one such indenter which has been used in this

work. It is a high precision instrument that can be operated in true displacement control mode, unlike many ex situ and in situ nanoindenters which rely on load controlled mode for indentation. This is particularly interesting for fracture tests since a load controlled experiment during fracture would lead to crashing of the indenter tip on the sample. The instrument is compact enough that it can be loaded on the sample stage of an SEM. Figure 4.8 shows an image of Alemnis nanoindenter highlighting the different parts. It consists of a indenter head which is controlled by a piezo stack for high precision movement in the up and down direction, generally referred to as z direction. The indenter tip can hold a wide range of tip such as Berkovich, conical, cube corner, flat punch, wedge, etc. The sample is placed on a sample holder, which in turn sits on a load cell which has been calibrated. The load cell can be suited to requirements, and in our case a load cell calibrated up to 500 mN was used. The sample holder and load cell rests on a piezo stage which can be moved in the horizontal directions for sample placement. The indenter setup is mounted on the SEM stage in a horizontal manner or at a small tilt such as 20°. This is to enable the viewing of sample surface during indentation and other experiments. The indenter is equipped with a real time controller which

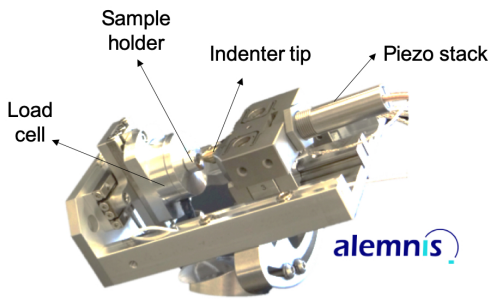

Figure 4.8: Alemnis in situ nanoindenter

manages data acquisition. The stage and the indenter tip can be moved with the help of a controller or the AMICS RT control software provided with the setup. The control software is used in designing and performing the experiments. In addition, a data analysis software is also provided, called AMMDA, which can aid in processing the data and generate output files to be used to plotting graphs. Testing protocols were developed for different purposes.

4.6 Micromechanical testing

This section describes all the micromechanical testing procedures that were developed for the oxide scales and single crystals used in this work. The sample preparation for the experiments is also described here since they are a

crucial part of the mechanical property measurement.

4.6.1 Deformation of thermally grown oxides on 718plus

The first part of measuring mechanical properties of oxide scales involved microcantilever bending of thermally grown oxides on alloy 718plus, which is chosen as an example to represent high temperature materials. The oxide layers developed from 100 hour oxidation exposure of alloy 718plus was roughly 200 nm thick. For testing such thin oxides, very good force resolution is required and that is the reason for using Kleindiek micromanipulator setup for the microcantilever bending tests, since the FMS provides sub-µN force resolution. **Paper I** shows the detailed results and discussion for this work.

The testing method entirely depends on the perfection of the prepared specimens. A special geometry was developed for microcantilevers so that the substrate and residual stress influences can be avoided. The rectangular geometry is modified as shown in Figure 4.9.

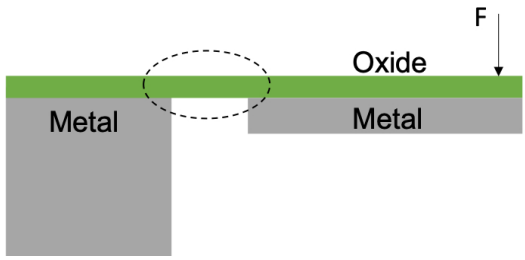

Figure 4.9: Modified cantilever geometry - region where substrate was removed has been highlighted.

The microcantilevers were prepared using an FEI Versa3D FIB. A small block of the oxidised superalloy (10 × 5 × 5 mm) is cut using a low speed diamond saw, and the cross section is polished. This was followed by broad ion beam milling on the cross section to obtain a flat surface perpendicular to the oxide layer surface. The sample is then mounted on a aluminium stub using silver glue (for electrical conduction and adherence). The stub is mounted on a 45° pre-tilted holder, which is then mounted on the FIB sample stage. The stage is then tilted to 7° (ion column is at 52° with respect to the stage) so that the ion beam is normal to the surface of the specimen. The first step is similar to that for a cantilever of rectangular geometry. High milling currents of 5 and 7 nA are used to isolate a rectangular slab from the edge of the sample. The stage is then rotated by 180°, which makes the cross section of the sample perpendicular to the ion beam. Undercutting of the rectangular slab prepared

earlier is done using the same milling currents, resulting in a fixed beam of rectangular cross-section, as shown in Figure 4.10(a). The next step is to remove the substrate over a small region (about 3 µm) near the support using a low milling current of 100 pA (Figure 4.10(b)). This frees the oxide from the substrate, thus preventing residual stresses and effects of substrate in the cantilever. The substrate metal is left behind for the rest of the cantilever length. This is to provide a support to the oxide scale and to prevent it from curling. The edges of the cantilever are then polished with a low FIB current of 100 pA to obtain a perfect geometry and to minimise the surface damage due to FIB. As a last step, the other end of the geometry is milled away to produce the final cantilever (Figure 4.10(c)). The SEM image in Figure 4.11 shows the final geometry of the cantilever. Note that the oxide is not visible in the SEM image and the thickness of the 'metal+oxide' portion is typically double of that for the 'free oxide' portion.

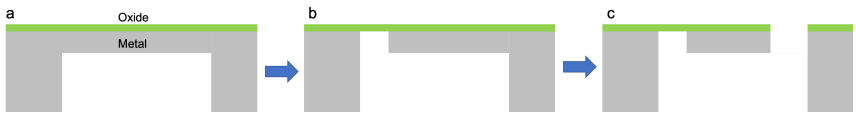

Figure 4.10: Different steps involved in milling of modified oxide cantilever geometry.

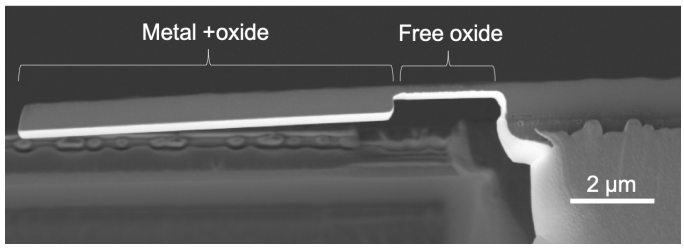

Figure 4.11: SEM image of FIB milled oxide cantilever

For this modified geometry, displacement equations were derived by considering it as a combination of two cantilevers. Details of the derivation can be found in supplementary material *section C* of **Paper I**. The displacement at the free end for this geometry was calculated to be,

$$\delta = \frac{F}{EI} \times g \tag{4.2}$$

where F is the applied load, E and I are the elastic modulus and moment of inertia of the oxide, and g is the geometric factor given by the formula,

$$g = L^2\chi - L\chi^2 + \frac{\chi^3}{3} \tag{4.3}$$

χ is the length of the isolated oxide near the support.

The bending tests were performed in an FEI Quanta 200 FEG ESEM. The Kleindiek micromanipulator setup is mounted on the SEM stage using an adaption plate, which allows the mounting of both the MM3A micromanipulator and sample on it so that the SEM stage movements result in the combined motion of the sample and manipulator. The FMS is then mounted on arm of the micromanipulator carefully using special tweezers provided by Kleindiek. The silicon tip (Figure 4.7(b)) is very sensitive and can break easily if not handled correctly. Before the start of experiments, the FMS is calibrated with a copper spring of known spring constant. The tip is used to bend the copper spring through a distance of 1µm, and the voltage change is used obtain a force constant since the spring has a known spring constant. This procedure is repeated a number of times by varying the contact point to obtain an average value of the force constant. The spring is then replaced by the sample, which is mounted in such a way that the oxide surface is vertical. In this way, the displacement can be recorded using SEM images without the need for tilt corrections. Next step involves the alignment of the silicon tip of the FMS with the width centre of the cantilever at the free end.Loading away from width centre can lead to twisting of the cantilever. A small stage tilt ($\sim 10°$) is applied to visualise the top surface on the cantilever. A line is milled along the centre of the cantilever to aid the placement of the tip. Once the alignment is performed, the stage is brought back to 0° tilt.

A set of small displacement bending tests are performed so that the bending is within the elastic region of the oxide. This is to calculate the stiffness of the oxide layer, which can later be utilised to calculate elastic modulus. The load is applied manually using the knobs on the control box for the micromanipulators. The SEM images are recorded at an interval of one second to measure the displacement of the cantilever using imaging analysis. The force is recorded by the FMS software associated with the setup. The elastic bending tests are followed by large displacement tests in which the microcantilever is bent as much as possible. In this case, the microcantilever can either fracture or show permanent deformation. In the case of fracture, the loading is stopped at that point. In the case of permanent deformation, a set of small displacement tests are repeated to compare the stiffness before and after testing, since a significant change in stiffness implies the presence of microcracks.

The obtained raw data needs to be processed to generate $F - \delta$ curves. The force data is obtained from the FMS software, but the values are averaged since the force is recorded at 4 Hz and displacement at 1 Hz. The displacement is calculated by image analysis using a simple MATLAB script for extracting pixel values from images. In each image, three points are chosen and their coordinates are recorded. One point is chosen anywhere on the fixed part of the sample, another at the contact point between the tip and cantilever, and the third point at the free end of the cantilever (Figure 4.12). The fixed point is tracked to get a sense of mechanical and thermal drift during the experiment

and its y coordinate is subtracted from that of free end displacement tracking point to obtain the displacement of the cantilever. This ensures that drift does not affect the measured value, since only the relative displacement is measured. During the bending, the FMS tip moves along the cantilever length. This means that the span length changes continuously and needs to be accounted for. Therefore, the load application point is also tracked, the distance between the loading point and the fixed end is calculated for each figure. This distance is used translate the force to the free end, in the form of an equivalent force (F_{eq}) using the equation,

$$F_{eq} = F_p \times \frac{\eta}{L} \tag{4.4}$$

Where F_p is the load measured by FMS, η is the actual span length recorded from each image, and L is the total length of the cantilever. So, the plotted $F - \delta$ curves are based on equivalent force and free end displacement.

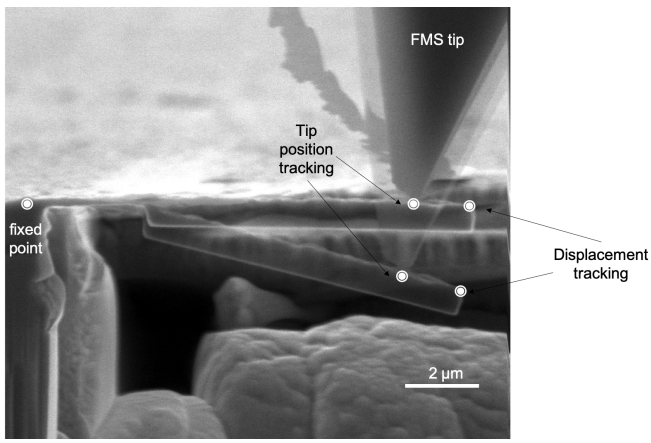

Figure 4.12: Overlaid SEM images recorded during cantilever bending of thermally grown oxides on alloy 718plus showing different tracking points.

The stiffness calculated from $F - \delta$ curves of small displacement tests can be used to estimate the elastic modulus (E).

$$E = g \times \frac{k}{I} \tag{4.5}$$

g is the geometry factor obtained from Equation 4.3, k is the stiffness, and I is the area moment of inertia. The use of analytical formula for elastic modulus calculation assumes a fixed support, which is not the case in reality as the support has definite compliance. This was compared using FE simulations, and it was calculated that E could be underestimated by about 5% by use of analytical formula (details in *section C* of supplementary material in **Paper I**).

Sources of errors

FMS calibration - Errors can occur in the calibration of FMS to convert voltage to force signal. The spring constant of the copper spring has an uncertainty of 10%, as reported by Kleindiek. The positioning of tip at the end of the spring can affect the value of voltage constant obtained. Therefore, the calibration was done multiple times by slightly varying the point of contact to determine the spread in the values and it was found that there is about a 5% variation in the voltage constant obtained through the calibration. To minimise errors, a number of calibrations are performed and the average value is taken as the force constant.

Misalignment - During bending test, the FMS tip should be in contact at the width centre of the cantilever. If the tip is away from centre, it can lead to twisting of the cantilever in addition to bending, which can be observed from imaging during experiment, This results in an error in force values and displacement as well. A line is milled using FIB during preparation of the cantilever to aid the correct placement of FMS tip.

Geometrical uncertainties – The cantilever is prepared using FIB, which can lead to uncertainties in dimensions, especially at the oxide-metal interface. In the calculation of the elastic modulus, it can be seen that thickness of the oxide is present as a power of three. So, the milling as well as the measurement should be done accurately in order to prevent large errors in elastic modulus calculations.

Horizontal force component - A point load applied to generate a large displacement will generate a force component in the x direction in addition to the applied force in y direction. This will affect the bending of the beam, for which a correction factor is required to correct the stress given by [173],

$$\sigma_{corr} = \sqrt{\frac{\tan\theta}{\theta}}\sigma \tag{4.6}$$

θ is the deflection angle at the loading point and σ is the uncorrected stress.

Friction - The sliding of the FMS tip along the top surface of the oxide during unloading induced what is thought to be a non-ideal bending of the FMS silicon cantilever. Consequently, the forces measured during unloading were lower than those measured during loading (Figure 4.13(b)). This effect is a particular feature of the micromanipulator setup used. It occurs only at large displacements, and therefore does not affect the stiffness measurements. Based on the normal forces and frictional forces at a certain angle θ (Figure 4.13(a)), The unloading to loading force ratio was calculated as,

$$\frac{F_{unloading}}{F_{loading}} = \frac{\cos\theta - \mu\sin\theta}{\cos\theta + \mu\sin\theta} \tag{4.7}$$

θ is the angle of the cantilever with horizontal and μ is friction coefficient. Figure 4.13(c) shows the effect of friction coefficient on the force ratio, which shows that the force drop can be close to 50% as seen in the experimental curves, if a friction coefficient of 0.3 - 0.5 is considered at an angle $> 30°$. Note that this correction was not utilised in **Paper I**, and was devised at a later stage.

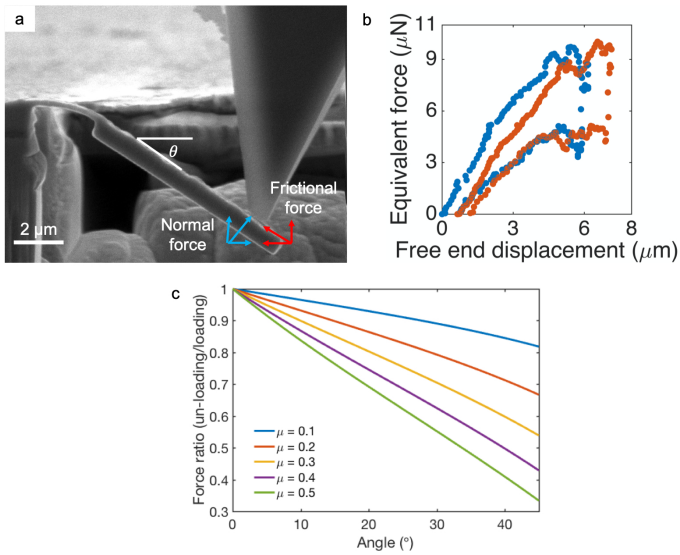

Figure 4.13: (a) SEM image showing normal and frictional forces; (b) $F - \delta$ curves showing force drop in unloading cycle; and (c) Plot showing how much the force can drop at a certain angle for different coefficients of friction.

FMS angle - Due to the geometry of FMS tip, the silicon cantilever on the FMS is often not parallel to the cantilever axis. This brings a change in the force values measured due to the difference in extent of bending of the silicon cantilever in FMS. To assess how much the angle affects the force values, a silicon cantilever of known orientation prepared using FIB was bent using different angles (α) of FMS, and it was noticed that as α increases the force drops significantly (Figure 4.14). The α angle needs to be kept minimum so that the force can be measured correctly.

Manual errors – There is a possibility of manual errors in the case of image analysis where a MATLAB script is used to calculate displacement by selecting different points in the images. It is essential to quantify the variation in displacement/force values calculated through image analysis.However, the uncertainties were more in the case of Kleindiek software provided for image analysis.

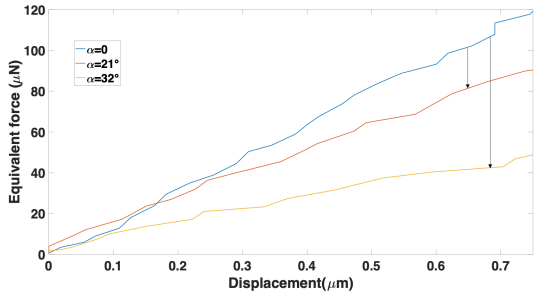

Figure 4.14: Effect of FMS tilt on measured force values.

4.6.2 Fracture properties of thermally grown Cr_2O_3

For measurement of fracture properties of thermally grown Cr_2O_3, which is detailed in **Paper II**, a similar geometry described in previous section was used. The only modification was the flattening of the top surface towards the free end, to facilitate placement of indenter tip (Figure 4.15). The micro-cantilevers were prepared using FIB in the same manner as described in the previous section.

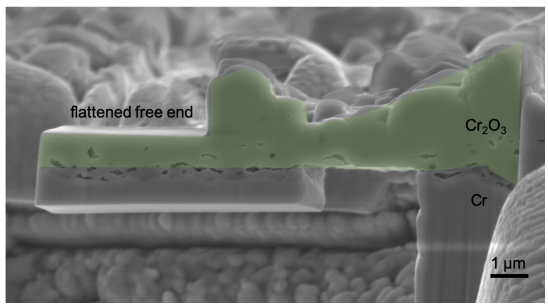

Figure 4.15: SEM image of FIB milled Cr_2O_3 cantilever.

The experiments consisted of both room temperature and high temperature tests, and therefore the Alemnis nanoindenter setup was used for testing. The sample was mounted on a copper stub using a high temperature cement and cured to obtain a good bonding of the sample with the stub. A tungsten carbide cono-spherical indenter of tip radius ∼1 µm was used fore the bending tests. The fracture tests at at room temperature and 600 °C were conducted in a displacement controlled mode with at 10 nm/s until fracture. The tip was manually retracted at fracture. All fracture tests consisted of fixed periods of thermal load drift measurement segments where the tip is not in contact with the sample surface. For the tests at 600 °C, the initial steps consisted of temperature matching, since the indenter tip and sample has independent

heaters attached to them. The temperature matching is done with the help of a series of indentations on the surface of the sample away from the cantilevers [116, 174]. A small region near the edge, but away from the cantilevers was flattened using FIB to perform these indentations.The direction of thermal drift during contact in the indentations corresponds to the difference in temperature and can be rectified according to the drift observed. For example, if the indenter tip is hotter, contact will lead to contraction of the tip and an increase in displacement will be observed. This procedure is repeated multiple times until the drift is minimised. This is followed by fracture tests using the same procedure as for room temperature tests. An additional set of microcantilevers were prepared on the sample with the same geometry, but the top surface was milled to remove the surface roughness throughout the length of the cantilever. This was to assess the influence of surface roughness on the fracturing mechanism and also to estimate elastic modulus. The room temperature tests were conducted using the Alemnis nanoindenter setup in displacement controlled mode. The first set of bending tests were small displacement tests to evaluate stiffness of the cantilever followed by fracture tests.

The raw data obtained from the experiments were evaluated manually using MATLAB. Linear fitting was performed on the drift segments to obtain the drift rate for each cantilever. This was then subtracted from the raw data to obtain the final $F-\delta$ curves. Since this response depends on the geometry, the force-displacement curves were converted to stress-strain curves ($\sigma-\varepsilon$). Since the geometry was complex, FEM was used to derive the geometric constants for each cantilever to obtain $\sigma-\varepsilon$ curves. The details of this procedure has been outline in *section C* of supplementary material in **Paper II**. The surface roughness was not accounted for in the FE models and the average height was used to calculated the geometric factors. The elastic modulus was obtained from slope of the generated stress-strain curves.

FE modelling was also used in evaluating the influence of surface features such as notches and bumps, and internal features such as porosity on stiffness of the cantilever. COMSOL Multiphysics 5.0 was used to perform linear elastic simulations on the cantilever geometry with actual dimensions, with addition of the aforementioned features. Figure 4.16 shows one such example where an extreme case of through thickness porosity and a surface notch is present. The stiffness of such a cantilever was compared with a cantilever of same dimensions, but with the height varied, as shown in Figure 4.17.

4.6.3 Fracture of single crystal Cr_2O_3

The observation of cleavage type of transgranular fracture seen in thermally grown Cr_2O_3 scales pointed towards the need for evaluation of its single crystal

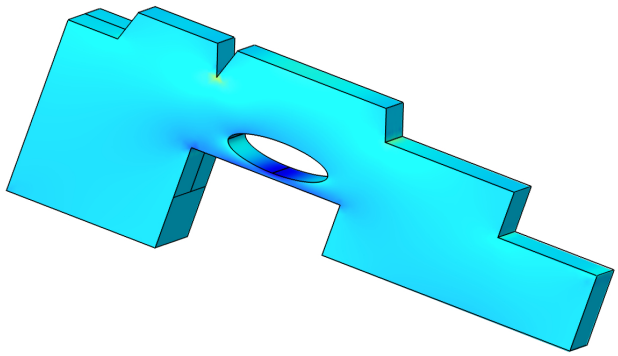

Figure 4.16: A example of FE model showing features such as porosity, surface notches, etc.

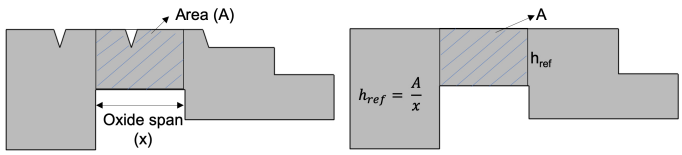

Figure 4.17: Schematic showing how a equivalent height for comparison of cantilevers is calculated.

properties. This was performed using single crystal wafers of Cr_2O_3. A microcantilever bending method was proposed to target different crystallographic planes in Cr_2O_3 to evaluate the preferential planes for cleavage. The idea was to prepare and test microcantilevers oriented in different crystallographic directions such that their tensile axis was perpendicular to the known cleavage plane for corundum structures. Figure 4.18 shows a schematic for the proposed method.

Since the cantilevers have to be oriented for particular crystallographic directions, preparation could not be done on edges of the wafer sample. They had to be FIB milled on the bulk surface away from edges of the samples. This meant that rectangular cross section cantilevers could not be prepared using FIB due to limitations in accessing the underside. For such situations, a triangular or pentagonal cross section is chosen as the geometry for the microcantilever. For our purpose, which was the experimental evaluation of cleavage planes, a pentagonal cross section was chosen since the top part is a rectangular section and it can be used to measure the angle of the cleavage plane using SEM images of side views. Figure 4.19 shows the schematic for the FIB milled pentagonal

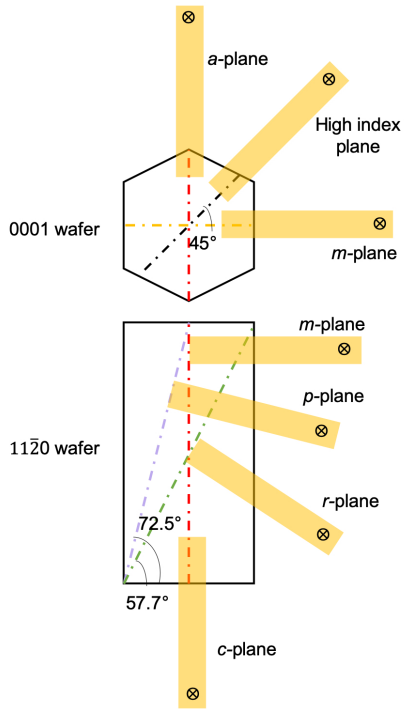

Figure 4.18: Schematic showing orientations of different cantilevers.

cross section microcantilevers. It should be noted that both unnotched and notched cantilevers were tested. The span length for unnotched cantilevers is calculated from the fixed end to the load application point and from the notch for notched cantilevers.

The single crystal wafers are of known orientation, but only the growth direction is known. So, the first step was to perform EBSD on the wafers to determine the exact orientation. This gives the exact position of the unit cell with respect to the edges of the wafers, and this information is utilised to determine the stage rotation necessary for each set of microcantilevers. The (0001) and (11$\bar{2}$0) wafers were used to make cantilevers in different directions. The angles between the different planes were determined using the c/a ratio for Cr_2O_3 from literature, which is 2.741 (details in *section B* of supplementary material in **Paper III**). For FIB milling of microcantilevers, the method outlined by Maio *et al.* [25] is utilised. The wafer is mounted on an aluminium stub using silver glue and is left to dry for a couple of hours. The mounted sample is then placed on the FIB stage and then an edge of the wafer is aligned horizontally/ vertically depending on the orientation of the cantilever to be milled. Then stage rotation is used to arrive at the orientation required.

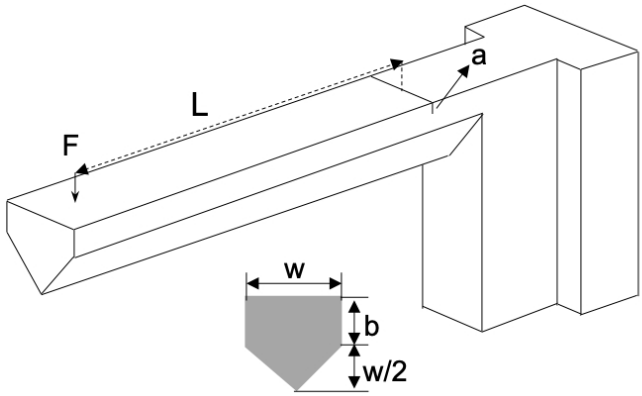

Figure 4.19: Schematic of pentagonal cross section cantilevers with FIB milled notch.

The stage is tilted so that the ion beam is perpendicular to the wafer surface. The initial milling was to produce a trench ('U' shaped from top view) so that a rough rectangular slab is produced that is only attached to the bulk on one side. This was done using milling currents of 5 and 7 nA. The next step was to undercut the rectangular slab using 3-5 nA of current, but at an angle of 45° in order to obtain a rough pentagonal cross section cantilever, The final steps involve polishing at 300 pA current to produce the final geometry. An overtilt of 1.5° is used for the final polishing to account for profile of the ion beam. A line roughly 2 µm was milled along the free end of the cantilever at the width centre to enable easy alignment of indenter tip for the experiments. For the notched cantilevers, the cantilever was carefully aligned vertically in the FIB image and a line was milled at 10 pA along the width. The milling time was kept below 100 s to avoid broadening of the notch due to drift. All prepared cantilevers were imaged in SEM to measure dimensions of the cantilevers. The prepared cantilevered roughly had a total length of about 15-17 µm, width about 3 µm, and the depth of the rectangular section ranged from 1.4-2 µm. For the notched cantilevers, the depth ranged from 0.4-0.7 µm.

Before the tests, a quick check of all the components of the Alemnis in situ nanoindenter is performed to ensure that the connections are right and are working. The initial set of experiments involve load controlled nanoindentation of fused silica samples using a Berkovich tip and the elastic modulus values are calculated. This value is compared with literature values for fused silica to ensure that the load cell is working as it should. This is followed by changing the indenter tip to cono-spherical (radius 1 µm) and also the sample. The sample is roughly aligned in such a way that the length of the cantilevers being tested is horizontal to the image plane (Figure 4.20). The cono-spherical tip makes the alignment easy due to axial symmetry, and aids in good visualisation of the contact point. The nanoindeter setup is allowed to remain in the SEM

chamber after pumping of vacuum for 20 to 30 minutes. This allows the stabilisation of the setup and tests are started when the load drift goes below 10 µN/min and displacement drift below 1 nm/min. This can be measured from the control software AMICS RT.

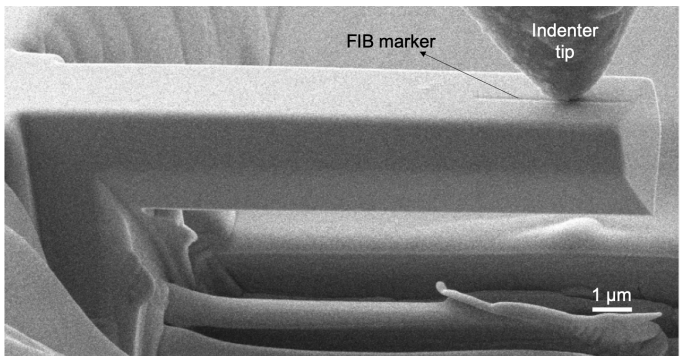

Figure 4.20: SEM image of pentagonal cross section cantilever with indenter tip shown.

The microcantilever bending tests start with small displacement tests to measure the elastic behaviour of the material. The loading profile shown in Figure 4.21 was used for these tests in displacement controlled mode. The initial 30 second segment with zero displacement is for measuring load drifts, which has to be subtracted from the raw data obtained from the experiments. These elastic bending cycles are conducted with increasing displacement for up to 1µm, which is followed by a thermal drift test to evaluate displacement drift. Load controlled experiments were conducted at a low load (750 µN) which was held for 1-2 minutes. This was followed by fracture test, which was displacement controlled. The indenter tip is withdrawn manually after fracture. The sample orientation is then changed manually for performing the same set of experiments on cantilevers of other orientations.

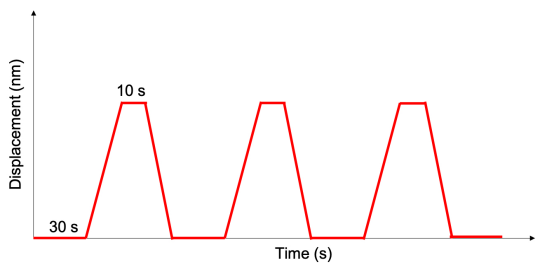

Figure 4.21: Loading cycle for small displacement tests.

After all fracture tests are completed, SEM images of the fracture surfaces are

taken from the side, top and front so that the cleavage plane of fracture can be determined through the images. The images are taken at a 70° tilt to minimise distortion due to tilt. After this, the angle of fracture surface with respect to length of the cantilever is determined using ImageJ software. Expect for top view images, other images require tilt correction for the correct determination of angles. The tilt correction for angles was performed according to,

$$\theta_{corr} = \tan^{-1}\left(\frac{\tan\theta}{\cos 20^{\circ}}\right) \tag{4.8}$$

Where θ is the angle measured from the SEM images. The corrected angles are then compared with angles for different crystallographic planes and thus the cleavage plane is identified.

The obtained raw data from the bending tests are processed using analysis software provided by Alemnis, called AMMDA. This software provides a fairly simple interface to perform drift corrections and obtain the final form of data. The initial part is the removal of load drift, for which the initial segments from the bending tests are used. A linear fit to these segments gives the load drift rate which can be subtracted from the raw data. The displacement thermal drift is evaluated separately from the dedicated load controlled test performed at low load. This is also subtracted from the raw data, which completes the drift corrections. The software has a pre-calculated value for compliance of frame of the nanoindenter, which becomes relevant at higher loads, and is accounted for during data processing. For the fracture tests, a non-negligible indentation of the cantilever surface takes place, despite using a rounded indenter tip. It is important to remove displacement caused by indentation from cantilever displacement in order to assess the mechanical behaviour correctly. To do this, load controlled indentations using the same tip are performed on the bulk surface at different loads observed from the fracture tests. The obtained data is fitted using equation 4.9 to obtain relation between load and indentation displacement.

$$P = A{\delta_i}^b \tag{4.9}$$

A and b are fitting coefficients. The function is used to determine the variation of indentation depth (δ_i) with respect to applied load,

$$\delta_i = \left(\frac{P}{A}\right)^{1/b} \tag{4.10}$$

This is then subtracted from the displacement data from the test to obtain corrected displacement (δ_{corr}).

$$\delta_{corr}(P) = \delta(P) - \delta_i(P) \tag{4.11}$$

Figure 4.22 shows an example for the effect of indentation depth correction on the $F - \delta$ curve. The force-displacement curves are then converted into

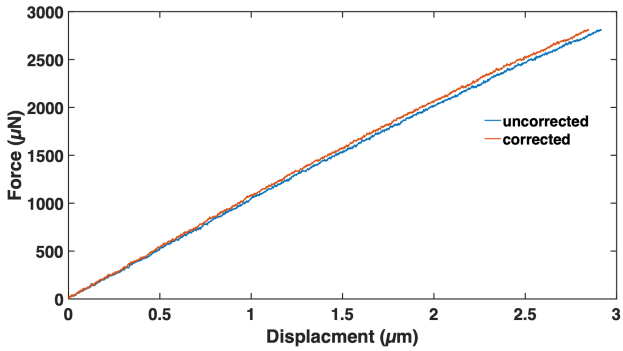

Figure 4.22: Graph showing an example for effect of indentation depth correction.

stress-strain curves using the beam flexural formula.

$$\sigma = \frac{PLy}{I} \tag{4.12}$$

P is the load, L is the span length, y is the vertical distance between neutral plane and the surface of the cantilever, which is given by the formula,

$$y = \frac{\frac{b^2 w}{2} + \frac{w^2}{4}\left(b + \frac{w}{6}\right)}{bw + \frac{w^2}{4}} \tag{4.13}$$

For a pentagonal cross section, the area moment of inertia (I)is given by the formula,

$$I = \frac{wb^3}{12} + wb\left(y - \frac{w}{2}\right)^2 + \frac{w^4}{288} + \frac{w^2}{4}\left((b - y) + \frac{w}{6}\right)^2 \tag{4.14}$$

The notations of dimensions are as per Figure 4.19. The bending strain is given by the equation,

$$\varepsilon = \frac{3y\delta}{L^2} \tag{4.15}$$

One thing to be noted here is that the above equations assume that the support is rigid, which is not true in reality. Therefore, fracture stresses were derived from linear elastic FE simulations of each tested cantilever and the analytical stress-strain curves were only used for comparison between different orientations of microcantilevers.

Linear elastic simulations were performed using the dimensions of the individual cantilevers using COMSOL Multiphysics 5.0 (Figure 4.23(a)). This provides a better estimation compared to analytical solutions since the fixed support assumption is not valid. In figure 4.23(b), the analytical calculation overestimates the stress at the fixed end. Also, the maximum stress in the

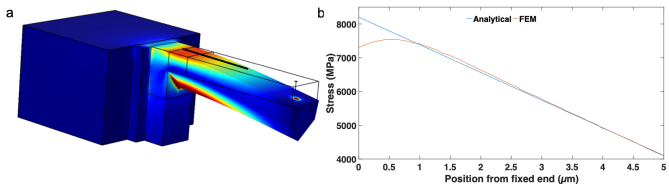

Figure 4.23: (a) Stress levels in pentagonal cross section cantilever; (b) Comparison of FEM and analytical solution of stress along the black line in (a).

case of FEM calculation is away from the fixed end due to compliance of the support. The full cross section was simulated for each cantilever because for some cantilevers, the depth of the rectangular section (b) was not the same in the front and back side, due to problems in FIB sample preparation. So the fracture stress values were extracted from the front and back edge of the cantilever and the position of maximum stress was derived as well. This was compared with the SEM images of the fracture surfaces and close agreement was seen with the position of fracture in most cases. This was performed to extract fracture stresses from both unnotched and notched microcantilevers.

For the notched microcantilevers, small displacement tests were not performed and just a displacement controlled fracture test was performed at a a rate of 10 nm/s. The thermal drift was measured on the bulk surface for these cantilevers to avoid crack propagation in cantilevers due to thermal drift measurement. The fracture toughness (K_{Ic}) was calculated according to the formula,

$$K_{Ic} = \sigma_c \sqrt{\pi a}\ f\left(\frac{a}{b}\right) \tag{4.16}$$

Where σ_c is the fracture stress obtained from FE calculations, a is the notch depth, and f(a/b) is the shape factor, according to [25].

$$f\left(\frac{a}{b}\right) = 1.85 - 3.38 \times \frac{a}{b} + 13.24 \times \left(\frac{a}{b}\right)^2 - 23.26 \times \left(\frac{a}{b}\right)^3 + 16.8 \times \left(\frac{a}{b}\right)^4 \tag{4.17}$$

Different errors can arise in the cleavage and fracture toughness measurement method. Errors in stage rotation and determination of orientation using EBSD is $< 1°$. The deviation from the ideal orientation in growth direction of the crystal is $< 3°$ due to the mounting of the wafer on aluminium stub. The measurement from SEM images can also result in small errors. Therefore, the exact angle for plane matching may not be obtained form the results. The known cleavage system closest to the measured angle is considered to be the active cleavage plane. For fracture toughness measurements, the ion implantation on FIB milled notch is of concern and has been studied extensively [64, 113]. To keep the influence minimal, the parameters recommended by literature has

been followed, and also comparison with fracture toughness values obtained from micropillar splitting experiments are also performed.

4.7 Other cantilever geometries

Apart from the aforementioned geometries, three other geometries for testing the oxide scale were developed as well. They were, however, not used in the current study since they were not a perfect fit for the designed experiments. They are described below:

4.7.1 Composite cantilever

This was the initial method developed for the fracture testing of thermally grown oxide scales on alloy 718plus. It consists of a rectangular cross section cantilever with an oxide layer on top and a metal substrate supporting the oxide layer (Figure 4.24). The ratio of thickness of oxide to substrate was about 1:4. During the bending of the cantilever, the upper layers experience tensile force which can cause the oxide layer to fracture. This would be seen in the force displacement curve as a sudden drop in force (Figure 4.25). Further bending would lead to a change in slope as the stiffness of the oxide layer and the substrate are different.

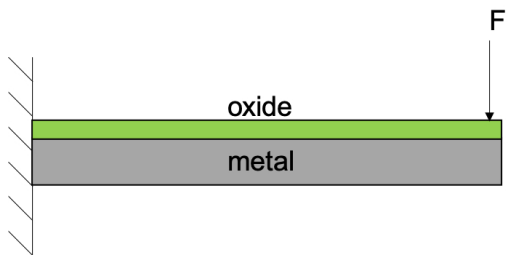

Figure 4.24: Schematic of composite microcantilever.

The advantage of this method is that the entire oxide layer will be in tension. The force resolution for this type of experiment was checked using FEM simulations and it was concluded that the fracture of the oxide should be visible in the force curve with the proportions used (typically a force drop of around 10% is expected, which would be readily observable at the applied load levels). A set of two experiments were conducted using this method, but no force drop was visible. It is not clear whether this was because cracking did not occur or because it was not detectable with the experimental setup. One of the factor could be the presence of compressive residual stresses. If the oxide

layer is under compressive stress, the stress state will not have reached tensile levels at smaller displacements. The generation of tensile stresses would require large displacements and the Kleindiek setup was not suitable for this due to movement of the force measuring tip during large displacements (see discussion section of **paper I**). The substrate has to be removed in order to relieve the residual stresses in the oxide layer.

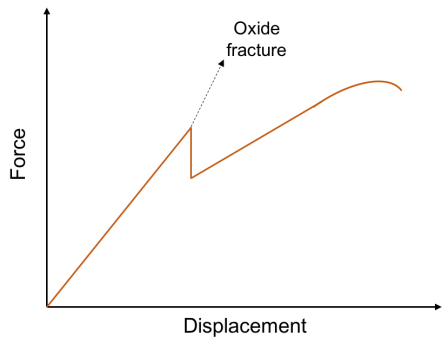

Figure 4.25: Schematic of force displacement showing how fracture can be detected in a composite microcantilever.

4.7.2 Free-standing oxide cantilever

This can be considered a modified form of the previous geometry where the metal substrate is completely removed (Figure 4.26(a)). This leads to residual stress relief in the oxide layer and also removes the substrate influence. A composite cantilever geometry is milled first and the substrate is gradually removed using FIB milling at low currents.

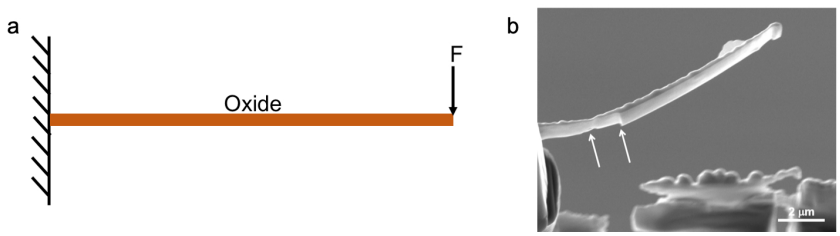

Figure 4.26: (a) Free-standing oxide cantilever schematic; (b) SEM image showing curling of cantilever and presence of stress concentrations (white arrows).

In reality, as the substrate is removed the cantilever starts to curl, which makes the FIB milling difficult and it becomes non-uniform (Figure 4.26(b)). Due to

this, the testing of such a cantilever is also not possible because of difficulties in indenter tip placements and the inference of results.

4.7.3 Peeled oxide cantilever

To prevent the curling of oxide during substrate removal in the previous case, spalled oxide scales which were seen from the longer oxidation exposures of alloy 718plus (500 hours) were targeted for the preparation of this geometry.

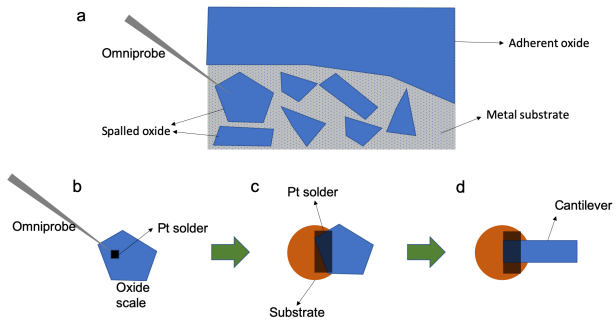

Figure 4.27: (a) Spalled oxide scales are attached to micromanipulator using platinum; (b) Oxide scale is picked up using micromanipulator and transferred to substrate; (c) Oxide attached to substrate using platinum; and (d) final geometry of cantilever milled with FIB.

Spalled oxide scales found on the oxidised alloy are picked up with the help of an Omniprobe micromanipulator typically used for TEM lift-outs by soldering the oxide to the tip using platinum (Figure 4.27(a)). This is then transferred to a different substrate, which can be a TEM grid, or needles used for atom probe tomography (Figure 4.27(b)). The scale is attached to the substrate using platinum solder and then the contact with the micromanipulator is cut off using FIB (Figure 4.27(c)). More platinum is deposited on the support for the oxide scale. The final step consists of milling the oxide scale to develop the geometry of the cantilever (Figure 4.27(d)). The resulting geometry is shown in Figure 4.28.

The advantage of using this method is that the oxide layer is free of residual stresses. However, there are some concerns regarding this method. The stability of the soldered joint is unknown and needs further analysis. Even if a large amount of Pt is used in the soldering, discontinuities within can act as stress concentrations. Also, the solder material is not stable at high temperatures, which renders this method unsuitable for high temperature testing. Even if a thermally stable solder such as tungsten is used, the thermal mismatch between the solder, specimen and the support could lead to instabilities

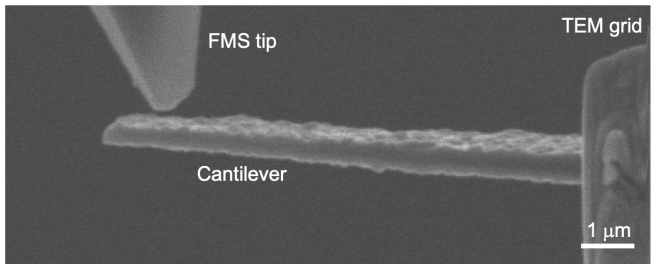

Figure 4.28: SEM image of peeled oxide cantilever.

in the mechanical test. A cantilever was manufactured from spalled scales in additional samples of exposed Allvac 718plus. It can be seen from Figure 4.28 that there is a taper in thickness of the cantilever. This would lead to errors evaluation of properties such as fracture toughness and elastic modulus. The bottom layer needs to be milled carefully in order to make the geometry uniform. The TEM grid also needs to be modified in such a way that the tip used for loading the cantilever can access it. The alignment of the FMS tip with the cantilever width centre was difficult and twisting of cantilever was observed during experiments.

4.8 Nanoindentation

Load controlled nanoindentations are performed on single crystal Cr_2O_3 samples using a Berkovich tip to obtain elastic modulus and hardness values. The typical loads used are 3 and 5 mN. The loading cycle consists of a linear loading segment followed by a hold of 10 seconds once the target load is reached. The retraction of the tip is done at a similar rate as loading. Multiple indentations are performed to ensure consistency and correctness of measurement. The analysis of the mechanical data obtained is performed using the Alemnis AMMDA data analysis software assuming an ideal Berkovich tip.

4.9 Micropillar splitting

Micropillars prepared by FIB are tested using a cube corner tip until fracture in accordance with the method proposed by Sebastiani *et al.*[123]. All the tests were done using the Alemnis in situ nanoindenter setup. A cube corner tip is used instead of Berkovich in order to enable easy placement while viewing the sample and tip through SEM. The tip is aligned with the centre of the pillar with the help of FIB milled cross on the pillar. The loading is performed in displacement controlled mode at a constant strain rate of 0.05 s^{-1}.

The tip is manually retracted at fracture. The load cycle starts with a load drift segment of 30 seconds during which the indenter is not in contact with the specimen. This is followed by the loading segment under displacement control. The displacement thermal drift is calculated using a load controlled experiment at a small load (750 µN) for 60 - 120 seconds. The determination of the dimensionless coefficient γ requires the knowledge of elastic modulus and hardness of the material. This was determined using nanoindentations using Berkovich indenter at 5mN load using the method outlined in section 4.8. Three indents on each wafer were performed which gave an average E/H ratio of 18.3 for $\{0001\}$ wafer and 23.8 for $\{11\bar{2}0\}$. γ was calculated from data given in Ghildelli *et al.* [124], which was obtained to be 0.74 for $\{0001\}$ wafer and 0.82 for $\{11\bar{2}0\}$. The fracture load was determined manually from the drift corrected $F - \delta$ data. The radius of the pillar was measured from SEM images of top views of the FIB milled microcantilevers using ImageJ.

CHAPTER 5

Results and Outlook

In this chapter, the results obtained from the papers appended with this thesis are summarised. The details are discussed in the papers. Initially, a microcantilever geometry for mechanical testing of thin oxides has been developed which circumvents the issues of residual stresses and substrate effects through the isolation of a small portion of oxide layer from the substrate. This geometry was used in microcantilever bending of oxide layers thermally grown on alloy 718plus (about 200 nm thick), which revealed the presence on plasticity (**Paper I**). One of the reasons for this was attributed to the top layer of cubic spinel. Due to the nature of cantilever bending, only the spinel layer was subjected to high tensile stresses, while the underlying Cr_2O_3 layer was under compressive stress. To determine the deformation behaviour of Cr_2O_3, thermal exposures were done on pure chromium to generate pure Cr_2O_3 scales and they were tested using microcantilever bending at room temperature and 600 °C. It was observed that the fracture behaviour at both room and high temperature was mixed inter - and transgranular, implying that cleavage behaviour of Cr_2O_3 needs to be understood (**Paper II**). Dedicated cleavage fracture studies were done with the aid of cantilevers prepared on single crystal Cr_2O_3 of specific orientations. Cleavage studies revealed the presence of both rhombohedral and pyramidal cleavage, though theory suggests just rhombohedral (**Paper III**). Therefore, a detailed study regarding orientation dependent fracture toughness was performed using notched microcantilevers. The results

reveal that there is no significant difference in fracture toughness for various orientations, implying that cleavage fracture toughness cannot be used as a criterion for determination of preferential cleavage planes in Cr_2O_3. Additionally, reliable estimates of fracture toughness values were obtained through micropillar splitting as well (**Paper IV**).

5.1 Room temperature plasticity in superalloy oxides

A novel method was developed for the testing of ultra thin thermally grown oxide scales, and the applicability was demonstrated with the help of oxide scales grown of alloy 718plus superalloy. The modified cantilever geometry was such that the oxide layer was free standing near the support for a small distance ($\sim$ 3 µm in this case) and for the rest of the cantilever length, oxide was supported by metal beneath. The free part is neither influenced by residual stresses nor by substrate. The rest of the support enables the microcantilever to be straight and not curl up, and also contributes by increasing the net length, thereby providing better displacement resolutions. A 100 hour exposure of metallographically prepared alloy 718plus in oxygen at 700 °C generated an layered oxide scale. The top layer was cubic spinel roughly 50 nm thick, followed by a Cr_2O_3 layer about 100 nm thick, and some internal Al_2O_3 was present as well. The microcantilevers were prepared in such a way that the internal Al_2O_3 was milled away using FIB.

Room temperature microcantilever bending experiments were performed with a Kleindiek micromaniulator setup, due to the force resolutions required. The force was measured using a force measurement sensor (FMS) with capability of measuring forces up to 360 µN. SEM images taken at a frequency of 1 Hz are relied upon for displacement measurements.

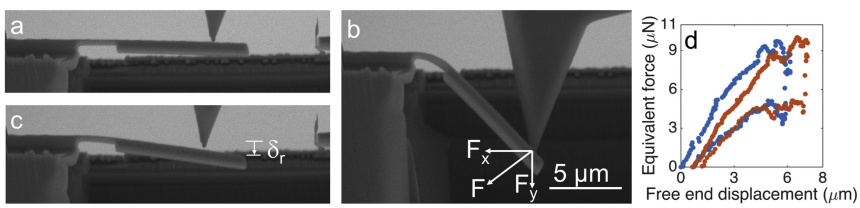

Figure 5.1: (a) Microcantilever bending test in SEM; (b) Maximum deflection; (c) Residual displacement after end of experiment; and (d) force-displacement curves for two consecutive cycles [175].

Three cantilevers were tested with progressively increasing displacements. The tested cantilevers have roughly the same dimensions. Figure 5.1(a) shows an example of microcantilever bending test. The force-displacement curves show non-linear behaviour (Figure 5.1(d)), but it does not necessarily imply plastic

deformation. At large displacements, a horizontal force component develops that can lead to such an effect (Figure 5.1(b)). But even with a correction factor applied for the horizontal force component, it is not enough to obtain a linear response, which means that there are other contributing factors, such as friction between the silicon tip and oxide surface. In all tested cantilevers, a residual displacement (δ_r) was also seen, both from the images (Figure 5.1(c)), and from the $F-\delta$ curves (Figure 5.1(d)). Since the oxide layer is not expected to undergo plastic deformation at room temperature, this effect can be due to micro-cracking. The cantilevers were therefor bent while viewing from top, but no micro-cracks were visible. To confirm their absence another cantilever was tested. The first part of the test consisted of small displacement tests to evaluate the elastic behaviour which was followed by large displacement tests similar to the previous cantilevers, creating a residual displacement. The last part of the testing also consisted of multiple small displacement tests. These tests were used to evaluate the stiffness of the cantilever before and after the large displacement tests. The initial stiffness was measured to be 2.15±0.11 N/m and the final stiffness was 2.37±0.27 N/m. This stiffness values are similar within the limits of error, implying absence of micro-cracks. Thus plasticity can be confirmed to be present in the oxide scales, which can be due to the low probability of defects at sub-micron sizes allowing for higher levels of tensile stresses to be reached and also the cubic structure of the top spinel layer allowing comparatively easier plastic deformation.

There are some aspects that need to be addressed. In the bending geometry, only the very top layer experiences high tensile stresses due to the stress gradient developed in the cross section, so the plasticity could be present only on the top spinel layer and the behaviour of the protective Cr_2O_3 layer cannot be isolated. Dedicated tests on Cr_2O_3 need to be performed. Another is the sliding of the FMS tip along the length of the cantilever which appears in the form of oscillations in the $F-\delta$ curves and needs to be taken into account.

5.2 Cr_2O_3 scale fracture

Though Cr_2O_3 is the protective oxide scale for many high temperature materials, very little work on mechanical properties of such oxide scales have been reported. Since it is difficult to isolate the Cr_2O_3 layer from the superalloy oxide mentioned in the previous section, oxide grown on pure chromium was studied. We measured the fracture properties of thermally grown Cr_2O_3 on pure chromium at room temperature and 600 °C, using the microcantilever geometry developed previously. Metallographically prepared pure chromium samples were exposed to oxygen at 700 °C for 480 hours which generated an oxide scale with average thickness of 2.8±0.6 µm. Near the metal-oxide interface, the grains are small with an average size of 100 nm, above which a

homogeneous layer of 1 µm size grains are present. Some grains on the surface have grown larger with a basal texture ($< 0001 >$). Microcantilevers were FIB milled according to the geometry mentioned in previous section (Figure 5.2).

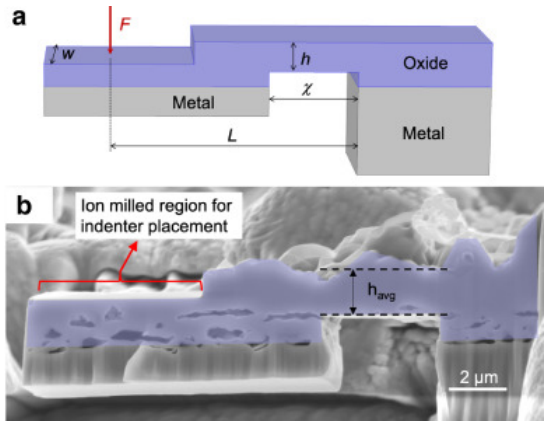

Figure 5.2: (a) Schematic of microcantilever geometry with notations of dimensions shown; (b) SEM image of FIB milled microcantilever [176].

Microcantilever bending tests were performed using an Alemnis in situ nanoindenter setup in an SEM. Both room and high temperature (600 °C) tests were performed. Microcantilevers with surface roughness ('raw') were tested at both temperatures, and a set of microcantilevers with the surface roughness removed by FIB polishing ('flat') were tested at RT. The force-displacement curves were converted to stress-strain curves using FE models due to complex geometry (details in supplementary material *section C* of **Paper II**). Fracture was observed in all tested cantilevers and was elastic until fracture (5.3(a) and (b)). Plasticity is not expected as failure occurs before reaching stress levels required for plasticity due to presence of defects.

Despite conversion to stress-strain, the variation in stiffness is prominent for the tested specimens. This can be due to geometric uncertainties in oxide scale, such are porosity and stress concentrations. FE models were used in testing effect of notch, bump and porosity, which showed that the stiffness can be halved in some situations (supplementary material *section F* in **paper II**). In addition to this material anisotropy is prominent due to the probing of a small volume containing few grains. The fracture strains at 600 °C are lower than that at RT for raw microcantilevers (Figure 5.3(c)). Higher fracture strains are observed for flat microcantilevers, which is expected due to the removal of stress concentrations. Dedicated bending tests were performed on flat microcantilevers to extract stiffness values and calculate elastic modulus, which is in the range of 217 to 301 GPa and well in agreement with literature values (Figure 5.3(d)). The elastic modulus calculated from raw cantilevers showed

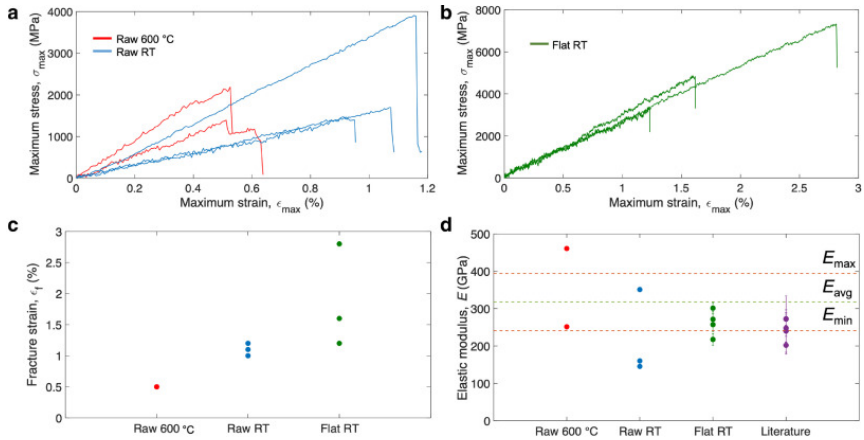

Figure 5.3: (a) Stress-strain curves for raw microcantilevers; (b) stress-strain curves for flat microcantilevers; (c) Fracture strains of tested specimens; and (d) Elastic modulus values from current study and comparison with literature (E_{max}, E_{min}, and E_{avg} are theoretical estimates) [176].

large variations between specimens, possibly due to stress concentrations and other defects.

Another important observation was from the SEM imaging of fracture surfaces, which showed mixed trans- and intergranular fracture (Figure 5.4). The presence of transgranular fracture in raw microcantilevers is surprising since the location of the stress concentration 'troughs' are along oxide grain boundaries. Removal of such stress concentrations for the flat microcantilevers increased the propensity for transgranular fracture. Fracture surface examination reveal a cleavage type of transgranular fracture. An attempt at identification of cleavage planes on flat cantilevers with the help of EBSD was made, but it was difficult to measure fracture surface angles due to polycrystalline nature of the oxide. This points towards the fact that crystallographic orientation and texture also play a role in fracture in addition to stress concentrations. However, dedicated single and bi-crystal tests need to be perform to elucidate the role of crystallographic orientations.

5.3 Fracture of single crystal Cr_2O_3

Due to the complex nature of fracture in thermally grown Cr_2O_3 scales, dedicated tests were designed for experimental determination of cleavage planes for Cr_2O_3. Two single crystals, one with growth direction perpendicular to basal plane (0001) and the other parallel to it ($11\bar{2}0$), were chosen for iden-

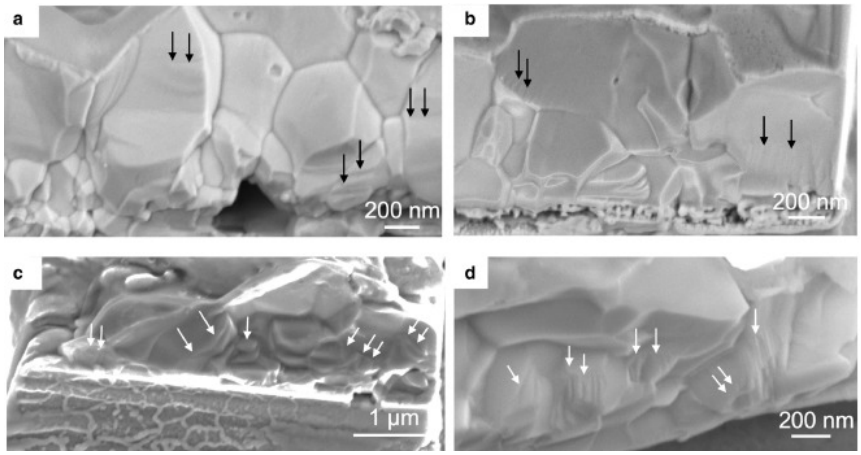

Figure 5.4: (a) and (b) show fracture surfaces from 600 °C tests; and (c) and (d) show fractures surfaces from RT tests (for raw microcantilevers) [176].

tification of cleavage planes during fracture. Microcantilevers of pentagonal cross-section were prepared using FIB in such a way that the tensile loading direction is perpendicular to known cleavage planes for corundum structure. EBSD done on crystals aided the exact alignment of microcantilevers.

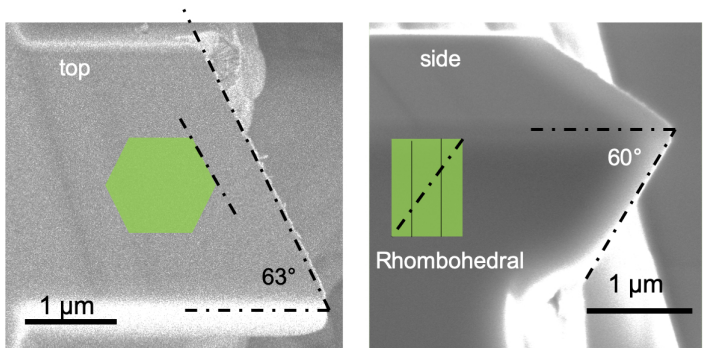

Figure 5.5: SEM images of top and side view of fracture microcantilever demonstrating determination of cleavage plane.

Microcantilever bending tests were preformed at room temperature in an SEM using Alemnis in situ nanoindenter. Fracture tests were performed in the displacement controlled mode and the $F - \delta$ curves show elastic behaviour. The fracture loads were converted to fracture stresses through FE modelling. The determination of cleavage planes was performed based on SEM imaging of fracture surfaces from different sides. The angles of fracture surfaces were determined using ImageJ from the images, and the unit cells were overlapped

over the images to determine the active cleavage plane (Figure 5.5). Tilt corrections are made for the side views since the images are taken at an angle of 70°.

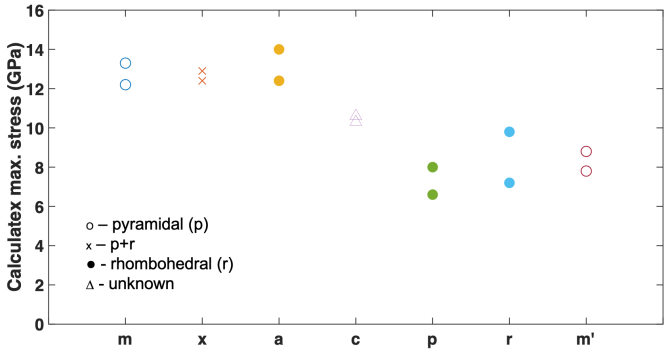

Figure 5.6: Maximum stress for fractured cantilevers from FEM calculations (fracture plane shown using symbols).

Figure 5.6 shows the plane of cleavage and fracture stresses for all tested cantilevers and the symbol type denotes the active cleavage plane. The notations on x-axis point to the plane targeted by cantilever bending. Rhombohedral (r) ($10\bar{1}2$) and pyramidal (p) ($10\bar{1}1$) cleavage was observed in various cantilevers, but r cleavage seems to be preferred over p, as the cantilevers aligned for p cleavage fracture along the r-plane instead. The basal (c) plane did not show a clear cleavage, as expected in the case of corundum structures. The cantilever oriented for a high index plane showed a combination of r and p fracture. Literature points to r cleavage in Cr_2O_3. This is based on the fact that the calculated surface energy is minimum along the plane [57], and also that the octahedral sites unoccupied by cations are arranged along this plane. The tendency for p cleavage has been previously reported for single crystal Al_2O_3 [62]. These results imply that surface energy calculations alone cannot be used as a criterion for identification of preferential cleavage for this system. Schultz *et al.* [39] suggested the use of fracture toughness of single crystals as a criterion, which was tested with notched microcantilevers.

A set of microcantilever bending experiments with FIB notched cantilevers were performed as well, in which the orientations previously studied were targeted. Only about half of tests were successful, and in several cases the crack did not follow the notch. In figure 5.7(a), the image shows that even though the crack followed the notch, it was not straight and followed the p-plane during propagation and not the targeted plane (m-plane). For cantilevers where the crack propagated away from the notch, they follow the p or r-plane (Figure 5.7(b)-(d)).

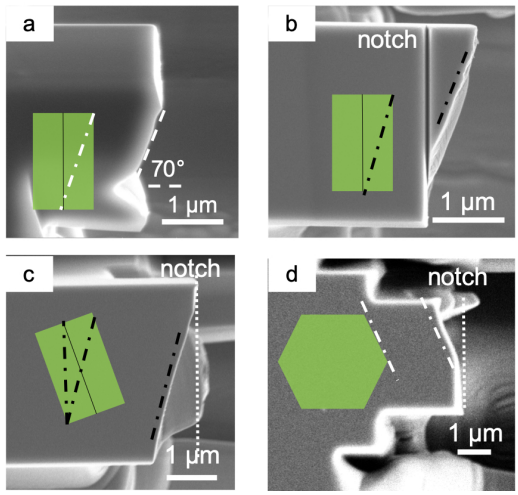

Figure 5.7: SEM images of fractured notched microcantilevers.

For the successful tests, the fracture toughness was in the range 2.6 to 4.9 MPa$\sqrt{\text{m}}$. There was no specific trend observed between the different orientations (Figure 5.8). If fracture toughness as a criterion for cleavage was valid, the toughness value for r oriented cantilevers should be lower than the others, which is not true for the current case. Such observations have been made in the case of other systems such as Al_2O_3 and ZrO, where there was no significant difference in fracture toughness values between various orientations. This shows that the cleavage fracture toughness cannot be used as criterion to determine preferential cleavage for such systems, especially Cr_2O_3.

Additionally, FIB influence on the measured fracture toughness values was evaluated using micropillar splitting. Based on Sebastiani *et al.*'s method [123], cube corner indenter was used to perform indentations of FIB milled micropillar of 2 µm diameter to generate cracks in the pillar, and using the fracture loads to measure toughness. Such experiments were performed on both the wafers, and the tip was rotated with respected to the wafer orientation to test for influence of crystallographic orientation. For pillars on the {0001} wafer, the cracks seemed to follow the sharp corners of the indenter, and for $\{11\bar{2}0\}$ wafer, rhombohedral cleavage was seen for all tip orientations. Same trend was seen in the calculated fracture toughness values as well. They ranged from 2.5 - 3 MPa$\sqrt{\text{m}}$ and did not show significant variation between orientations. The absolute values do follow the similar trend as other studies, where the ones calculated through micropillar splitting are lower than that measured through microcantilevers, since the ones from notched microcantilevers are affected by FIB. Although FIB influence in micropillar splitting is minimal, there is a concern with regard to the applicability of this method in

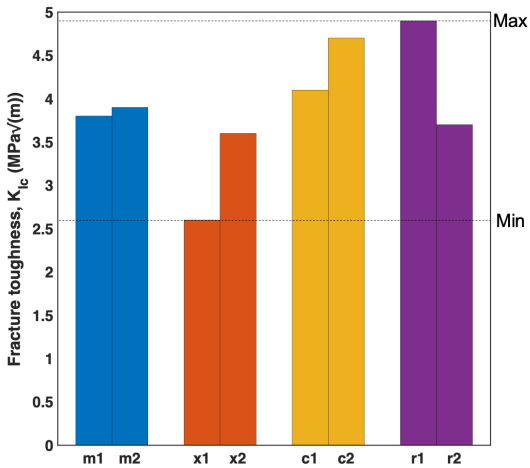

Figure 5.8: Fracture toughness values for successfully tested microcantilevers

the current case. The cohesive zone simulations [123] on which the method is based has the cracks following the sharp corners of the indenter. This condition is not met in some pillars, but the general trend between the toughness values from microcantilevers and micropillars observed by Best *et al.* [113] is followed here.

5.4 Conclusions

A significant part of this thesis work has been to develop testing methods apt for measuring mechanical properties of oxide scales. From all of the experiments and results described in the previous sections, the following conclusions have been made.

- A microcantilever geometry has been developed which has the capability of testing thin oxide scales which are otherwise difficult to be studied due to substrate influence and residual stress effects.
- The first two studies show that microcantilever bending using the developed geometry is highly effective in determination of fracture properties of oxide scales, both at room and high temperature.
- The presence of plasticity in thin oxide scales is most likely due to a small volume being studied, thereby reducing the defect probability, and the cubic spinel layer on top.

- Cr_2O_3 scale fracture is complex and the microstructure and crystallographic texture play a role in addition to stress concentrations.

- Surface energy criterion is not capable of accurately predicting preferential cleavage in Cr_2O_3, and both rhombohedral and pyramidal are preferred cleavage planes.

- Fracture toughness in single crystal Cr_2O_3 does not depend on orientation and fracture along its preferential cleavage planes. Therefore, even cleavage fracture toughness cannot be used in predicting preferential cleavage planes.

To summarise, a microcantilever based method has been developed which is effective in determination of parameters such as fracture strain and elastic modulus of protective oxide scales. This can contribute towards the development of comprehensive oxide failure diagrams and oxidation based material life models. Taking an example of Cr_2O_3, it can be seen that the fracture of oxide scales is complex and simple models may not be able to explain fracture behaviour at atomistic level. Tests on single crystal Cr_2O_3 have shown that previously known and commonly used criterion such as surface energy cannot explain the fracture behaviour completely. Therefore, atomistic aspects of fracture in such real systems need to be studied in detail towards the development of better models.

5.5 Future work suggestions

Several ideas have been proposed during the course of this project which were not realised due to the lack of time. Some of them are mentioned here which can be the path to taking this work further ahead.

- One of the demerits of cantilever bending is that the whole oxide layer is not under tension and there is a stress gradient. A cantilever based geometry was proposed in which the bending could be transformed to pure tension in the oxide scale through the use of a hinge like structure. An alternative is to platinum solder a peeled oxide layer using the method described in section 4.7.3 to a push-pull geometry and perform tensile tests. Such an experiment can be attempted so that the fracture behaviour of oxide scale in pure tension can be determined.

- Thermal exposures on pure chromium to generate Cr_2O_3 scales were done for different time period and the long term exposures (1000 hours) generated an oxide layer in which several grains on the surface grew more than 10 µm in size (Figure 3.4). Such grains can be targeted

for preparation of single crystal cantilevers, similar to work done by Mueller *et al.* [177]. In regions where two crystals are close together, cantilevers can be prepared in such a away that the interface can be tested for fracture. The advantage of this method is that a whole range of orientations can be targeted without the need to purchase expensive lab grown single crystals. Additionally, in the case of bicrystals, stress concentrations are naturally present in the grain boundaries and can be utilised for fracture testing of interfaces.

- Plastic deformation in single crystal Cr_2O_3 can be evaluated with the help of micropillar compression by varying both the size and temperatures.

- A natural next step would be also to extend this study to oxidised grain boundaries in high temperature materials such as superalloys to determine mechanism of high temperature fatigue damage in such materials.

- Microcantilever preparation using FIB on Cr_2O_3 has shown that redeposition can occur on the surface, which can influence the results if unaccounted. A method for surface protection during FIB milling was proposed based on masking the region of milling using free standing thin films. If successful, this can be highly effective in reduction of redeposition and FIB damage.

Bibliography

[1] T Giampaolo. *The Gas Turbine Handbook: Principles and Practices*. Fairmont Press, 2003.

[2] Matthew J. Donachie and Stephen James. Donachie. *Superalloys : a technical guide*. ASM International, 2002.

[3] C T Sims, N S Stoloff, and W C Hagel. *Superalloys II: High-Temperature Materials for Aerospace and Industrial Power*. Wiley, 1987.

[4] M Schütze. Stresses and decohesion of oxide scales. *Materials Science and Technology*, 4(5):407–414, 5 1988.

[5] H.-J. Christ. Is Thermomechanical Fatigue Life Predictable? *Procedia Engineering*, 55:181–190, 2013.

[6] D. G. Leo Prakash, M. J. Walsh, D. Maclachlan, and A. M. Korsunsky. Crack growth micro-mechanisms in the IN718 alloy under the combined influence of fatigue, creep and oxidation. *International Journal of Fatigue*, 31(11-12):1966–1977, 2009.

[7] F.V. Antunes, J.M. Ferreira, C.M. Branco, and J. Byme. High temperature fatigue crack growth in Inconel 718. *Materials at High Temperatures*, 17(4):439–448, 11 2000.

[8] T. Weerasooriya. Effect of frequency on fatigue crack growth rate on Inconel 718 at high temperatures. *Technical report. Air Force Wright Aeronautical Laboratories Report, AFWAL-TR-87-4038, Wright-Patterson Air Force Base, OH*, (September), 1987.

[9] Magnus Hörnqvist, Tomas Månsson, and David Gustafsson. High temperature fatigue crack growth in Alloy 718 – Effect of tensile hold times. *Procedia Engineering*, 10(10):147–152, 2011.

[10] J.A. Pfaendtner and C.J. McMahon Jr. Oxygen-induced intergranular cracking of a Ni-base alloy at elevated temperatures—an example of dynamic embrittlement. *Acta Materialia*, 49(16):3369–3377, 9 2001.

[11] U Krupp and C.J. McMahon Jr. Dynamic embrittlement–time-dependent brittle fracture. *Journal of Alloys and Compounds*, 378(1-2):79–84, 2004.

[12] B.S.-J. Kang, G. Zhang, P. Liu, and M. Ellathur. Stress Accelerated Grain Boundary Oxygen Embrittlement on creep crack growth of nickel-base superalloys. In *American Society of Mechanical Engineers, Aerospace Division (Publication) AD*, volume 50, pages 255–259, 1995.

[13] H.S. Kitaguchi, M.P. Moody, H.Y. Li, H.E. Evans, M.C. Hardy, and S. Lozano-Perez. An atom probe tomography study of the oxide–metal interface of an oxide intrusion ahead of a crack in a polycrystalline Ni-based superalloy. *Scripta Materialia*, 97:41–44, 2015.

[14] L. Viskari, M. Hörnqvist, K.L. L. Moore, Y. Cao, and K. Stiller. Intergranular crack tip oxidation in a Ni-base superalloy. *Acta Materialia*, 61(10):3630–3639, 2013.

[15] Kwai S. Chan. A Grain Boundary Fracture Model for Predicting Dynamic Embrittlement and Oxidation-Induced Cracking in Superalloys. *Metallurgical and Materials Transactions A: Physical Metallurgy and Materials Science*, 46(6):2491–2505, 2015.

[16] S. Cruchley, H.Y. Li, H.E. Evans, P. Bowen, D.J. Child, and M.C. Hardy. The role of oxidation damage in fatigue crack initiation of an advanced Ni-based superalloy. *International Journal of Fatigue*, 81:265–274, 12 2015.

[17] S. Cruchley, M. P. Taylor, H. Y. Li, H. E. Evans, P. Bowen, D. J. Child, and M. C. Hardy. Effect of prior oxidation on high cycle fatigue performance of RR1000 and role of oxidation in fatigue crack initiation. *Materials at High Temperatures*, 32(1-2):68–73, 1 2015.

[18] V. Bauer and H.-J. Christ. Thermomechanical fatigue behaviour of a third generation γ-TiAl intermetallic alloy. *Intermetallics*, 17(5):370–377, 5 2009.

[19] Michael Schütze. Modelling oxide scale fracture. *Materials at High Temperatures*, 22(1-2):147–154, 1 2005.

[20] M. Schütze, P. F. Tortorelli, and I. G. Wright. Development of a Comprehensive Oxide Scale Failure Diagram. *Oxidation of Metals*, 73(3-4):389–418, 4 2010.

[21] M. Schütze and W. J. Quadakkers. Future Directions in the Field of High-Temperature Corrosion Research. *Oxidation of Metals*, 87(5-6):681–704, 2017.

[22] S R J Saunders, M M Nagl, and M Schütze. Measurement methods for the determination of fracture strain. *Materials at High Temperatures*, 12(2-3):103–109, 6 1994.

[23] P. F. Tortorelli. Mechanical properties of chromia scales. *Le Journal de Physique IV*, 03(C9):9–943, 12 1993.

[24] M.M. Nagl, S.R.J. Saunders, W.T. Evans, and D.J. Hall. The tensile failure of nickel oxide scales at ambient and at growth temperature. *Corrosion Science*, 35(5-8):965–977, 1 1993.

[25] D. Di Maio and S.G. G Roberts. Measuring fracture toughness of coatings using focused-ion-beam-machined microbeams. *Journal of Materials Research*, 20(02):299–302, 2 2005.

[26] Nagamani Jaya B, Vikram Jayaram, and Sanjay Kumar Biswas. A new method for fracture toughness determination of graded (Pt,Ni)Al bond coats by microbeam bend tests. *Philosophical Magazine*, 92(25-27):3326–3345, 9 2012.

[27] Alex Montagne, Siddhartha Pathak, Xavier Maeder, and Johann Michler. Plasticity and fracture of sapphire at room temperature: Load-controlled microcompression of four different orientations. *Ceramics International*, 40(1):2083–2090, 1 2014.

[28] Judith Dohr, David E.J. Armstrong, Edmund Tarleton, Thierry Couvant, and Sergio Lozano-Perez. The influence of surface oxides on the mechanical response of oxidized grain boundaries. *Thin Solid Films*, 632:17–22, 2017.

[29] M. D. Abad, S. Parker, D. Frazer, M. Rebelo de Figueiredo, A. Lupinacci, K. Kikuchi, and P. Hosemann. Evaluation of the Mechanical Properties of Naturally Grown Multilayered Oxides Formed on HCM12A Using Small Scale Mechanical Testing. *Oxidation of Metals*, 84(1-2):211–231, 8 2015.

[30] D. Kupka, N. Huber, and E.T. T. Lilleodden. A combined experimental-numerical approach for elasto-plastic fracture of individual grain boundaries. *Journal of the Mechanics and Physics of Solids*, 64:455–467, 3 2014.

[31] Helen Dugdale, David E.J. Armstrong, Edmund Tarleton, Steve G. Roberts, and Sergio Lozano-Perez. How oxidized grain boundaries fail. *Acta Materialia*, 61(13):4707–4713, 8 2013.

[32] T L Anderson. *Fracture Mechanics: Fundamentals and Applications, Third Edition*. CRC Press, 2005.

[33] Jay R. Lund and Joseph P. Byrne. Leonardo Da Vinci's tensile strength tests: Implications for the discovery of engineering mechanics. *Civil Engineering and Environmental Systems*, 18(3):243–250, 6 2001.

[34] A. A. Griffith. The Phenomena of Rupture and Flow in Solids. *Philosophical Transactions of the Royal Society A: Mathematical, Physical and Engineering Sciences*, 221(582-593):163–198, 1 1921.

[35] INGLIS and CE. Stresses in a plate due to the presence of cracks and sharp corners. *Trans Inst Naval Archit*, 55:219–241, 1913.

[36] J. W. Obreimoff. The Splitting Strength of Mica. *Proceedings of the Royal Society A: Mathematical, Physical and Engineering Sciences*, 127(805):290–297, 5 1930.

[37] Paul L. Gutshall and Gordon E. Gross. Observations and mechanisms of fracture in polycrystalline alumina. *Engineering Fracture Mechanics*, 1(3):463–471, 4 1969.

[38] Kouichi Yasuda, Junichi Tatami, Kazutoshi Asada, Yohtaro Matsuo, and Shiushichi Kimura. Influence of Crack Propagation Path on the Fracture Toughness of Polycrystalline Al2O3. *Journal of the Ceramic Society of Japan*, 101(1180):1384–1389, 1993.

[39] Richard A. Schultz, Martin C. Jensen, and Richard C. Bradt. Single crystal cleavage of brittle materials. *International Journal of Fracture*, 65(4):291–312, 2 1994.

[40] S. F. Pugh. The fracture of brittle materials. *British Journal of Applied Physics*, 18(2):129–162, 2 1967.

[41] Robb Thomson, C. Hsieh, and V. Rana. Lattice trapping of fracture cracks. *Journal of Applied Physics*, 42(8):3154–3160, 1971.

[42] R Pérez and P Gumbsch. An ab initio study of the cleavage anisotropy in silicon. *Acta Materialia*, 48(18-19):4517–4530, 12 2000.

[43] Peter Gumbsch and Rowland M Cannon. Atomistic Aspects of Brittle Fracture. *MRS Bulletin*, 25(05):15–20, 5 2000.

[44] M. Schütze. 1.08 – Stress Effects in High Temperature Oxidation. In *Shreir's Corrosion*, pages 153–179. 2010.

[45] M. Schütze. Plasticity of protective oxide scales. *Materials Science and Technology*, 6(1):32–38, 1 1990.

[46] R. M. Cannon, W. H. Rhodes, and A. H. Heuer. Plastic Deformation of Fine-Grained Alumina (Al2O3): I, Interface-Controlled Diffusional Creep. *Journal of the American Ceramic Society*, 63(1-2):46–53, 1980.

[47] J.B. Wachtman Jr and L.H Maxwell. Plastic deformation of ceramic-oxide single crystals. *Journal of the American Ceramic Society*, 37(7):291–299, 1954.

[48] M Schütze. *Deformation and Cracking Behavior of Protective Oxide Scales on Heat-Resistant Steels under Tensile Strain*, volume 24. 1985.

[49] P Hancock and J R Nicholls. Application of fracture mechanics to failure of surface oxide scales. *Materials Science and Technology*, 4(5):398–406, 5 1988.

[50] J Robertson and M I Manning. Limits to adherence of oxide scales. *Materials Science and Technology*, 6(1):81–92, 1 1990.

[51] Mario Rudolphi and Michael Schütze. Investigations for the Validation of the Defect Based Scale Failure Diagrams—Part I: Nickel Oxide. *Oxidation of Metals*, 79(1-2):167–177, 2 2013.

[52] Mario Rudolphi and Michael Schütze. Investigations for the Validation of the Defect Based Scale Failure Diagrams—Part II: Extension of the Concept and Application to Nickel Oxide, Titanium Oxide and Iron Oxide. *Oxidation of Metals*, 84(1-2):45–60, 8 2015.

[53] J R Nicholls, C Mendes, and P Hancock. Measurement methods to determine the elastic properties of oxides at elevated temperatures. *Materials at High Temperatures*, 12(2-3):85–94, 6 1994.

[54] P. Hancock and J. R. Nicholls. Failure of oxide scales. *Materials at High Temperatures*, 12(2-3):209–218, 6 1994.

[55] R. C. Hurst, M. Davies, and P. Hancock. The determination of fracture strains of growing surface oxides on mild steel at high temperatures. *Oxidation of Metals*, 9(2):161–169, 4 1975.

[56] M. M. Nagl, W. T. Evans, S. R. J. Saunders, and D. J. Hall. Investigation of failure of brittle layers under compressive stresses using acoustic emission. *Materials Science and Technology*, 8(11):1043–1050, 11 1992.

[57] P.J. Lawrence, S.C. Parker, and P.W. Tasker. Computer Simulation Studies of Perfect and Defective Surfaces in Cr2O3. *Journal of the American Ceramic Society*, 71(8):C–389–C–391, 8 1988.

[58] Jizhong Sun, T. Stirner, and A. Matthews. Structure and surface energy of low-index surfaces of stoichiometric α-Al2O3 and α-Cr2O3. *Surface and Coatings Technology*, 201(7 SPEC. ISS.):4205–4208, 2006.

[59] V E Henrich and P A Cox. *The Surface Science of Metal Oxides*. Cambridge University Press, 1994.

[60] J Goodenough. Metallic oxides. *Progress in Solid State Chemistry*, 5(C):145–399, 1971.

[61] Robert Lad J. and Matthew Antonik D. Imaging of defect microstructure at oxide single crystal surfaces by atomic force microscopy. *Ceramic Transactions*, 24:359–366, 1991.

[62] H. S. Bagdasarov, G. V. Berezhkova, V. G. Govorkov, E. P. Kozlovskaya, E. A. Fedorov, and M. A. Chernysheva. The geometry of fractures caused by cleavage of α-Al2O3 single crystals. *Kristall und Technik*, 8(4):507–511, 1973.

[63] Valerian Pishchik, Leonid A. Lytvynov, and Elena R. Dobrovinskaya. *Sapphire*. Springer US, Boston, MA, 2009.

[64] A. D. Norton, S. Falco, N. Young, J. Severs, and R. I. Todd. Microcantilever investigation of fracture toughness and subcritical crack growth on the scale of the microstructure in Al2O3. *Journal of the European Ceramic Society*, 35(16):4521–4533, 2015.

[65] Ronan Henry, Thierry Blay, Thierry Douillard, Armel Descamps-Mandine, Isabelle Zacharie-Aubrun, Jean-Marie Gatt, Cyril Langlois, and Sylvain Meille. Local fracture toughness measurements in polycrystalline cubic zirconia using micro-cantilever bending tests. *Mechanics of Materials*, 136:103086, 9 2019.

[66] T. P. Weihs, S. Hong, J. C. Bravman, and W. D. Nix. Mechanical deflection of cantilever microbeams: A new technique for testing the mechanical properties of thin films. *Journal of Materials Research*, 3(5):931–942, 10 1988.

[67] Fredric Ericson and Jan Åke Schweitz. Micromechanical fracture strength of silicon. *Journal of Applied Physics*, 68(11):5840–5844, 1990.

[68] Philip R. Howie, Sandra Korte, and William J. Clegg. Fracture modes in micropillar compression of brittle crystals. *Journal of Materials Research*, 27(1):141–151, 1 2012.

[69] Michael D. Uchic, Dennis M. Dimiduk, Jeffrey N. Florando, and William D. Nix. Exploring specimen size effects in plastic deformation of Ni 3 (Al, Ta). *MRS Proceedings*, 753:BB1.4, 2 2002.

[70] Dan S. Gianola and Chris Eberl. Micro- and nanoscale tensile testing of materials. *Jom*, 61(3):24–35, 2009.

[71] W.C. Oliver and G.M. Pharr. An improved technique for determining hardness and elastic modulus using load and displacement sensing indentation experiments. *Journal of Materials Research*, 7(6):1564–1583, 6 1992.

[72] W.C. Oliver and G.M. Pharr. Measurement of hardness and elastic modulus by instrumented indentation: Advances in understanding and refinements to methodology. *Journal of Materials Research*, 19(1):3–20, 2004.

[73] J.M. Wheeler, D.E.J. Armstrong, W. Heinz, and R. Schwaiger. High temperature nanoindentation: The state of the art and future challenges. *Current Opinion in Solid State and Materials Science*, 19(6):354–366, 12 2015.

[74] P.F. Tortorelli and J.R. Keiser. The use of depth-sensing submicron indentation testing to characterize the mechanical behavior of thin oxide scales. *Scripta Metallurgica et Materialia*, 25(10):2339–2344, 10 1991.

[75] P. F. Tortorelli, S. R. J. Saunders, G. Shafirstein, and D. J. Hall. Use of the mechanical properties microprobe for characterization of oxide scales. *Materials at High Temperatures*, 12(2-3):95–101, 6 1994.

[76] S. Suresh, T. G. Nieh, and B. W. Choi. Nano-indentation of copper thin films on silicon substrates. *Scripta Materialia*, 41(9):951–957, 1999.

[77] H.Y. Y. Li, J.F. F. Sun, M.C. C. Hardy, H.E. E. Evans, S.J. J. Williams, T.J.A. J A Doel, and P. Bowen. Effects of microstructure on high temperature dwell fatigue crack growth in a coarse grain PM nickel based superalloy. *Acta Materialia*, 90:355–369, 2015.

[78] J. R. Nicholls, D. J. Hall, and P. F. Tortorelli. Hardness and modulus measurements on oxide scales. *Materials at High Temperatures*, 12(2-3):141–150, 6 1994.

[79] D. F. Bahr, A. L. Olson, K. R. Morasch, M. S. Kennedy, D. Rodriguez Marek, and A. Alamr. Fracture in Thin Oxide Films. *MRS Proceedings*, 795:U3.1, 2 2003.

[80] B. R. Lawn, A. G. Evans, and D. B. Marshall. Elastic/Plastic Indentation Damage in Ceramics: The Median/Radial Crack System. *Journal of the American Ceramic Society*, 63(9-10):574–581, 9 1980.

[81] D. S. Harding, W. C. Oliver, and G. M. Pharr. Cracking during nanoindentation and its use in the measurement of fracture toughness. *Materials Research Society Symposium - Proceedings*, 356(1):663–668, 1995.

[82] G.R. Anstis, P. Chantikul, B.R. Lawn, and D.B. Marshall. A Critical Evaluation of Indentation Techniques for Measuring Fracture Toughness: I, Direct Crack Measurements. *Journal of the American Ceramic Society*, 64(9):533–538, 9 1981.

[83] C. B. Ponton and R. D. Rawlings. Vickers indentation fracture toughness test Part 1 Review of literature and formulation of standardised indentation toughness equations. *Materials Science and Technology*, 5(9):865–872, 9 1989.

[84] Robert F. Cook and George M. Pharr. Direct Observation and Analysis of Indentation Cracking in Glasses and Ceramics. *Journal of the American Ceramic Society*, 73(4):787–817, 4 1990.

[85] Yoshinari Kato, Hiroki Yamazaki, Satoshi Yoshida, and Jun Matsuoka. Effect of densification on crack initiation under Vickers indentation test. *Journal of Non-Crystalline Solids*, 356(35-36):1768–1773, 2010.

[86] K. Niihara, R. Morena, and D. P.H. Hasselman. Evaluation of KIc of brittle solids by the indentation method with low crack-to-indent ratios. *Journal of Materials Science Letters*, 1(1):13–16, 1982.

[87] Jae il Jang and G. M. Pharr. Influence of indenter angle on cracking in Si and Ge during nanoindentation. *Acta Materialia*, 56(16):4458–4469, 2008.

[88] B. A. Mound and G. M. Pharr. Nanoindentation of Fused Quartz at Loads Near the Cracking Threshold. *Experimental Mechanics*, 59(3):369–380, 2019.

[89] Dylan J. Morris and Robert F. Cook. In situ cube-corner indentation of soda-lime glass and fused silica. *Journal of the American Ceramic Society*, 87(8):1494–1501, 2004.

[90] Sebastian Bruns, Laszlo Petho, Christian Minnert, Johann Michler, and Karsten Durst. Fracture toughness determination of fused silica by cube corner indentation cracking and pillar splitting. *Materials and Design*, 186:108311, 2020.

[91] Muhammad Zeeshan Mughal, Hugues Yanis Amanieu, Riccardo Moscatelli, and Marco Sebastiani. A comparison of microscale techniques for determining fracture toughness of LiMn 2 O 4 particles. *Materials*, 10(4):403, 2017.

[92] J. H. Lee, Y. F. Gao, K. E. Johanns, and G. M. Pharr. Cohesive interface simulations of indentation cracking as a fracture toughness measurement method for brittle materials. *Acta Materialia*, 60(15):5448–5467, 2012.

[93] Yuri Kadin, Mehdi Mazaheri, Vadim Zolotarevskiy, Charlotte Vieillard, and Mark Hadfield. Finite elements based approaches for the modelling of radial crack formation upon Vickers indentation in silicon nitride ceramics. *Journal of the European Ceramic Society*, 39(14):4011–4022, 2019.

[94] B.J. Inkson, H.Z. Wu, T. Steer, and G. Möbus. 3D Mapping of Subsurface Cracks in Alumina Using FIB. *MRS Proceedings*, 649:Q7.7, 3 2000.

[95] A. Baggott, M. Mazaheri, and B. J. Inkson. 3D characterisation of indentation induced sub-surface cracking in silicon nitride using FIB tomography. *Journal of the European Ceramic Society*, 39(13):3620–3626, 2019.

[96] C. Motz, T. Schöberl, and R. Pippan. Mechanical properties of micro-sized copper bending beams machined by the focused ion beam technique. *Acta Materialia*, 53(15):4269–4279, 9 2005.

[97] Goran Žagar, Václav Pejchal, Martin G. Mueller, Lionel Michelet, and Andreas Mortensen. Fracture toughness measurement in fused quartz using triangular chevron-notched micro-cantilevers. *Scripta Materialia*, 112:132–135, 2016.

[98] Johannes Ast, Mikhail N. Polyakov, Gaurav Mohanty, Johann Michler, and Xavier Maeder. Interplay of stresses, plasticity at crack tips and small sample dimensions revealed by in-situ microcantilever tests in tungsten. *Materials Science and Engineering: A*, 710(August 2017):400–412, 1 2018.

[99] S. Massl, W. Thomma, J. Keckes, and R. Pippan. Investigation of fracture properties of magnetron-sputtered TiN films by means of a FIB-based cantilever bending technique. *Acta Materialia*, 57(6):1768–1776, 2009.

[100] D. Kupka and E. T. Lilleodden. Mechanical Testing of Solid-Solid Interfaces at the Microscale. *Experimental Mechanics*, 2012.

[101] Farasat Iqbal. *Fracture Mechanisms of γ–TiAl Alloys Investigated by In-situ Experiments in a Scanning Electron and Atomic Force Microscope.* PhD thesis, 2012.

[102] Balila Nagamani Jaya, Christoph Kirchlechner, and Gerhard Dehm. Can microscale fracture tests provide reliable fracture toughness values? A case study in silicon. *Journal of Materials Research*, 30(5):686–698, 3 2015.

[103] Kurt Matoy, Thomas Detzel, Matthias Müller, Christian Motz, and Gerhard Dehm. Interface fracture properties of thin films studied by using the micro-cantilever deflection technique. *Surface and Coatings Technology*, 204(6-7):878–881, 12 2009.

[104] Balila Nagamani Jaya, Jeffrey M. Wheeler, Juri Wehrs, James P. Best, Rafael Soler, Johann Michler, Christoph Kirchlechner, and Gerhard Dehm. Microscale Fracture Behavior of Single Crystal Silicon Beams at Elevated Temperatures. *Nano Letters*, 16(12):7597–7603, 12 2016.

[105] Erik Camposilvan, Oscar Torrents, and Marc Anglada. Small-scale mechanical behavior of zirconia. *Acta Materialia*, 80:239–249, 11 2014.

[106] D. Kiener, W. Grosinger, G. Dehm, and R. Pippan. A further step towards an understanding of size-dependent crystal plasticity: In situ tension experiments of miniaturized single-crystal copper samples. *Acta Materialia*, 56(3):580–592, 2 2008.

[107] Johannes Ast, Mathias Göken, and Karsten Durst. Size-dependent fracture toughness of tungsten. *Acta Materialia*, 138:198–211, 10 2017.

[108] M.G. Mueller, V. Pejchal, G. Žagar, A. Singh, M. Cantoni, and A. Mortensen. Fracture toughness testing of nanocrystalline alumina and fused quartz using chevron-notched microbeams. *Acta Materialia*, 86:385–395, 3 2015.

[109] Kurt Matoy, Helmut Schönherr, Thomas Detzel, Thomas Schöberl, Reinhard Pippan, Christian Motz, and Gerhard Dehm. A comparative micro-cantilever study of the mechanical behavior of silicon based passivation films. *Thin Solid Films*, 518(1):247–256, 11 2009.

[110] Stefan Wurster, Christian Motz, and Reinhard Pippan. Characterization of the fracture toughness of micro-sized tungsten single crystal notched specimens. *Philosophical Magazine*, 92(14):1803–1825, 5 2012.

[111] Denise Yin, Christopher J. Marvel, Fiona Yuwei Cui, Richard P. Vinci, and Martin P. Harmer. Microstructure and fracture toughness of electrodeposited Ni-21 at.% W alloy thick films. *Acta Materialia*, 143:272–280, 1 2018.

[112] Ashish Kumar Saxena, Ankit Kumar, Michael Herbig, Steffen Brinckmann, Gerhard Dehm, and Christoph Kirchlechner. Micro fracture investigations of white etching layers. *Materials and Design*, 180:107892, 2019.

[113] James P. Best, Johannes Zechner, Jeffrey M. Wheeler, Rachel Schoeppner, Marcus Morstein, and Johann Michler. Small-scale fracture toughness of ceramic thin films: the effects of specimen geometry, ion beam

notching and high temperature on chromium nitride toughness evaluation. *Philosophical Magazine*, 96(32-34):3552–3569, 2016.

[114] Steffen Brinckmann, Kurt Matoy, Christoph Kirchlechner, and Gerhard Dehm. On the influence of microcantilever pre-crack geometries on the apparent fracture toughness of brittle materials. *Acta Materialia*, 136:281–287, 9 2017.

[115] Michael Uchic, Dennis M Dimiduk, Jeffrey N Florando, and William D Nix. Sample dimension influence strength and crystal plasticity. *Science*, 305(5686):986–989, 2004.

[116] Thomas Edward James Edwards, Fabio Di Gioacchino, Gaurav Mohanty, Juri Wehrs, Johann Michler, and William John Clegg. Longitudinal twinning in a TiAl alloy at high temperature by in situ microcompression. *Acta Materialia*, 148:202–215, 2018.

[117] G. Dehm, B. N. Jaya, R. Raghavan, and C. Kirchlechner. Overview on micro- and nanomechanical testing: New insights in interface plasticity and fracture at small length scales. *Acta Materialia*, 142:248–282, 2018.

[118] Julia Hütsch and Erica T. Lilleodden. The influence of focused-ion beam preparation technique on microcompression investigations: Lathe vs. annular milling. *Scripta Materialia*, 77:49–51, 2014.

[119] Julia R. Greer, Warren C. Oliver, and William D. Nix. Size dependence of mechanical properties of gold at the micron scale in the absence of strain gradients. *Acta Materialia*, 53(6):1821–1830, 2005.

[120] D. Kiener, C. Motz, M. Rester, M. Jenko, and G. Dehm. FIB damage of Cu and possible consequences for miniaturized mechanical tests. *Materials Science and Engineering A*, 459(1-2):262–272, 2007.

[121] Fredrik Östlund, Karolina Rzepiejewska-Malyska, Klaus Leifer, Lucas M. Hale, Yuye Tang, Roberto Ballarini, William W. Gerberich, and Johann Michler. Brittle-to-Ductile Transition in Uniaxial Compression of Silicon Pillars at Room Temperature. *Advanced Functional Materials*, 19(15):2439–2444, 8 2009.

[122] H. Zhang, B. E. Schuster, Q. Wei, and K. T. Ramesh. The design of accurate micro-compression experiments. *Scripta Materialia*, 54(2):181–186, 2006.

[123] M. Sebastiani, K. E. Johanns, E. G. Herbert, F. Carassiti, and G. M. Pharr. A novel pillar indentation splitting test for measuring fracture toughness of thin ceramic coatings. *Philosophical Magazine*, 95(16-18):1928–1944, 2015.

[124] Matteo Ghidelli, Marco Sebastiani, Kurt E. Johanns, and George M. Pharr. Effects of indenter angle on micro-scale fracture toughness measurement by pillar splitting. *Journal of the American Ceramic Society*, 100(12):5731–5738, 12 2017.

[125] Alexander J. G. Lunt, Gaurav Mohanty, Tee K. Neo, Johann Michler, and Alexander M. Korsunsky. Microscale resolution fracture toughness profiling at the zirconia-porcelain interface in dental prostheses. *Micro+Nano Materials, Devices, and Systems*, 9668(December 2015):96685S, 2015.

[126] C. M. Lauener, L. Petho, M. Chen, Y. Xiao, J. Michler, and J. M. Wheeler. Fracture of Silicon: Influence of rate, positioning accuracy, FIB machining, and elevated temperatures on toughness measured by pillar indentation splitting. *Materials and Design*, 142:340–349, 2018.

[127] Nagamani Jaya B, Vikram Jayaram, and Sanjay Kumar Biswas. A new method for fracture toughness determination of graded (Pt,Ni)Al bond coats by microbeam bend tests. *Philosophical Magazine*, 92(25-27):3326–3345, 2012.

[128] B. Nagamani Jaya and Vikram Jayaram. Crack stability in edge-notched clamped beam specimens: Modeling and experiments. *International Journal of Fracture*, 188(2):213–228, 2014.

[129] Balila Nagamani Jaya, Sanjit Bhowmick, S.A. Syed Asif, and Vikram Jayaram. In-situ study of microscale fracture of diffusion aluminide bond coats: Effect of platinum. *Journal of Materials Research*, 30(21):3343–3353, 11 2015.

[130] Fiona Yuwei Cui and Richard P. Vinci. A chevron-notched bowtie microbeam bend test for fracture toughness measurement of brittle materials. *Scripta Materialia*, 132:53–57, 4 2017.

[131] S. Liu, J. M. Wheeler, P. R. Howie, X. T. Zeng, J. Michler, and W. J. Clegg. Measuring the fracture resistance of hard coatings. *Applied Physics Letters*, 102(17):171907, 4 2013.

[132] Yu Liu, Cristina Ramirez, Lin Zhang, Wenwen Wu, and Nitin P. Padture. In situ direct observation of toughening in isotropic nanocomposites of alumina ceramic and multiwall carbon nanotubes. *Acta Materialia*, 127:203–210, 2017.

[133] R. Konetschnik, R. Daniel, R. Brunner, and D. Kiener. Selective interface toughness measurements of layered thin films. *AIP Advances*, 7(3), 2017.

[134] Giorgio Sernicola, Tommaso Giovannini, Punit Patel, James R. Kermode, Daniel S. Balint, T. Ben Britton, and Finn Giuliani. In situ stable crack growth at the micron scale. *Nature Communications*, 8(1), 2017.

[135] Brian Lawn. *Fracture of brittle solids*. Cambridge University Press, Cambridge, 1993.

[136] Afrooz Barnoush and Horst Vehoff. Electrochemical nanoindentation: A new approach to probe hydrogen/deformation interaction. *Scripta Materialia*, 55(2):195–198, 2006.

[137] Afrooz Barnoush and Horst Vehoff. Recent developments in the study of hydrogen embrittlement: Hydrogen effect on dislocation nucleation. *Acta Materialia*, 58(16):5274–5285, 9 2010.

[138] Afrooz Barnoush, Jules Dake, Nousha Kheradmand, and Horst Vehoff. Examination of hydrogen embrittlement in FeAl by means of in situ electrochemical micropillar compression and nanoindentation techniques. *Intermetallics*, 18(7):1385–1389, 2010.

[139] Tarlan Hajilou, Yun Deng, Bjørn Rune Rogne, Nousha Kheradmand, and Afrooz Barnoush. In situ electrochemical microcantilever bending test: A new insight into hydrogen enhanced cracking. *Scripta Materialia*, 132:17–21, 2017.

[140] Dong Wang, Xu Lu, Di Wan, Zhiming Li, and Afrooz Barnoush. In-situ observation of martensitic transformation in an interstitial metastable high-entropy alloy during cathodic hydrogen charging. *Scripta Materialia*, 173:56–60, 2019.

[141] Y. Deng, T. Hajilou, D. Wan, N. Kheradmand, and A. Barnoush. In-situ micro-cantilever bending test in environmental scanning electron microscope: Real time observation of hydrogen enhanced cracking. *Scripta Materialia*, 127:19–23, 2017.

[142] Yun Deng and Afrooz Barnoush. Hydrogen embrittlement revealed via novel in situ fracture experiments using notched micro-cantilever specimens. *Acta Materialia*, 142:236–247, 2018.

[143] Di Wan, Yun Deng, and Afrooz Barnoush. Hydrogen embrittlement effect observed by in-situ hydrogen plasma charging on a ferritic alloy. *Scripta Materialia*, 151:24–27, 2018.

[144] Jinwoo Kim and Cemal Cem Tasan. Microstructural and micromechanical characterization during hydrogen charging: An in situ scanning electron microscopy study. *International Journal of Hydrogen Energy*, 44(12):6333–6343, 2019.

[145] B. N. Lucas and W. C. Oliver. Time Dependent Indentation Testing At Non-Ambient Temperatures Utilizing the High Temperature Mechanical Properties Microprobe. *MRS Proceedings*, 356:645, 2 1994.

[146] J. F. Smith and S. Zheng. High temperature nanoscale mechanical property measurements. *Surface Engineering*, 16(2):143–146, 2000.

[147] J.M. Wheeler, P. Brodard, and J. Michler. Elevated temperature, in situ indentation with calibrated contact temperatures. *Philosophical Magazine*, 92(25-27):3128–3141, 9 2012.

[148] J. M. Wheeler, C. Niederberger, C. Tessarek, S. Christiansen, and J. Michler. Extraction of plasticity parameters of GaN with high temperature, in situ micro-compression. *International Journal of Plasticity*, 40:140–151, 2013.

[149] Gaurav Mohanty, Jeffrey M. Wheeler, Rejin Raghavan, Juri Wehrs, Madoka Hasegawa, Stefano Mischler, Laetitia Philippe, and Johann Michler. Elevated temperature, strain rate jump microcompression of nanocrystalline nickel. *Philosophical Magazine*, 95(16-18):1878–1895, 2015.

[150] S. Lotfian, M. Rodríguez, K. E. Yazzie, N. Chawla, J. Llorca, and J. M. Molina-Aldareguía. High temperature micropillar compression of Al/SiC nanolaminates. *Acta Materialia*, 61(12):4439–4451, 2013.

[151] Rafael Soler, Jeffrey M. Wheeler, Hyung Jun Chang, Javier Segurado, Johann Michler, Javier Llorca, and Jon M. Molina-Aldareguia. Understanding size effects on the strength of single crystals through high-temperature micropillar compression. *Acta Materialia*, 81:50–57, 2014.

[152] Georgios Constantinides, Catherine A. Tweedie, Doria M. Holbrook, Patrick Barragan, James F. Smith, and Krystyn J. Van Vliet. Quantifying deformation and energy dissipation of polymeric surfaces under localized impact. *Materials Science and Engineering A*, 489(1-2):403–412, 2008.

[153] Jennifer L. Hay, Carlos Morillo, and Julie Silk. A Scanning-Probe Technique for Mapping the Hardness of Lead-Free Solders. *MRS Proceedings*, 1652(23):13–1652, 2 2014.

[154] Pardhasaradhi Sudharshan Phani and Warren Carl Oliver. Ultra high strain rate nanoindentation testing. *Materials*, 10(6), 2017.

[155] Gaylord Guillonneau, Maxime Mieszala, Juri Wehrs, Jakob Schwiedrzik, Serge Grop, Damian Frey, Laetitia Philippe, Jean Marc Breguet, Johann Michler, and Jeffrey M. Wheeler. Nanomechanical testing at high strain rates: New instrumentation for nanoindentation and microcompression. *Materials and Design*, 148:39–48, 2018.

[156] James P. Best, Gaylord Guillonneau, Serge Grop, Aidan A. Taylor, Damian Frey, Quentin Longchamp, Tobias Schär, Marcus Morstein, Jean Marc Breguet, and Johann Michler. High temperature impact testing of a thin hard coating using a novel high-frequency in situ micromechanical device. *Surface and Coatings Technology*, 333(July 2017):178–186, 2018.

[157] Rajaprakash Ramachandramoorthy, Jakob Schwiedrzik, Laszlo Petho, Carlos Guerra-Nunez, Damian Frey, Jean Marc Breguet, and Johann Michler. Dynamic Plasticity and Failure of Microscale Glass: Rate-Dependent Ductile-Brittle-Ductile Transition. *Nano Letters*, 19(4):2350–2359, 2019.

[158] Y. Parsa, L. Latu-Romain, Y. Wouters, S. Mathieu, T. Perez, and M. Vilasi. Effect of oxygen partial pressure on the semiconducting properties of thermally grown chromia on pure chromium. *Corrosion Science*, 141(June):46–52, 2018.

[159] L. Latu-Romain, Y. Parsa, S. Mathieu, M. Vilasi, and Y. Wouters. Chromia Scale Thermally Grown on Pure Chromium Under Controlled p(O2) Atmosphere: II—Spallation Investigation Using Photoelectrochemical Techniques at a Microscale. *Oxidation of Metals*, 90(3-4):267–277, 2018.

[160] D. Caplan and G. I. Sproule. Effect of oxide grain structure on the high-temperature oxidation of Cr. *Oxidation of Metals*, 9(5):459–472, 10 1975.

[161] P. Kofstad and K. P. Lillerud. Chromium transport through Cr2O3scales I. On lattice diffusion of chromium. *Oxidation of Metals*, 17(3-4):177–194, 1982.

[162] Hannes Falk-Windisch, Per Malmberg, Mohammad Sattari, Jan Erik Svensson, and Jan Froitzheim. Determination of the oxide scale growth mechanism using 18O-tracer experiments in combination with Transmission Electron Microscopy and nanoscale Secondary Ion Mass Spectrometry. *Materials Characterization*, 136(November 2017):128–133, 2018.

[163] Joseph I. Goldstein, Dale E. Newbury, Patrick Echlin, David C. Joy, Charles E. Lyman, Eric Lifshin, Linda Sawyer, and Joseph R. Michael. *Scanning Electron Microscopy and X-ray Microanalysis*. Springer US, Boston, MA, 2003.

[164] Patrick W. Trimby. Orientation mapping of nanostructured materials using transmission Kikuchi diffraction in the scanning electron microscope. *Ultramicroscopy*, 120:16–24, 9 2012.

[165] Glenn C. Sneddon, Patrick W. Trimby, and Julie M. Cairney. Transmission Kikuchi diffraction in a scanning electron microscope: A review. *Materials Science and Engineering: R: Reports*, 110:1–12, 12 2016.

[166] L A Giannuzzi, B W Kempshall, S M Schwarz, J K Lomness, B I Prenitzer, and F A Stevie. FIB Lift-Out Specimen Preparation Techniques. In Lucille A Giannuzzi and Fred A Stevie, editors, *Introduction to Focused Ion Beams: Instrumentation, Theory, Techniques and Practice*, pages 201–228. Springer US, Boston, MA, 2005.

[167] C A Volkert and A M Minor. Focused Ion Beam Microscopy and Micromachining. *MRS Bulletin*, 32(May):389–399, 2007.

[168] L. A. Woodward. General Introduction. In *Raman Spectroscopy*, volume 55, pages 1–43. Springer US, Boston, MA, 1967.

[169] Olaf Hollricher and Wolfram Ibach. High Resolution Optical and Confocal Microscopy. In *Springer Series in Surface Sciences*, volume 66, pages 25–45. Springer International Publishing, 2018.

[170] J. Birnie, C. Craggs, D.J Gardiner, and P.R Graves. Ex situ and in situ determination of stress distributions in chromium oxide films by raman microscopy. *Corrosion Science*, 33(1):1–12, 1 1992.

[171] Julie Mougin, Noël Rosman, Guy Lucazeau, and Alain Galerie. In situ Raman monitoring of chromium oxide scale growth for stress determination. *Journal of Raman Spectroscopy*, 32(9):739–744, 2001.

[172] M. Kemdehoundja, J. L. Grosseau-Poussard, J. F. Dinhut, and B. Panicaud. Growth stresses in α-Cr2O3 thermal oxide films determined by ¡i¿in situ¡/i¿ high temperature Raman spectroscopy. *Journal of Applied Physics*, 102(9):093513, 2007.

[173] Jan-Åke Schweitz. Mechanical Characterization of Thin Films by Micromechanical Techniques. *MRS Bulletin*, 17(07):34–45, 7 1992.

[174] Marcello Conte, Gaurav Mohanty, Jakob J. Schwiedrzik, Jeffrey M. Wheeler, Bertrand Bellaton, Johann Michler, and Nicholas X. Randall. Novel high temperature vacuum nanoindentation system with active surface referencing and non-contact heating for measurements up to 800 °C. *Review of Scientific Instruments*, 90(4):045105, 4 2019.

[175] Anand H.S. Iyer, Krystyna Stiller, and Magnus Hörnqvist Colliander. Room temperature plasticity in thermally grown sub-micron oxide scales revealed by micro-cantilever bending. *Scripta Materialia*, 144:9–12, 2 2018.

[176] Anand H.S. Iyer, Gaurav Mohanty, Krystyna Stiller, Johann Michler, and Magnus Hörnqvist Colliander. Microscale fracture of chromia scales. *Materialia*, 8(September):100465, 12 2019.

[177] M. G. Mueller, G. Žagar, and A. Mortensen. In-situ strength of individual silicon particles within an aluminium casting alloy. *Acta Materialia*, 143:67–76, 2018.